Synthesis, characterization, and field-test of nanocatalysts for hydrogen production by hydrolysis of chemical hydrides

Rohan P. Fernandes

Supervisor : Prof. Antonio Miotello

A thesis submitted for the degree of

Doctor of Philosophy in Physics

March 2011

To My Family

Acknowledgements

First and foremost I offer my sincerest gratitude to my supervisor, Prof. Antonio Miotello, whose encouragement, guidance and support throughout the period of my Ph.D. enabled me to develop an understanding of the subject. I have been amazingly fortunate to have him as an advisor who gave me the freedom and opportunity to explore. One simply could not wish for a better or friendlier supervisor.

I am deeply grateful to Prof. D.C. Kothari for inspiring me to take up research and also providing me with opportunities to work under his guidance during the initial period of my research career.

I am indebted to all the members of the my research group with whom I have interacted during the course of my Ph.D. I would like to thank Dr. Nainesh Patel for his continuous support, suggestions and discussions that has helped me sort out the technical details of my work. I am thankful to Prof. Graziano Guella for giving his valuable time on NMR spectroscopy. Barbara Patton and Cristian Zanchetta who helped tutor me in methods necessary in catalyst testing. Paolo Mosaner was responsible for the smooth running of the of PLD. Laura Toniutti and Nicola Bazzanella who have provided me with all of the SEM images with consistent quality covered in this thesis, and Cristina Armellini provided me with the XRD measurements. I am also thankful to Marco Adami and Alessandra Santini who have always been there to give a helping hand in carrying out my experiments.

My sincere thanks goes to Claudio Cestari for his support with his exceptional skills in fabrication of experimental set ups. He has been a wonderful friend making my stay pleasent in Trento.

Many of my friends have helped me through these years; I especially would like to thank Ashwin Kale, Rupali Dolam, Devendra Saroj, Seema, Kiran Bhakta, G. R. Gangadharan, Lejo Joseph and other friends in Trento for all their support and encouragement. I thank all my close friends back in India for being there for me.

Most importantly, none of this would have been possible without the love and patience of my family, to whom I dedicated this dissertation. My heartfelt gratitude to my parents, my brother and my wife Deepa, for their love, encouragement and understanding.

Abstract

There is a growing concern related to increasing energy requirement and greenhouse gas emissions. Hydrogen gas is recognised as a desirable clean fuel and may be a sustainable solution. Hydrogen gas can be directly used as an anodic fuel for Proton Exchange Membrane Fuel Cell that converts chemical energy of hydrogen into electrical energy with no environmentally harmful by-products. Chemical hydrides with high hydrogen storage capacity in terms of gravimetric and volumetric efficiencies are the most promising candidates to supply pure hydrogen at room temperature. Among them, Sodium borohydride (SBH) and Ammonia borane (AB) have drawn a lot of interest as they are stable, non-flammable, non-toxic, and have a high hydrogen storage capability. Large amount of pure hydrogen gas is released during the hydrolysis of these chemical hydrides in presence of certain catalysts. The by-products are non-toxic, environmentally safe and can be recycled. Noble catalysts like Pt and Pd, used in the past to enhance the hydrogen production rate, do not seem to be viable for industrial application considering their cost and availability. Co and Ni borides are considered as good candidates for catalyzed hydrolysis owing to their good catalytic activity, low cost and effortlessly synthesis. Transition metals with varying $\frac{metal}{(Co+metal)}$ molar ratio were doped in Co-B catalyst and the effect of metal doping on surface morphology, electronic interaction, and catalytic efficiency of the alloy catalyst powder on hydrogen production by hydrolysis of SBH and AB were studied. On the basis of characterization results, the role of each metal species, involved in hydrolysis and enhanced catalytic performance is discussed. The stability, reusability, and durability of these catalysts have also been investigated. Nanoparticle-assembled Co-B-P thin films on Ni foam (by electroless deposition), along with supported and unsupported Co-B nanoparticles over carbon films were synthesized by Pulsed Laser Deposition and studied for catalytic hydrolysis.

Contents

Chapter 1

Introduction

"What you are is what you have been,
and what you will be is what you do now."
-Gautam Buddha

1.1 Energy

1.1.1 Energy perspectives

From the time we wake up and even while we are asleep, energy affects our life. Whether we notice it or not, we are dependent on abundant and uninterrupted supply of energy. Energy is also an essential commodity for increasing agricultural and industrial productivity. The social and economic development of a country has a positive impact when there is an increase in its energy consumption. Development in technology and increased standard of living demands increase in the requirement of energy. Continuous expansion of world population also results in increasing need for energy to support human existence.

Energy insecurity and rising prices of conventional energy sources are major threats to economic and political stability. These factors lead to world population transition, migration, hunger, environmental problem, deteriorating health, diseases, terrorism, energy and natural resources concerns and wars [1]. The Global economic recession that began in 2007 and continued into 2009 had profound impact on the world energy demand. The total world energy consumption contracted by 1.2% in 2008 and estimated 2.2% in 2009 as manufacturing and consumer demand for goods and services declined [2]. This clearly reflects the interdependence of energy and economic growth.

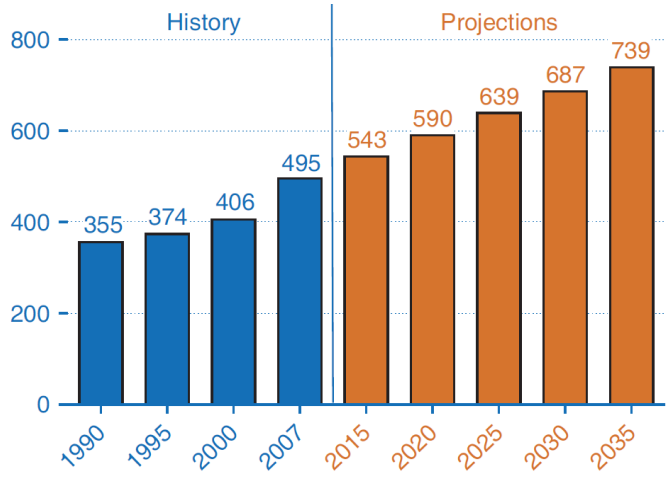

Figure 1.1 – World marketed energy consumption in Btu

Fig. 1.1 presents the world marketed energy consumption from the past and the predicted consumption for the future. As seen from the graphs, there would be a steady increase in the energy consumption; it would grow by 49% from 2007 to 2035. The world energy use will rise from 495 Btu (quardrillion British thermal units) in 2007 to 590 Btu in 2020, and 739 Btu in 2035, i.e. if the current laws and policies remain unchanged. [2]. With the growing need for energy for the future, there is a direct need in production of energy.

Presently, the world energy systems are largely based on combustion of fossil fuels, i.e. petroleum, natural gas, and coal; and are being consumed at an alarming rate. When we turn on the lights, watch TV, or take a shower, the electricity is being generated by fossil fuels. We are accustomed to using fossil fuels as our central source of energy for everyday exploiting. Electricity is the most convenient form of energy and is largely dependent on coal. Coal is the second most used source of energy. It is filling much of the growing energy demands of those developing countries, where energy-intensive industrial production is growing rapidly and large coal reserves exist with limited reserves of other energy sources. The world coal reserves are estimated at 909 billion tons, reflecting a current reserves-to-production ratio of 129 years [2].

Crude Oil and its derivatives are used as primary source of energy and thus is constantly in high demand. As a dense energy source, it powers majority of vehicles and thus is one of the world's most important commodities. The price of oil has been escalating and is likely to continue in the coming years. According to Oil & Gas Journal (January 2010), world oil reserves were estimated to be 1,354 billion barrels [3]. While, the worldwide reserves-to-production ratio is estimated at 45

years [4]. The third major source of energy is Natural gas that is mostly used for household purposes. LPG (Liquefied Petroleum Gas) is a mixture of hydrocarbons gases that primarily contains propane, and mostly used for cooking and heating. CNG (Compressed Natural Gas) mostly contains Methane, a substitute for LPG. As it is cleaner, they are also used as fuel in CNG-powered vehicles [5]. The natural gas reserves estimated at 6,609 trillion cubic feet, giving us the reserves-to-production ratio of 60 years.

These forms of energy are rapidly depleting, i.e., in the next 45 and 60 years we will run out of both oil and natural gas respectively, while coal will last only for the next 129 years. In this scenario finding an alternate source of energy become an urgent need. If countries do not increasingly diversify their reliance upon fossil fuels, there will be economic tragedies in the near future.

1.1.2 Environmental impacts

With a growing population around the world, the need for more energy increases as well. Dramatic world wide consumption of fossil fuels has had severe consequences on the environment. Crude oil and its derivatives that are used as primary sources of energy and are constantly in high demand. In order to meet this demand in the most economical fashion, offshore drilling is a common practice by oil companies. However, offshore drilling is devastating to the environment in several ways. As a result of the equipment and methods used to extract the oil, high levels of pollution are released into the atmosphere, disturbing nearby ecosystems. Secondly, the high level of drilling is consistently depleting the earth's supply of many natural resources. Furthermore, organisms and animals in the areas surrounding the drilling are susceptible to many of the negative side effects of the process. Thus, it is evident that the negative environmental impacts of offshore drilling greatly outweigh any possible economic benefits.

Burning of gasoline and coal releases hazardous gases like CO_2, CO, SO and SO_2, NO_2 [6,7] into the atmosphere giving rise to serious environmental and health issues. Smog is formed when NiO_2 reacts with volatile organic compounds in the atmosphere increasing respiratory problems in humans. The emission of CO_2 has increased 10 times in the last century [8]. In fact between 2007 and 2008, CO_2 emissions from the combustion of coal increased by 3% [9]. In Fig. 1.2 we see the Annual changes in global mean CO_2 concentration (grey bars) and their five-year means.

Global climate change is one of the most severe global environmental consequences. CO_2 emissions are classified as one of the main driving forces behind global warming

today. In Fig. 1.3 we see the Annual global mean temperatures represented by the black dots with linear fits to the data.

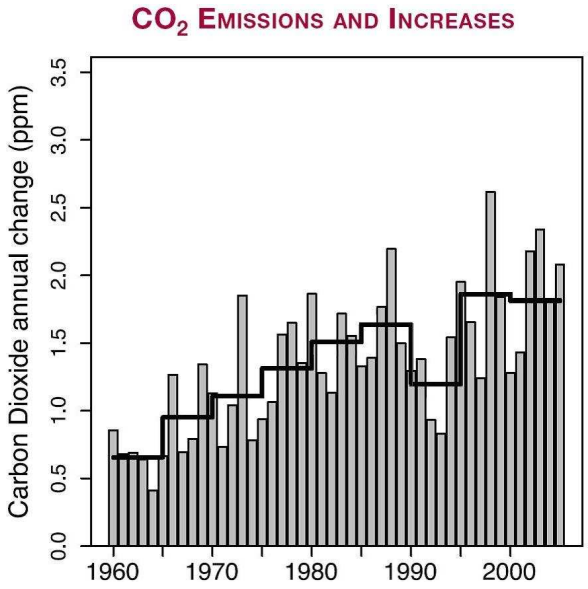

Figure 1.2 – Annual changes in global mean CO_2 concentration

The left hand axis shows temperature anomalies relative to the 1961 to 1990 average and the right hand axis shows estimated actual temperatures, both in °C. Linear trends are shown for the last 25 (yellow), 50 (orange), 100 (purple) and 150 years (red). The smooth blue curve shows decadal variations, with the decadal 90% error range shown as a pale blue band about that line. The total temperature increase from the period 1850 to 1899 to the period 2001 to 2005 is $0.76°C \pm 0.19$°C. We can clearly observe the increase in the world temperature, and this has lead to dramatic climate changes all over the world.

The world's hunger for energy is growing matters of concern; while on the other hand, we need to find a sustainable amount of energy to meet our world's future needs. Despite the hunger for energy, the world will also require an energy that does not produce the greenhouse effect. Fossil fuels have had a crucial role in modern society, but since they are non-renewable and dangerous, we have to reduce our dependence on them and explore alternative energy sources. The amount of power generated from renewable energy sources needs to be increased, as there is little chance of power consumption decreasing. Recognizing these problems, countries around the world are relying more and more on renewable energies, not only for the economic benefits, but also for the environmental benefits. To enable the world to meet the energy demands

at lower rate of energy consumption with corresponding reduction in pollutant and CO_2 emissions a major improvement in energy efficiency of electric power plants and transportation vehicles is required [8].

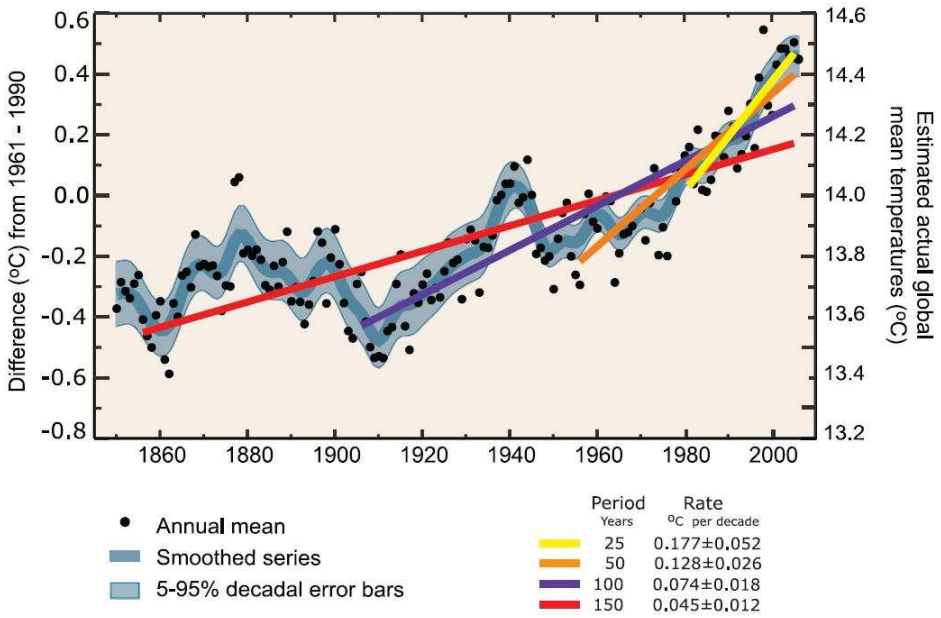

Figure 1.3 – Annual global mean temperatures

Hydrogen economy is an alternative and promising source of fuel. An energy economy based on hydrogen may prove to be a sustainable solution to growing concerns related to increasing energy requirement and greenhouse gas emissions [10].

1.2 Hydrogen

1.2.1 Hydrogen as a future energy carrier

With fossil fuels running out, growing concerns for environment problems, and increase in the requirement of pollution-free energy source, there is an urgent need for an alternate source of energy. Identifying and building a sustainable energy system are the most critical issues to be addressed. Major improvement in energy efficiency and use of emission-free energy would be required.

Hydrogen is considered as a strong candidate and environmental desired clean energy carrier for the future and for this reason, hydrogen based technologies are largely studied [11]. Hydrogen is environmentally friendly and has the highest heating value per mass of all the chemicals [12]. Hydrogen is the most abundant element on

earth, but less than 1% is present in molecular gas form [13]. Hydrogen can be produced in many ways, i.e. from hydrocarbons, electrolysis of water, and processes driven by sunlight to name a few. Unlike electricity, hydrogen can be stored relatively long period of time. Hydrogen can be used in stationary as well as a mobile fuel [1]. Hydrogen energy can also be applicable to heating, cooking, electricity generation, and automobiles like cars, busses etc. [14].

For the past century, the use of gasoline and diesel fuels to power our vehicles has been extremely wasteful but they are still perhaps the best forms of energy in terms of energy density for a given material and ease of refueling and storage. The current designs of the internal combustion engine using gasoline (petrol) as a fuel are only $18 - 20\%$ efficient in producing usable power [15], the rest of the energy produced is wasted in the form of heat-loss, friction etc. Hydrogen gas is considered thermally more efficient than gasoline primarily because it burns better in air and permits use of higher compression ratio [16].

Utilization of hydrogen for power generating, fuel for mobile applications, and energy storage for portable devices, will help to control and reduce the negative effect of fossil fuels in environment. Proton exchange membrane (PEM) or other types of fuel cells are attracting more and more attention as clean and efficient power generation devices.

1.2.2 Fuel cell

The fuel cell offers great promise as a pollution free power source for various applications ranging from mobile phones to automobile [17–19]. Hydrogen fuel cells will more than likely eventually replace the internal combustion engine entirely. Hydrogen is much more efficient and safer than the internal combustion engine. As they do not have any moving parts, they are also very quite and reliable. Lithium ion batteries that power laptops, cell phones and other electronic devices, deteriorates with time and use; whereas a fuel cell potentially has an unlimited life time for as long as the fuel is supplied the fuel cell will continue to generate power.

The power generation process in a fuel cell is analogous to that of a battery, i.e. converting chemical energy to electrical energy. A fuel cell combines hydrogen and oxygen to produce electricity, with water and heat as its by-product. Thus, it is a so-called zero emission engine. [20].

There are several types of fuel cells currently under development, each with its own advantages, limitations, and potential applications. They are differentiated by the kind of electrolyte, chemical reaction, fuel, catalyst and temperature required for

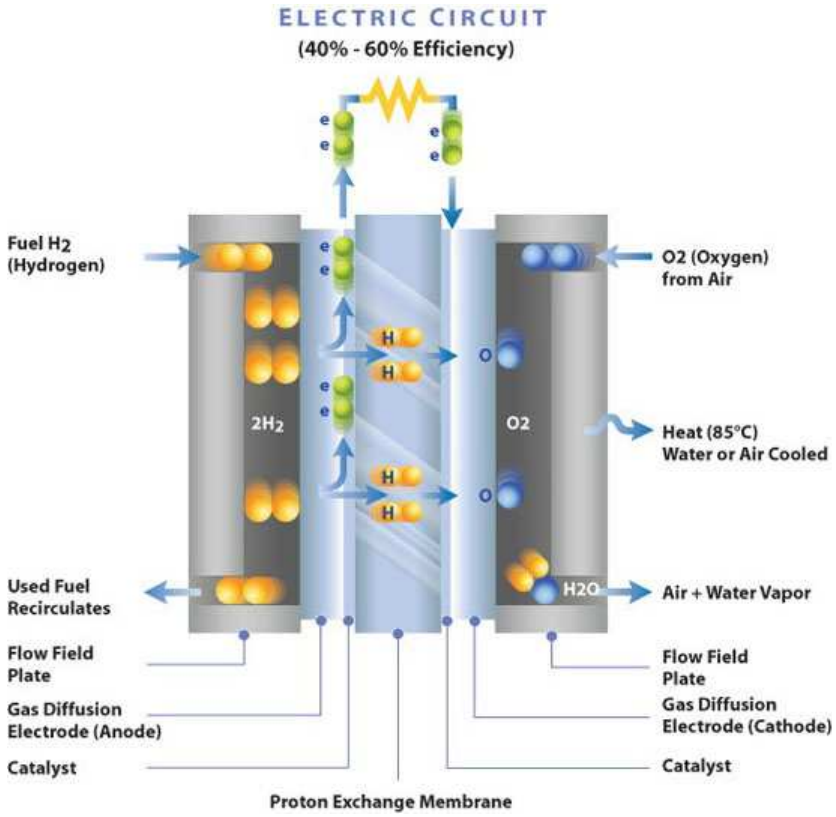

Figure 1.4 – Basic design of a fuel cell [22]

its functioning. Polymer Electrolyte Membrane Fuel Cell (PEMFC), Direct Methanol Fuel Cell (DMFC), Alkaline Fuel Cell (AFC), Phosphorous Acid Fuel Cell (PAFC), Solid oxide Fuel Cell (SOFC) to name a few [21]. Most of the fuel cells have similar basic design. A single fuel cell is made from several layers of different materials as seen in the Fig. 1.4. The three key layers in fuel cell are the Anode, Cathode, and Electrolyte. The electrodes are porous and normally made of carbon cloth or carbon fiber [23]. The polymer membrane is sandwiched between the two electrodes. At the interface between the electrode and the polymer membrane there is a layer with catalyst particles (typically platinum supported on carbon) [23]. The Anode is the negative side of the fuel cell, and allows the flow of hydrogen, the platinum catalyst layer between the anode and the electrolyte assists in splitting of the Hydrogen to electrons and protons. The anode then conducts electrons to the external circuit, while protons travel through the membrane. The cathode is the positive side of the fuel cell, it conducts the electrons back from the external circuit to recombine with hydrogen ions and oxygen to form water. For basic fuel cell reaction see eq. 1.1 - 1.3 [24].

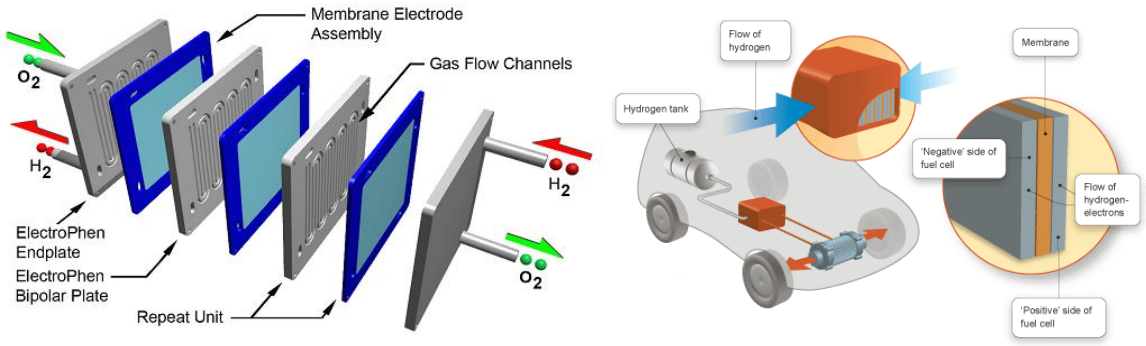

Figure 1.5 – Fuel cell stack

$$Anode: \ H_2 \rightarrow 2H^+ + 2e^- \tag{1.1}$$

$$Cathode: \ {}^1\!/_2 O_2 + 2H^+ + 2e^- \rightarrow H_2O \tag{1.2}$$

$$Overall: \ H_2 + {}^1\!/_2 O_2 \rightarrow H_2O \tag{1.3}$$

Hydrogen, Methanol, natural gas and gasoline can be used as fuel in a fuel cell. To avoid exhaust of carbon dioxide gas, PEMFC is considered to be the best option [17]. PEMFC use pure hydrogen as fuel so there is no need for fuel processor, and the by-product is pure water. A typical fuel cell can produce between 0.5 and 0.9 V of DC electricity [8]. To produce the required amount of voltage, single fuel cells are stacked together to have a fuel cell-stack as seen in Fig. 1.5.

Some fuel cells can work on hydrogen rich fuels (Ethanol and hydrocarbon), the hydrogen is generated inside the fuel cell using reformers. DMFC uses methanol as the fuel, that is mixed with steam and fed in to the anode. The catalyst in this fuel cell is very sensitive to impurities and thus affecting the life span of the fuel cell. The catalyst in AFC works at temperature ranging between 100 ^{o}C and 250 ^{o}C and is easily poisoned by CO_2. PAFC are based on phosphoric acid as the electrolyte. They are more tolerant to impurities but are large and bulky. SOFC does not need a catalyst but operates at 1000 ^{o}C thus requiring a start-up time. Secondly high temperature is a big disadvantage for vehicular applications. Considering its low temperature operation and being environmental friendly, PEMFC are currently in focus of research as they are promising candidates. For proper functioning and having a better life time of the fuels cells it needs to be fed with pure hydrogen.

1.2.3 Production, storage and transportation of hydrogen

The most economical way to produce hydrogen is by Steam Methane Reforming (SMR) of natural gas, most of the hydrogen at industrial level is produced by SMR [25]. Steam reforming involves the endothermic conversion of methane and water vapour into hydrogen and carbon monoxide in presence of active nickel catalyst. The resultant gas contains approximately 12% CO, which can be further converted to CO_2 and H_2 through the water-gas shift reaction.

$$CH_4 + H_2O + heat \rightarrow CO + 3H_2 \tag{1.4}$$

$$CO + H_2O \rightarrow CO_2 + H_2 + heat \tag{1.5}$$

Hydrogen can also be produced from fossil fuels using other techniques like Partial Oxidation and Autothermal Reforming [26], but the hydrogen produced by all of these methods are not pure and may contains impurities like CO_2, CO and Sulphur and needs further purification.

Another way to produce hydrogen is by water splitting [27]. The process involved is splitting of water into hydrogen and oxygen by the application of external energy (see eq. 1.6)

$$H_2O + energy \rightarrow H_2 + \frac{1}{2}O_2 \tag{1.6}$$

The hydrogen produced by this process is pure, clean and free from carbon and sulphur impurities. Unfortunately, this process requires a lot of energy, making the process very expensive relative to steam reforming of natural gas.

Even after production of pure hydrogen, one of the main obstacles to the widespread as an energy carrier, are related to the unsolved problems concerning its storage and distribution [13, 28]. For successful application of hydrogen in stationary and automobile application, hydrogen storage is important. Secondly, the volumetric and gravimetric density is also a critical issue [12, 29]. The most studied hydrogen storage systems for storage and transport are high pressure tanks, liquid hydrogen [30], hydrogen stored in metal hydrides and chemical hydrides.

A classical high pressure tanks is made of inexpensive steel and can hold up to 300 bar, and are normally filled up to 200 bar. So storing 4 Kg of hydrogen will require 225 liters. Carbon-fiber reinforced composite materials are also being considered,

that can hold up to 600 bar. These type of tanks need special inner coating to avoid high pressure hydrogen reaction [13]. Manufacturing and maintaining of such kind of tanks would also add to the cost. Energy would be spent in making and storing the hydrogen as well. High pressure tanks could also be dangerous for transportation and can be a risk in automobiles. Other way to store hydrogen is in the form of liquid. The mass per volume of hydrogen can be increased by condensing it to liquid. The condensation temperature of hydrogen at 1 bar is -252 ^{o}C. The liquid hydrogen also has problem of hydrogen loss as the containers are open system to prevent strong over pressure. Considering the energy spent to liquefy hydrogen and the loss from the tank, they are not an ideal way to store and carry hydrogen to be used for fuel cells.

Metal hydrides are also considered for hydrogen storage, but have kinetic problems. Chemical hydrides like Sodium borohydride ($NaBH_4$) [31–34], Ammonia Borane (NH_3BH_3) [35, 36], Lithium borohydride ($LiBH_4$) [37], Potassium borohydride (KBH_4) [38], etc. with high hydrogen storage capabilities have drawn a lot of attention in recent years as a hydrogen carrier. Chemical hydrides are considered as a breakthrough for its safe hydrogen storage capabilities [34]. $NaBH_4$ and NH_3BH_3 high hydrogen storage of 10.6 $wt\%$ and 18 $wt\%$ respectively [16, 35]. They are non toxic and extremely stable in air. Large amount of pure hydrogen gas is released during the hydrolysis of these chemical hydrides in presence of appropriate catalysts. The by-product obtained after the generation of hydrogen can be recycled. Chemical hydrides seem to be the most potential candidates to supply pure hydrogen for fuel cell to be used for portable application.

1.3 Chemical hydrides for hydrogen storage and production.

Chemical hydrides appear as capable and promising solution to overcome the issue related to hydrogen safety and handling and to be competitive with respect to conventional fuel. Ammonia borane (NH_3BH_3) and Sodium borohydride ($NaBH_4$) with high gravimetric and volumetric hydrogen storage ability are the most prospective candidates to supply pure hydrogen for portable and on-board application at room temperature [39, 40]

1.3.1 Sodium borohydride

$NaBH_4$ is a crystalline white thermally stable substance. It is a powerful reducing agent and is extensively used in wastewater processing and paper bleaching [16]. $NaBH_4$ in presences of appropriate catalysts, hydrolyse to produce clean hydrogen gas. Aqueous $NaBH_4$ seems to be an ideal hydrogen source for the following reasons [41]:

- $NaBH_4$ solution is non-flammable and is stable in air for months.
- It has a H_2 storage capability of $10.8\,wt.\%$
- H_2 produced is clean, without any impurities.
- H_2 generation can be controlled in presence of selected catalysts .
- The reaction product, Sodium borate ($NaBO_2$), obtained after de-hydrogenation of $NaBH_4$, is environmentally clean and can be recycled to generate the reactant.
- H_2 can be generated even at $0\,^{\circ}C$.
- H_2 is generated by water-based hydrolysis reaction of $NaBH_4$, during which half of the hydrogen is produced from the water solvent.

In the 1950s, Schlesinger et al. [42] first observed that $NaBH_4$ in presence of appropriate catalysts, at room temperature, could be hydrolysed to H_2 gas and Sodium borate, $NaBO_2$ (see eq. 1.7).

$$NaBH_4 + 2H_2O \rightarrow 4H_2 + NaBO_2 + Heat\ (300\,kJ) \tag{1.7}$$

$NaBH_4$ self hydrolyse even in the absence a catalyst for solution having pH$<$ 9. The rate of decomposition of the aqueous borohydride solutions is expressed by its half-life as a function of pH and temperature [43].

$$log(t_{1/2}) = pH - (0.034T - 1.92) \tag{1.8}$$

where, $t_{1/2}$ is indicated in minutes and T in Kelvin. Sodium hydroxide (NaOH) is added to $NaBH_4$ solution to increase the self-life of the solution, by making the solution strongly alkaline [44]. Schlesinger et al. [42] studied effects of many acids for

the hydrolysis of $NaBH_4$ (like inorganic protic acids, oxalic acid, phosphorus pentoxide, aluminium chloride). These acids could hydrolyse the $NaBH_4$ solution, but the reaction could not be controlled. In 1985 Kaufman et al. studied the effect of some metals (Cu, Ni, and Co) and their salts on the overall hydrogen production [45]. Suda et al. [46] examined the effect of fluorinated metal hydrides catalyst on the hydrolysis of alkaline $NaBH_4$. Kojima et al. [47] studied the effect of Pt metal coated on metal oxide. Amendola et al. [16] reported the application of Ru-catalyzed hydrolysis of aqueous BH_4^- solution as hydrogen generator for PEMFC. Precious metals like Pt [48] and Pd supported on carbon [49], PtRu supported on metal oxide [50], Ru on polymer [51], Ru nanoclusters [52] have been extensively studied as catalysts and have shown excellent catalytic activities. These kinds of catalysts are quite expensive and cannot be considered due to their high cost. Some metals, such raney Ni and Co, and even nickel and cobalt borides [53–56], are also used to accelerate the hydrolysis reaction of $NaBH_4$.

1.3.2 Ammonia Borane

Recently, Ammonia borane (NH_3BH_3, AB) has attracted increasing attention as an efficient hydrogen storage material because of its high hydrogen content. AB can produce hydrogen by either hydrolysis or thermolysis [57] and the end product, which is nontoxic and environmentally safe, can be recycled to regenerate AB [58]. While thermolysis of AB requires moderate temperature, the catalytic hydrolysis can generate sustained amount of hydrogen even at room temperature (see eq. 1.9)

$$NH_3BH_3 + 2H_2O \rightarrow NH_4^+ + BO_2^- + 3H_2 \tag{1.9}$$

Along with $NaBH_4$, AB is also considered as promising candidate to supply pure hydrogen for portable and on-board application at room temperature [39, 40] because of their following properties:

- AB has H_2 storage capacity of 19.6 $wt\%$.
- They has low molecular weight of 30.7 g/mol [39, 59].
- High gravimetric and volumetric hydrogen storage ability.
- AB is highly stable and soluble in water and do not need alkaline solution like in the case of $NaBH_4$.

- The end product, which is non toxic and environmentally safe, can be recycled.

The hydrolysis reaction rate can be effectively increased by using several inorganic and organic acids but the reaction usually becomes uncontrollable. On the other hand, solid state catalysts such as precious and transition metals and their salts are found to be very efficient in accelerating the hydrolysis reaction in a controllable manner. Noble catalysts like Pt, Rh, and Ru supported on Al_2O_3 [60], Carbon [61, 62] and on TiO_2 [63], K_2Pt_6Pt [64], and nanoclusters of Pd(0) [65], Ru(0) [66] and Rh(0) [67] have been utilized in the past to enhance the hydrogen production rate. However, these catalysts do not seem to be viable for industrial application considering their cost and availability. Transition metals such as Co supported on Al_2O_3, SiO_2 and C [68]; Co(0), Ni(0) and Fe(0) nanoclusters [69–71], Ni based alloy [72], and Ni-SiO_2 nanospheres [73] are generally used to accelerate the hydrolysis reaction of NH_3BH_3. The hydrolysis reaction can be effectively controlled by means of heterogeneous catalyst. Although noble metals like Pt, Rh, and Ru [57, 58, 74] are highly active catalysts for hydrogen production, their viability for industrial application is uncertain considering their cost and scarcity.

1.4 Thesis Overview

In the present chapter, we have discussed the need for clean energy for the future. We have seen how hydrogen can be a promising solution as a future energy source, especially for vehicular applications and portable devices. Hydrogen can be produced by catalytic hydrolysis of chemical hydrides using appropriate catalyst. This hydrogen can then be supplied to fuel cell to produce electricity. The aim of this thesis is to present catalysts that are economical, easy to synthesise and also have a high hydrogen production rate. ***Chapter 2*** describes the techniques for catalysts preparation and the experimental setup that was used to carry out all the hydrogen generation measurement. In ***Chapter 3***, we see that doping nickel or phosphorous in Co-B powder enhances the catalytic activity to obtain a higher hydrogen generation rate for hydrolysis of $NaBH_4$. We discuss the enhanced catalytic activity by studying the surface electronic states and composition of the catalysts. After having understood the role of Ni and P in Co-B catalyst, we prepare Co-Ni-B-P catalyst, which has a superior catalytic activity compared to Ni or P doped catalyst. In ***Chapter 4***, we will discuss how doping various transition elements (i.e., Cu, Cr, Ni, Fe, Mo and W at different molar ratios) in Co-B catalyst, enhances the catalytic hydrolysis of $NaBH_4$.

We study and discuss the role of each doped element in the enhanced catalytic activity. Later, we also put these doped catalysts through an endurance test, to check if these catalysts can conserve its enhanced properties and withstand against high temperature, exposure to environment (with time), and extensive use. In ***Chapter 5***, we synthesise film catalysts of Co-B-P using electrolysis deposition and pulse laser deposition (PLD). We will see how films catalysts are better than powder catalyst and can be prepared in a controlled manner. We also discuss the enhanced catalytic effect of the films and the role of nanoparticle prepared by PLD. We also produce film of Co-B on Carbon using PLD. In ***Chapter 6***, we study the catalytic hydrolysis of AB using the doped Co-B powder catalyst; we also study the hydrolysis of AB using film catalyst of Co-B and Co-B on carbon produced by PLD.

Chapter 2

Experimental Techniques

"All the breaks you need in life wait within your imagination, Imagination is the workshop of your mind, capable of turning mind energy into accomplishment."
-Napoleon Hill

2.1 Catalyst preparation techniques

2.1.1 Preparation of Powder catalyst

Co-B powder catalyst is synthesised by chemical reduction method. In a typical procedure, an appropriate amount of cobalt chloride, $CoCl_2$ (Sigma-Aldrich) is reduced using $NaBH_4$ at room temperature (see eq. 2.1). The molar ratio of $NaBH_4$ and $CoCl_2$ was kept larger than 2 to ensure complete reduction of $CoCl_2$. $NaBH_4$ solution was added drop wise in a glass beaker containing the aqueous solution of $CoCl_2$. The mixture is stirred using a magnetic stirrer until hydrogen liberation stops from the solution.

$$2CoCl_2 + NaBH_4 \rightarrow Co_2B + NaCl + \frac{1}{2}H_2 \tag{2.1}$$

The resulting black powder, separated from the solution during the reaction, is collected using a filtration process. The powder is extensively washed with distilled water a few times in order to remove Cl^- and Na^+ ions (presence of these ions may poison the catalytic activity of Co). The powder is finally washed with ethanol (99.9%) and then dried in continuous nitrogen flow at around 323 K.

Co-Ni-B powder catalyst can also be prepared following a similar procedure. An aqueous solution of cobalt chloride ($CoCl_2$) and nickel chloride ($NiCl_2$) is prepared. The solution is then reduced using $NaBH_4$ at room temperature with continuous stirring . The same procedure is used for washing and drying the powder as used for Co-B. The $\frac{Co}{Co+Ni}$ molar ratio in the final Co-Ni-B powder can be adjusted by varying the concentration of Co and Ni salts in the starting solution. Similar procedures have been followed to synthesise powders of Co-Fe-B, Co-Cu-B, Co-Cr-B, Co-Mo-B, Co-W-B. $\frac{M}{Co+M}$ molar ratio is denoted by χ_M, where, M = Ni, Fe, Cu, Cr, Mo and W.

2.1.2 Thin film using PLD

The experimental set-up is schematically represented in Fig. 2.1. The energy source used in the experiments is a KrF ($\lambda = 248\,nm$) excimer laser (LPX220i Lambda Physik) capable of operating at frequencies between $1 - 200\,\mathrm{Hz}$. The pulse width is about $20\,ns$ (FWHM) and the maximum pulse energy is $450\,mJ$, having a maximum average power of $80\,W$. The pulse energy can be lowered by dropping the pumping high voltage. The beam dimensions are $8\,mm \times 23\,mm$ (vertical x horizontal), with the beam divergence of $1\,mrad \times 3\,mrad$ (V x H). The beam is deflected by 90° using a dielectric mirror. The beam can be focused by a $30\,cm$ focal length lens mounted on a slide permitting it to be moved along the beam direction.

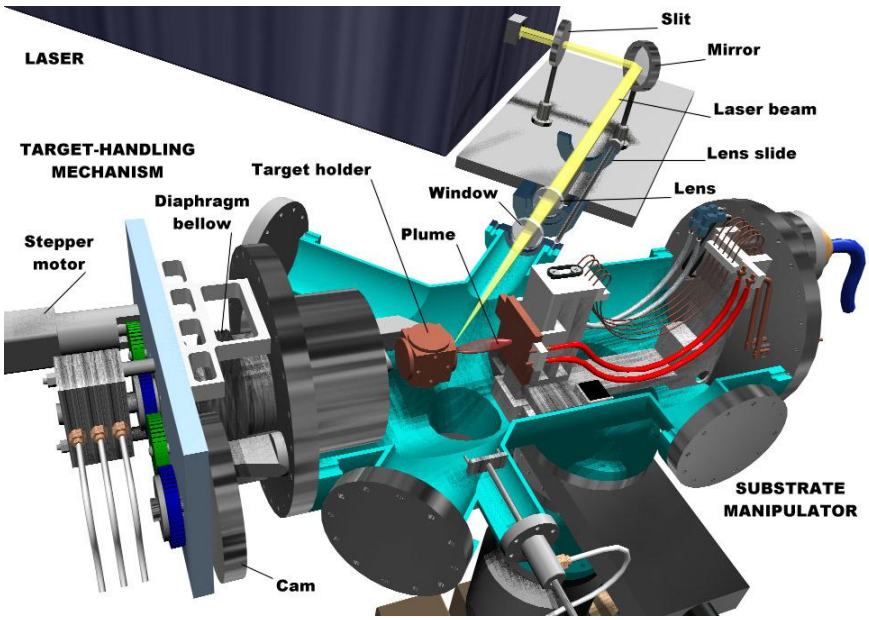

Figure 2.1 – 3D view of our PLD apparatus. [75]

The slide is used to change the energy fluence on the target. The focused beam finally enters the chamber through a fused silica window and impinges on the target at 45°. To prepare catalyst films, the catalyst powder is first synthesised using the above mentioned procedure. The powder is then cold pressed to cylindrical disks in a stainless steel holder and is used as a target. PLD is performed at a repetition rate of 20 Hz. Films are deposited on silicon substrates for the characterization and on glass substrates for testing its catalytic activity. For ablation in vacuum ($2 \times 10^{-4} Pa$), the laser fluence is varied from 1 to 10 J/cm^2. Deposition can also be carried out under different Ar gas pressure in chamber by using the laser fluence as required. Ar gas can be introduced in the chamber through mass flow controller and pumping is throttled in order to maintain desired gas pressure. The target to sample distance is maintained at 4 cm. Weight of the catalyst films is evaluated by measuring the weight of the glass substrate (76 $mm \times 46\,mm$), before and after deposition, and can be kept approximately constant for all laser fluences by varying the number of laser pulses during deposition.

2.1.3 Catalyst on Ni foam using Electroless Deposition

Ni-foam (Inco Co. LTD, density = 380 g/m^2, pore size = 590 μm, thickness = 1.7 mm) was selected as support for catalyst films for its high surface area provided by its porous structure. Square specimen (2 $cm \times 2\,cm$) of Ni-foam is ultrasonically cleaned with acetone followed by NaOH solution to remove any kind of lubricants. The surface of specimen was deoxidized and activated by immersing it in HCl solution for 2 min and then washed with distilled water and dried at 323 K in N_2 atmosphere. This pre-treated Ni-foam specimen is then immersed in aqueous solution containing 0.1 M of cobalt chloride ($CoCl_2$) and sodium hypophosphite (NaH_2PO_2) for 1 min at room temperature under stirring condition. Equal volume of $NaBH_4$ solution (0.25 M) was then poured in the solution. The Ni-foam was removed from the mixture once the bubble generation was ceased. The previous immersion step was repeated several times in order to obtain several layers on the Ni-foam support. Finally the Ni-foam was extensively washed with distilled water and ethanol before drying at around 323 K under continuous N_2 flow. The molar ratio of $\frac{P+B}{Co}$ and B/P was kept as desired by selecting appropriate amount of $CoCl_2$ and NaH_2PO_2. The weight of Co-P-B film was evaluated by measuring the weight of Ni-foam specimen before and after deposition.

2.2 Hydrogen Measurement Set up

2.2.1 Experimental setup

The reaction chamber is composed of a cylindrical flat flange vessel (DuranR glass, 250 ml maximum capacity, HWS) with off-centre bottom outlet valve and a stirrer guide at the bottom (see Fig. 2.2). It is surrounded by a jacket connected to a heating circulator bath (Thermo C10, Haake) for temperature control. The temperature is controlled within ± 0.1 K by a water bath with a digital temperature controller. The reactor is closed by a flat flange lid (Duran® glass, HWS) with five necks 29/32 NS type (a central socket, two angular side sockets and two parallel side sockets).

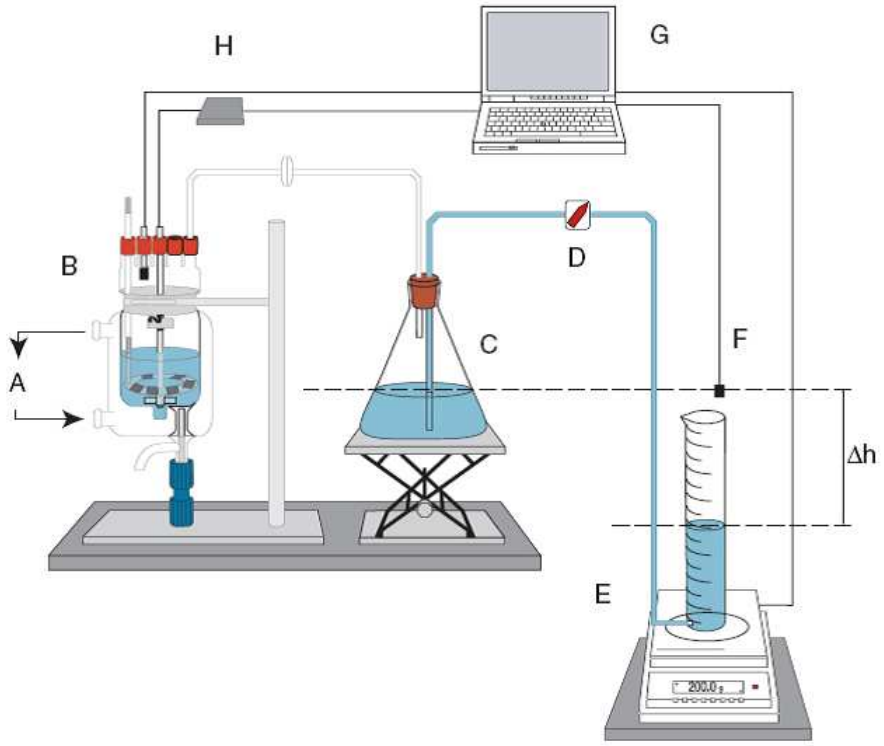

Figure 2.2 – Schematic diagram of the experimental apparatus for GV analysis: (A) thermostatic water bath system, (B) reaction chamber, (C) Erlenmeyer flask with water reserve and elevator, (D) stopcock, (E) graduated cylinder and electronic balance, (F) external pressure sensor, (G) input-output board and acquisition software, (H) stepper motor controller. The height-difference $\triangle h$ between the water level contained in the chamber-flask system and that in the cylinder is also indicated. [76]

A quick release clamp with a VMQ O-ring maintains the sealing. The entire device is supported by a quick fixing Vario-Grip® group with additional clamping

unit allowing removal of the vessel or of the lid without disassembling the accessories. Screw-thread tubes with standard ground cones are connected to the lid sockets, while sensor, probe and tubes are locked by PTFE screw joints with GL thread. The central socket was assigned to the stirrer system. The conventional outlying electrical unit was replaced with a stepper motor ($M42SP-7$ model with explosion-proof feature) placed inside the reactor and controlled with a 2/2.5 A bipolar stepper motor drive module ($GS-D200S$, $SGS-THOMSON$ Microelectronics). This configuration permits a very simple procedure to remove the lid and ensures low wear of the components. A pressure sensor ($XFAM-115KPASRH$ sensor, Fujikura) is placed in one of the angular side sockets and a second sensor is placed outside the reactor to follow the ambient pressure. Hydrogen evolved from the chemical reaction can flow through the second angular side socket which is connected to the measurement system through a polyurethane tube (5 mm inner diameter). One of the parallel side sockets is devoted to the insertion device which is made up of a tube (inner diameter $8mm$) with a PVC rod inside (diameter 7.8 mm). Along the rod three slots have been provided for a PTFE O-ring of the right size. The ISP module is connected to the bottom of the rod. The last socket is sealed with an NS glass tap, and it is available for additional devices (for instance a probe for pH monitoring). This configuration ensures an air-tight seal of the whole system with a maximum inlet pressure up to 105 Pa relative to the ambient pressure.

All electronic devices are controlled via a PC through a data acquisition board (NI–6036E, National Instruments) with dedicated software developed in our laboratories by using LabVIEW6.1 (National Instruments). In particular, it reads inlet and outlet pressure with two analogue inputs ($0.0-5.0\,V$, reference single ended, 0.5 duty cycle), controls the stepper motor drive module with three digital lines and a clock line (frequency and direction of rotation) and collects the experimental data both acquired with a GV system and FM in a text file, thanks to an RS232 line (the GC system uses a proprietary program).

2.2.2 Gas Volumetric Method

A typical experiment consists in the addition of 200 ml of the alkaline solution of $NaBH_4$ 0.025 M to the reaction chamber. The catalyst (in the form of a film, powder or liquid) is placed on the ISP module, connected to the insertion device and fixed to the reactor lid. The latter is placed on the reaction chamber and sealed with a clamp. The system internal pressure (P_0), with stopcock still closed, is the same as atmospheric, as shown in Fig. 2.3. Using the Bernoulli law, we can describe the

pressure contribution experienced by the liquid in the flask (left term, where $P_0 = P_{atm}$) and in the cylinder (right term) as follows:

$$P_0 > P_{atm} - \rho g \triangle h_0 \tag{2.2}$$

where $\triangle h_0$ is the difference in the water level between the flask and the cylinder with the stopcock closed, as shown in Fig. 2.2.

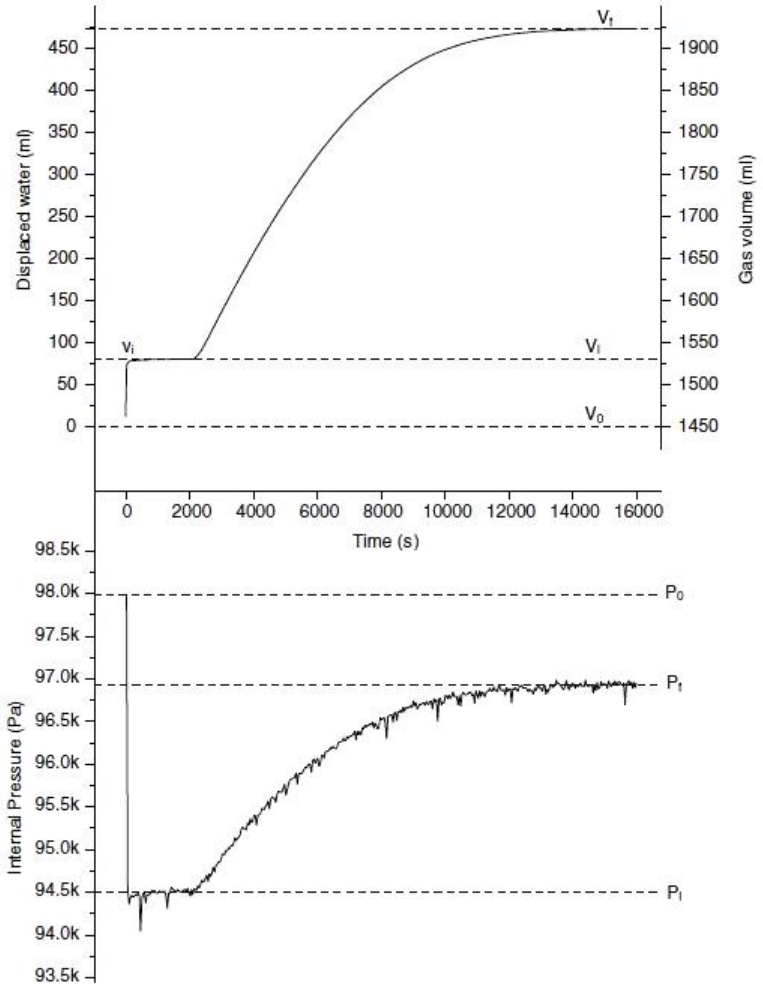

Figure 2.3 – Volume and pressure change when Co–B catalysed hydrolysis takes place

After adjusting the suitable balance controls (calibration in ambient conditions and taring) the stopcock is opened (see Fig. 2.3, $t = 0$). A small amount of water flows towards the cylinder, because of the level difference between the latter and the flask, and the internal pressure drops. When a new hydrostatic equilibrium for the

given initial condition is reached the pressure, P_i, remains constant ($0 < t < 2000\,s$):

$$P_i(< P_{atm}) = P_{atm} - \rho g \triangle h_1 \tag{2.3}$$

where h_1 is the new altitude difference in the liquid level between the two containers. Once hydrostatic equilibrium is reached, the catalyst is dipped into the solution ($t = 2000\,s$) and reaction starts. As a result of hydrogen evolution the pressure inside the reactor flask increases causing a water flow from the Erlenmeyer flask towards the graduated cylinder, inducing a new temporary equilibrium pressure condition. The displaced volume of water, as a function of produced hydrogen, is continuously monitored by the electronic balance until the reaction ends, ($P(t) = Pf, V(t) = Vf$).

The mathematical expression for the number of moles of evolved hydrogen $n_{H_2}(t)$ is derived from the ideal gas law as follows. At the beginning of the measure ($t = 0$):

$$P_0 V_0 = n_{air} RT \tag{2.4}$$

where $P_0 = P_{atm}$ and $V_0 = (1450 \pm 20)\,ml$ is the volume of air in the reactor-flask system.

During the measurement, and therefore with the production of gaseous hydrogen, the equation becomes

$$P(t)V(t) = (n_{air} + n_{H_2}(t))\,RT \tag{2.5}$$

where $V(t)$ is given by the sum of the initial volume of air and the volume of water displaced :$V(t) = V_0 + v(t)$

Hence, from equations (4) and (5) the expression for the estimation of the number of moles of hydrogen evolved can be obtained:

$$n_{H_2}(t) = \frac{P(t)V(t)}{RT} - \frac{P_0 V_0}{RT} \tag{2.6}$$

The mathematical expressions for time dependence of gas yield (%) and the rate ($ml\,min^{-1}g^{-1}$) as a function of the controlled variables are given by

$$Yield_{H2} = \frac{n_{H_2}(t)}{4n_{BH_4^-}} \tag{2.7}$$

where $n_{BH_4^-}$ is the number of moles of borohydride added, and

$$Rate_{H_2} = \frac{dv(t)}{dt} \tag{2.8}$$

is the rate of evolved hydrogen in millilitres per minute and grams of catalyst.

Chapter 3

Powder catalyst for hydrolysis of alkaline $NaBH_4$

"All invention and progress comes from finding a link between two ideas that have never met."
-Theodore Zeldin.

3.1 Introduction

The efficiency of hydrogen production by hydrolysis of $NaBH_4$ can be significantly enhanced by use of appropriate catalyst during the reaction. Many organic and inorganic acids are able to effectively enhance the hydrolysis reaction rate; however the reaction usually becomes uncontrollable [42]. On the other hand, solid state catalysts such as noble (generally functionalized with support) or transition metals and their salts are found to be very efficient in accelerating the hydrolysis reaction in a controllable manner. Catalysts like Ru supported on anion-exchange resin [16], fluorinated Mg based alloy [46], Pt [48] and Pd supported on carbon [49], PtRu supported on metal oxide [50], raney Ni and Co, and even nickel and cobalt borides [53, 77, 78] are generally used to accelerate the hydrolysis reaction of $NaBH_4$. Co and Ni borides are mostly considered as good candidates for catalyzed hydrolysis reaction of $NaBH_4$ owing to their good catalytic activity and low cost. These catalysts can be effortlessly synthesized by a simple procedure of chemical reduction method in which transition metal ions are brought to the metallic state by reducing agent [77]. Non-noble metals (Co and Ni) demonstrate the better activity only when used in boride form, because boron is able to protect the active metal sites (Co or Ni) from oxidation by electron transfer [79].

Elements like boron (B) or phosphorous (P), have been used with Co (Co-B, Co-P) or Ni (Ni-B, Ni-P) to bring variation in the electronic states of the active metals for superior catalytic activity [80, 81]. This shows that elements like boron or phosphorous affect the surface properties of catalysts and, hence enhance their catalytic properties. In the past, it was also reported that the catalytic activity of Co-B is enhanced by inclusion of P in the catalyst. Better selectivity and activity were obtained for the hydrogenation of maltose with Co-P-B catalyst powder, as compared to Co-B and Co-P [82]. A similar effect was reported for Ni by Lee at al. [83], where the authors have showed that by just regulating the P/B molar ratios, the ultra fine Ni-P-B amorphous alloy catalyst could be made more efficient for various liquid phase hydrogenation reactions than Ni-B or Ni-P.

In the present Chapter, we prepare Co-Ni-B catalyst with varying Co/Ni atomic ratios in order to establish the optimum condition to have the best efficiency in the catalytic reaction. Co/Ni ratio is an important parameter to determine the efficiency of the catalyst. In addition, we have also compared Co-Ni-B catalyst powder with Co-B and Ni-B in order to understand the role of each atomic element in the catalytic activity. Then, we have synthesized Co-P-B catalyst powders with different B/P molar ratio by chemical reduction method. Superior catalytic behaviour has also been found to be exhibited by Co-P-B powder as compared to Co-B and Co-P powders, which are inferred from the XPS and morphological studies. The core electron binding energies of Co, P, and B obtained from XPS measurements will help us to infer on the electronic states of Co-P-B, Co-B, and Co-P and to suggest their roles in $NaBH_4$ hydrolysis process. After understanding the role of Ni and P doped in Co-B catalyst, it is interesting to investigate the performance of a single mixed catalyst (Co-Ni-P-B) (possibly including a variety of synergic effects in electron transfer to Co) for hydrogen generation by hydrolysis of $NaBH_4$ solution. The molar ratio of B/P and Co/Ni is varied in order to understand the role of composition in the Co-Ni-P-B catalytic activity.

3.2 Ni-doped Co-B catalyst

Effect of different $\frac{Co}{(Co+Ni)}$ molar ratios

Co-Ni-B catalysts were prepared by adding $NaBH_4$ as reducing agent into aqueous mixture solution of cobalt chloride ($CoCl_2$) and nickel chloride ($NiCl_2$) under vigorous stirring at room temperature (see 2.1.1). The $\frac{Co}{(Co+Ni)}$ molar ratio (χ_{Co}) in the Co-Ni-B samples was adjusted by varying the concentration of Co and Ni salts in the

starting solution. Ni-B ($\chi_{Co} = 0$) and Co-B ($\chi_{Co} = 1$) were also prepared in a similar manner, where only $NiCl_2$ and $CoCl_2$ was used in the solution respectively. One set of Co-Ni-B and Co-B powder was annealed at 773 K for $2h$ in Ar atmosphere to study the effect of the lattice structural variation on the catalytic activity.

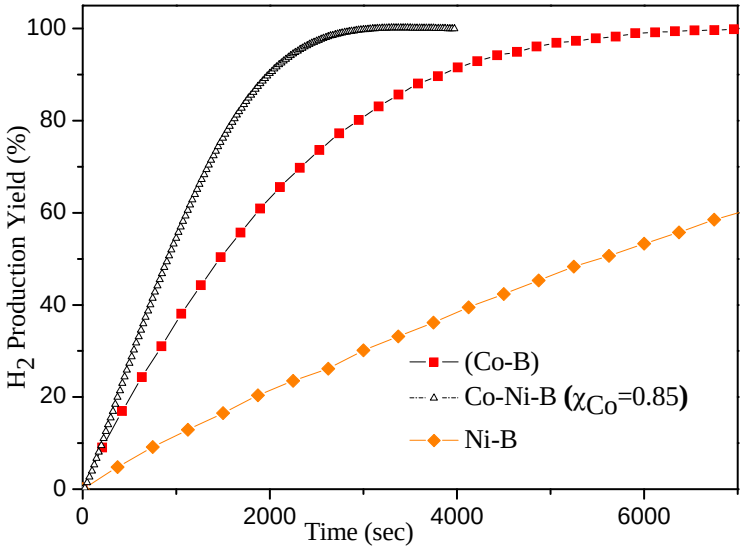

Figure 3.1 – Hydrogen generation yield as a function of reaction time obtained by hydrolysis of alkaline $NaBH_4$ (0.025 M) with Co-B, Ni-B, and Co-Ni-B ($\chi_{Co} = 0.85$) catalyst powder.

Fig. 3.1 presents the hydrogen generation yield as function of time obtained by the hydrolysis of alkaline $NaBH_4$ (0.025 M) solution using Co-B, Ni-B, and Co-Ni-B ($\chi_{Co} = 0.85$) catalyst powder at 298 K. The expected total amount of H_2 has been measured, for all the catalysts used. The generation rate increases initially to a maximum value, and then decreases with time as the $NaBH_4$ concentration decreases in the solution: this suggests the non-zero order of the reaction kinetics. Co-Ni-B ($\chi_{Co} = 0.85$) catalyst shows much better catalytic activity as compared to the same amount ($\approx 15mg$) of Co-B and Ni-B powder. Fitting method[1] has been used to obtain maximum hydrogen generation rates (R_{max}) and are summarized in Table 3.1, Co-Ni-B ($\chi_{Co} = 0.85$) shows the highest R_{max} which is nearly 1.7 and 11.5 times higher than the Co-B and Ni-B powder, respectively.

Fig. 3.2 presents SEM images of Co-B, Co-Ni-B ($\chi_{Co} = 0.85$), and Ni-B powders. Both Co-B and Ni-B are present in form of well-dispersed spherical particles with the average size of about 30 and 18 nm, respectively. In the case of Co-Ni-B catalyst, the

[1] See Appendix A

particles sizes seem to be smaller as compared to other powders, and are difficult to measure as they are embedded in cotton-like filamentary matrix of nanometer size. This kind of morphology may also be helpful to enhance the active surface area of the Co-Ni-B catalyst. XRD pattern (fig. 3.17) of Co-B, Co-Ni-B ($\chi_{Co} = 0.85$), and Ni-B powders showed a single broad peak at around $2\theta = 45^{o}$ thus indicating the amorphous nature of the catalyst powders.

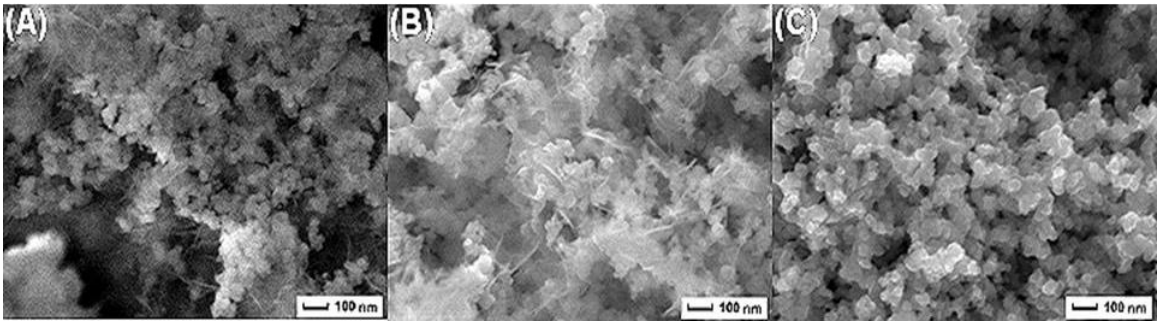

Figure 3.2 – SEM micrographs of (A) Ni-B, (B) Co-Ni-B ($\chi_{Co} = 0.85$) and (C) Co-B catalyst powder

Catalyst powder	$\frac{Co}{(Co+Ni)}$ molar ratio (χ_{Co})	Maximum hydrogen generation rate ($ml/(min\,g)$ catalyst)
Ni-B	0	100
Co-Ni-B	0.50	491
Co-Ni-B	0.65	644
Co-Ni-B	0.75	832
Co-Ni-B	0.85	1175
Co-Ni-B	0.90	779
Co-B	1	681

Table 3.1 – Maximum hydrogen generation rate obtained with Co-B, Co-Ni-B ($\chi_{Co} = 0.50, 0.65, 0.75, 0.85$, and 0.90) and Ni-B powders by hydrolysis of alkaline $NaBH_4$ (0.025 M) solution.

To understand the enhanced activity of Co-Ni-B ($\chi_{Co} = 0.85$), it is necessary to study the surface electronic interaction between the atoms in the compound. Thus, XPS spectra of Co-B, Co-Ni-B ($\chi_{Co} = 0.85$), and Ni-B catalyst powders were acquired and are reported in Fig. 3.3 In all the catalyst powders, two peaks appear in $Co_{2p_{3/2}}$ and $Ni_{2p_{3/2}}$ levels with the binding energies of 778.4 and 781.9 eV for Co,

and 852.8 and 856.3 eV for Ni indicating that metals exist in both the elemental and oxidized states respectively. The peaks due to oxidized Co and Ni are mainly related to $Co(OH)_2$ and $Ni(OH)_2$ which would have been formed during the catalyst preparation reaction between $NaBH_4$ and metal salts [84, 85]. Two XPS peaks with binding energy (BE) of 188.1 and 192.5 eV are also observed for the B_{1s} level, which are assigned to elemental and oxidized boron, respectively [84]. If one compares the BE of pure boron (187.1 eV) [86] with that of the elemental boron in all the catalyst powders there is positive shift of 1 eV. This shift indicates an electron transfer from alloying B to vacant $d-$orbital of metallic Ni and/or Co which makes boron electron deficient while Ni and/or Co metals are enriched with the electron in all the catalyst powders. Electron-enriched metal active sites repel the adsorption of oxygen atoms, while they are strongly adsorbed by the electron deficient B. In other words, alloying B effectively protects metals from oxidation [87, 88]. The BE of metallic Co in Co-Ni-B is 0.2 eV lower than that in the Co-B, whereas BE of metallic Ni in Co-N-B is 0.1 eV lower than that in Ni-B. This proves that in Co-Ni-B catalyst, Co and Ni metals may exchange electrons more easily than the Co-B and Ni-B catalyst: this could be connected to the B-enrichment in Co-Ni-B catalyst as seen by the compositional analysis of XPS spectra (Table 3.2) and also reported by Li et al. [89] who also performed theoretical calculations using Density functional theory (DFT) method to show that the increase of the B content on surface would contribute more electrons to metallic Ni or Co in their corresponding amorphous alloys. The H_2 production from the metal-catalyzed hydrolysis of $NaBH_4$ is proposed to take place by following three kinetics steps[2] [49]. In the first step, BH_4^- ions are chemisorbed on the metal (Ni and/or Co) atoms while in the second step the hydride ion H^- is transferred from BH_4^- ion to an unoccupied adjacent (Ni and/or Co) metal atom. In the last step, this hydrogen atom acquires a negative charge in form of electron from the metal and leaves the site in hydridic form (H^-) which reacts with the water molecule to produce H_2 and OH^- ion. OH^- reacts with boron in BH_3 to produce the $BH_3(OH)^-$ ion. The cycle of hydrogen absorption on the metal sites continues till $BH_3(OH)^-$ forms $B(OH)_4^-$. Molecular hydrogen is released during the full cycle. Looking at the mechanism mentioned above, electron enriched metal active sites will be able to facilitate the catalysis reaction by providing the negative charge electron required by the hydrogen atom in the last step. These electrons are provided by the alloying boron to the active metal sites, as discussed when reporting the XPS results. Thus, the higher concentration of boron in Co-Ni-B catalyst, as compared to Co-B and Ni-B, plays a

[2] See Appendix B

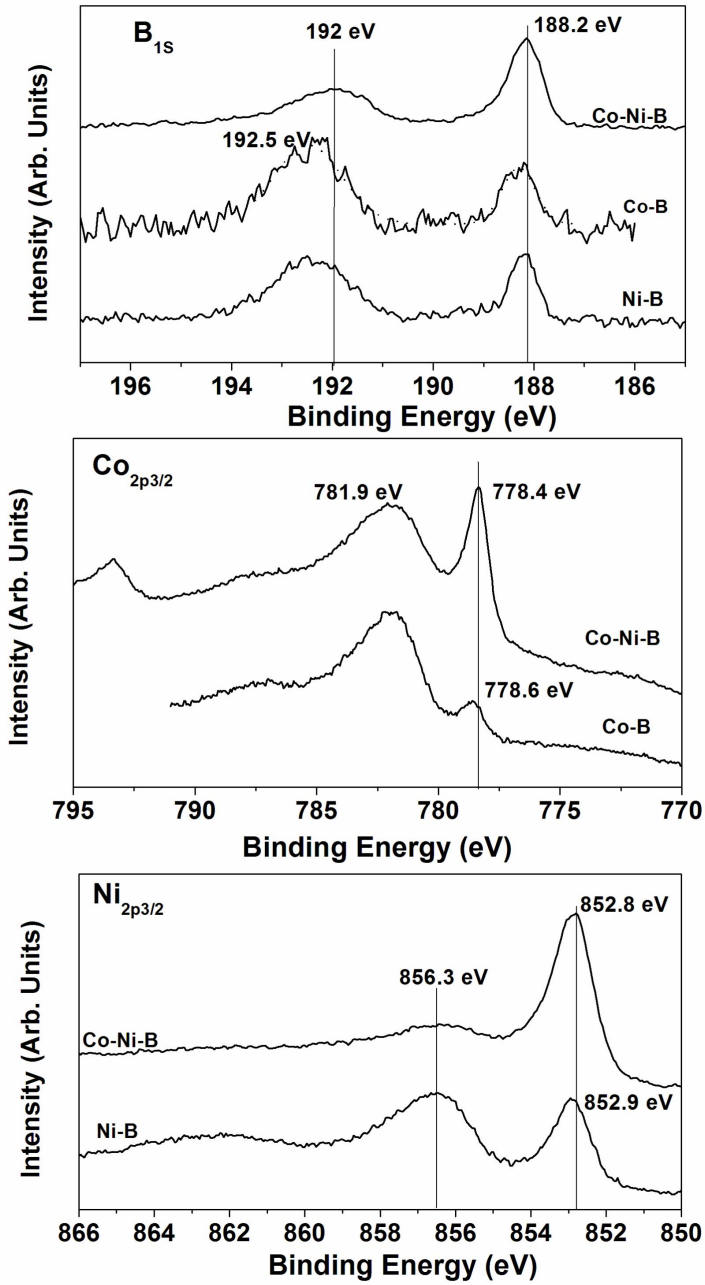

Figure 3.3 – XPS spectra of B1s, $Co_{2p_{3/2}}$ and $Ni_{2p_{3/2}}$ level for Co-B, Ni-B, and Co-Ni-B ($\chi_{Co} = 0.85$) catalyst powder

significant role in enhancing the catalytic activity. Co and Ni molar ratio was varied from $\chi_{Co} = 0.50$ to 0.9 in the Co-Ni-B powder catalyst in order to study the effect of active metal concentration on catalytic activity. The Co and Ni molar ratio was evaluated by EDS and XPS.

Catalyst powders	Co ($at.\%$)	Ni ($at.\%$)	B ($at.\%$)
Co-B	64	-	36
Co-Ni-B ($\chi_{Co} = 0.85$)	50	9	41
Ni-B	-	64	39

Table 3.2 – Surface atomic composition of catalyst powders obtained by the XPS spectra

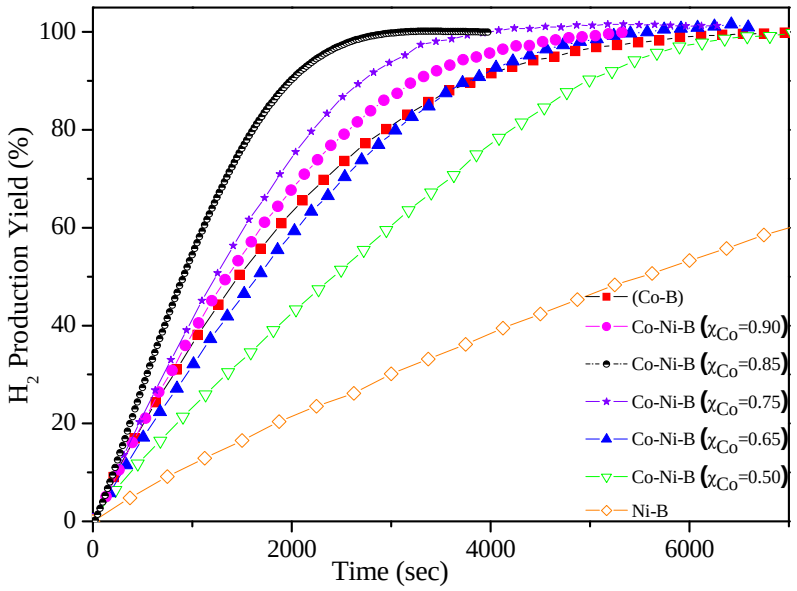

Figure 3.4 – Hydrogen generation yield as a function of reaction time obtained by hydrolysis of alkaline $NaBH_4$ (0.025 M) with Ni-B, Co-Ni-B (Co = 0.50, 0.65, 0.75, 0.85, and 0.90) and Co-B catalyst powder.

Fig. 3.4 presents the hydrogen generation yield as function of time measured by hydrolysis of alkaline $NaBH_4$ (0.025 M) solution using Co-Ni-B catalyst powder with different molar ratio of Ni and Co. The corresponding maximum H_2 generation rate (R_{max}) is report in Table 3.1. R_{max} obtained by pure Ni-B catalyst is always lower than that measured by other powders containing Co. By increasing the Co content

relative to Ni in the Co-Ni-B powder, the rate increases and reaches the highest R_{max} of about $\sim 1175 ml/min/g$ for molar ratio of Co = 0.85 which is even superior than pure Co-B powder. With further increase of the molar ratio χ_{Co} to 0.9, the activity of the powder decreases. The catalytic activity of the powders decrease in following order: Co-Ni-B($\chi_{Co} = 0.85$) > Co-Ni-B($\chi_{Co} = 0.75$) > Co-Ni-B($\chi_{Co} = 0.90$) > Co-B($\chi_{Co} = 1$) > Co-Ni-B($\chi_{Co} = 0.65$) > Co-Ni-B($\chi_{Co} = 0.50$) > Ni-B (χ_{Co} =0). The measurements were repeated at least three times to verify the results obtained in the present case. As observed in the previous results, the Co-B shows much higher catalytic activity as compared to Ni-B thus indicating that Co metal is more active site than Ni for catalytic hydrolysis reaction. The increment in the activity by increasing the amount in Co is due to the fact that less active Ni sites are replaced by more active Co sites. However, the effect of B enrichment on the surface of the Co-Ni-B (χ_{Co} = 0.90, 0.85 and 0.75) causes the superior activity than Co-B as discussed previously.

3.2.1 Activation Energy

In another set of experiments, the hydrogen generation from catalytic hydrolysis of alkaline $NaBH_4$ (0.025 M) solution was measured at different solution temperature ranging from 298 to 313 K by using Co-Ni-B ($\chi_{Co} = 0.85$) (Fig. 3.5) and Co-B (Fig. 3.6) catalyst powders. As expected, H_2 generation rate increases with the temperature. The Arrhenius plot (inset of Fig. 3.5 and Fig. 3.6) of the hydrogen production rate gives activation energies of about 34 ± 1 and 45 ± 2 $kJmol^{-1}$, within experimental errors, for Co-Ni-B ($\chi_{Co} = 0.85$) and Co-B powder catalyst, respectively. This value for Co-Ni-B powder is lower than that found by Amendola et al. [16] using Ru catalyst ($47\,kJmol^{-1}$), while Kaufman and Sen [45] obtained $75\,kJmol^{-1}$ for Co, $71\,kJmol^{-1}$ for Ni, and $63\,kJmol^{-1}$ for Raney nickel. The activation energy for the Co-B catalyst measured in the present case is same as that obtained by Lee et al. [55] with structured Co-B catalyst powder ($45\,kJmol^{-1}$). The favourable activation energy value obtained with Co-Ni-B, as compared to Co-B, suggests that electronic synergetic effects operate with Co and Ni atoms in Co-Ni-B which help to enhance the catalytic activity. Possibly, transient electronic states are favoured with Co and Ni atoms in the Co-Ni-B powder at appropriate atomic composition.

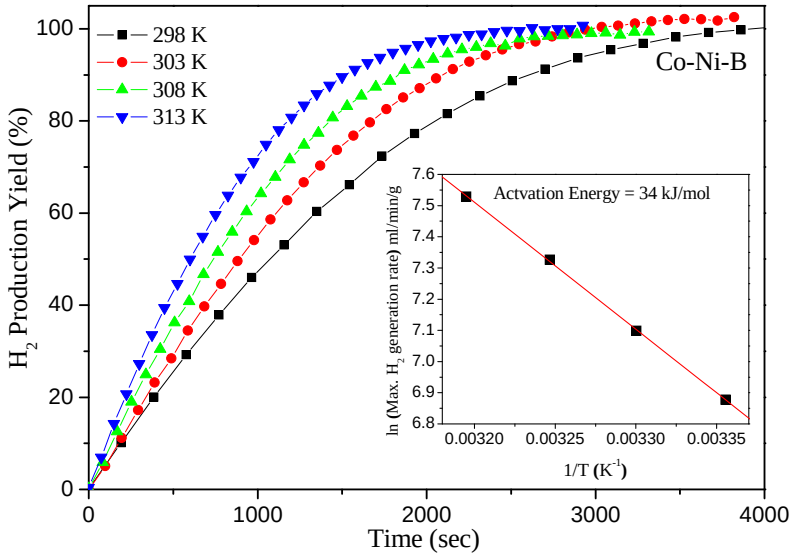

Figure 3.5 – Hydrogen generation yield as a function of reaction time with Co-Ni-B ($\chi_{Co} = 0.85$) catalyst measured at four different temperatures by hydrolysis of alkaline $NaBH_4$ (0.025 M) solution. Inset shows the Arrhenius plot of the H_2 generation rates.

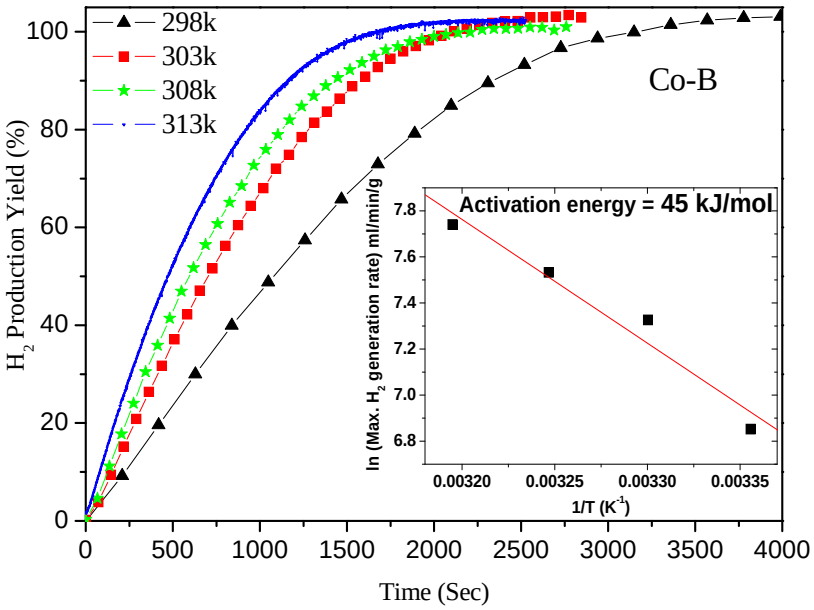

Figure 3.6 – Hydrogen generation yield as a function of reaction time with Co-B catalyst measured at four different temperatures by hydrolysis of alkaline $NaBH_4$ (0.025 M) solution. Inset shows the Arrhenius plot of the H_2 generation rates.

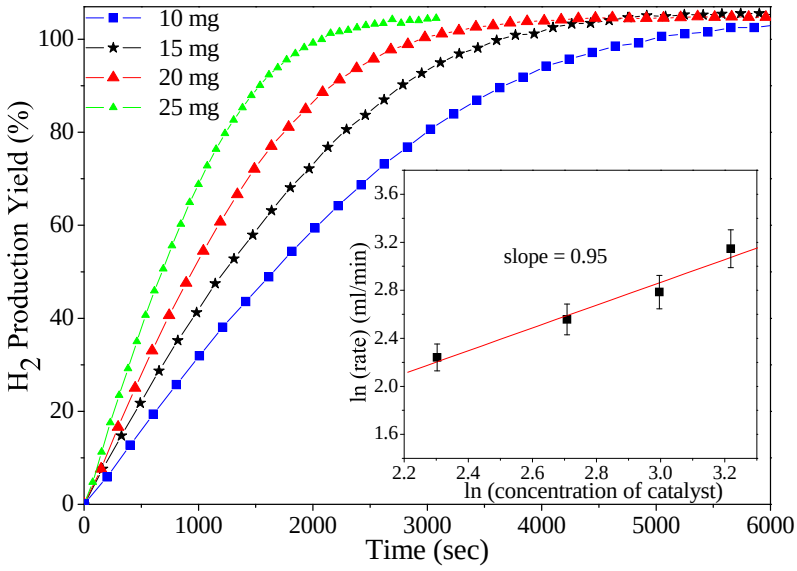

Figure 3.7 – Hydrogen generation yield as a function of reaction time with Co-Ni-B ($\chi_{Co} = 0.85$) catalyst of four different concentrations by hydrolysis of alkaline $NaBH_4$ ($0.025M$) solution. Inset shows the plot of $ln(H_2\, generation\, rate)$ vs. $ln(concentration\, of\, catalyst)$.

3.2.2 Effect of catalyst concentration

To identify the reaction order in connection to the catalyst concentration, the H_2 generation yield was measured by hydrolysis of alkaline $NaBH_4$ (0.025 M) solution using four different amounts of Co-Ni-B ($\chi_{Co} = 0.85$) catalyst, i.e., $10, 15, 20, 25\, mg$ (Fig. 3.7) at 298 K. The figure clearly indicates that the hydrolysis of $NaBH_4$ depends on the catalyst concentration because when the amount of catalyst increases, then the reaction takes much less time to reach the maximum expected H_2 generation yield. The hydrogen generation rate (R) seems to be proportional to the catalyst concentration when the concentrations of all the other reactants are kept constant:

$$R \propto [concentration\, of\, catalyst]^x \tag{3.1}$$

By plotting $ln(R)$ vs. $ln(concentration\, of\, catalyst)$ one obtains the straight line of the inset of Fig. 3.7 and the slope provides the value of the reaction order (x) with respect to the concentration of catalyst. The value of the slope is 0.95 thus indicating that the hydrolysis of $NaBH_4$ is first order reaction with respect to the concentration of Co-Ni-B ($\chi_{Co} = 0.85$) powder catalyst.

3.2.3 Effect of heat-treatment

To study the effect of structural modification on catalytic activity, Co-Ni-B ($\chi_{Co} = 0.85$) and Co-B were heat-treated in Ar atmosphere at 773 K for $2h$. XRD pattern (Fig. 3.8) of the annealed Co-Ni-B ($\chi_{Co} = 0.85$) powder show that annealing causes structural modification in the powder leading to the formation of crystalline Co metal phase with the crystal size of around 15 nm. Morphological studies performed by SEM also show analogous results for annealed Co-Ni-B powder catalyst.

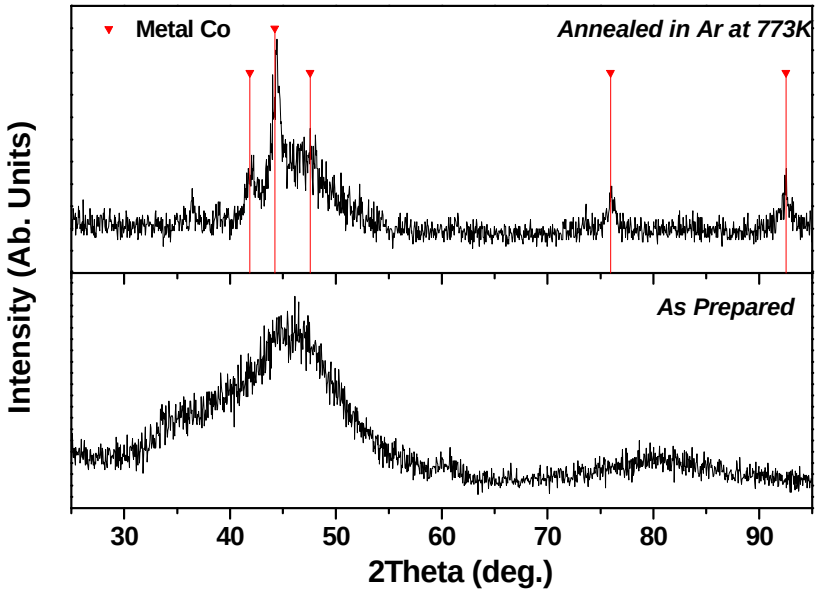

Figure 3.8 – XRD pattern of Co-Ni-B ($\chi_{Co} = 0.85$) catalyst powder untreated and treated in Ar gas atmosphere at 773 K for $2h$.

The SEM images (Fig. 3.9) clearly demonstrate the transformation from the well-dispersed spherical particle morphology of the fresh powders (Fig. 3.9 A) to porous crystallite morphology after annealing at 773 K (Fig. 3.9 B). The hydrogen generation yield, as function of time, obtained by hydrolysis of alkaline $NaBH_4$ (0.025 M) solution using annealed Co-Ni-B ($\chi_{Co} = 0.85$) at 293 K, is reported in Fig. 3.10. However, the structural changes did not bring any differences in the catalytic activity for the annealed Co-Ni-B ($\chi_{Co} = 0.85$) powder when compared with untreated powder. Co-B powder annealed at 773 K in similar condition, shows analogous structural modification similar to that of Co-Ni-B.

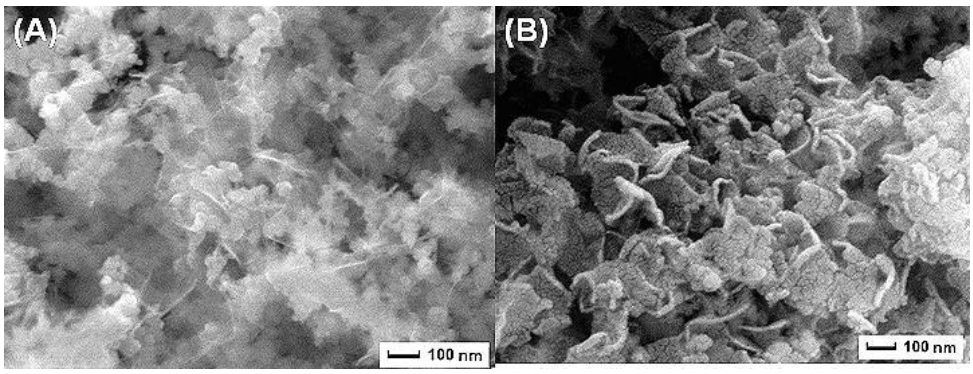

Figure 3.9 – SEM micrographs of Co-Ni-B ($\chi_{Co} = 0.85$) catalyst powder (A) untreated and (B) treated in Ar gas atmosphere at 773 M for $2h$.

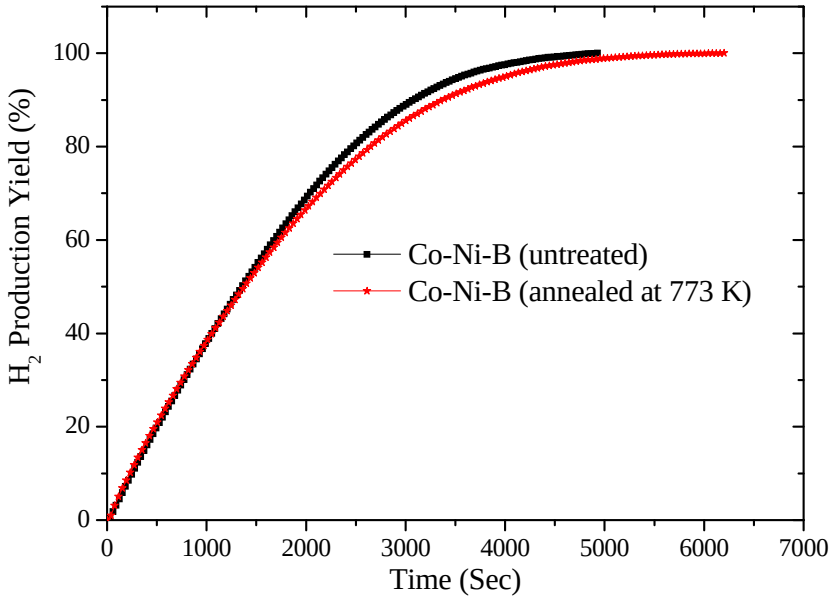

Figure 3.10 – Hydrogen generation yield as a function of reaction time with Co-Ni-B ($\chi_{Co} = 0.85$) catalyst powder untreated and heat-treated at 773 K obtained by hydrolysis of alkaline $NaBH_4$ (0.025 M) solution.

However, there is now a decrease in the hydrogen generation rate as compared to the untreated powder (Fig. 3.11). Lee et al. [55] and Wu et al. [90] also reported a decrement in the H_2 generation rate for Co-B powder when annealed above 573 K and the authors discussed the results in terms of the crystallization of Co metal. However, our present results indicate that even after crystallization of the Co metal phase in Co-Ni-B powder, the same powder maintains its catalytic efficiency. Thus it shows that the Co-Ni-B catalyst is stable and useful for high temperature application

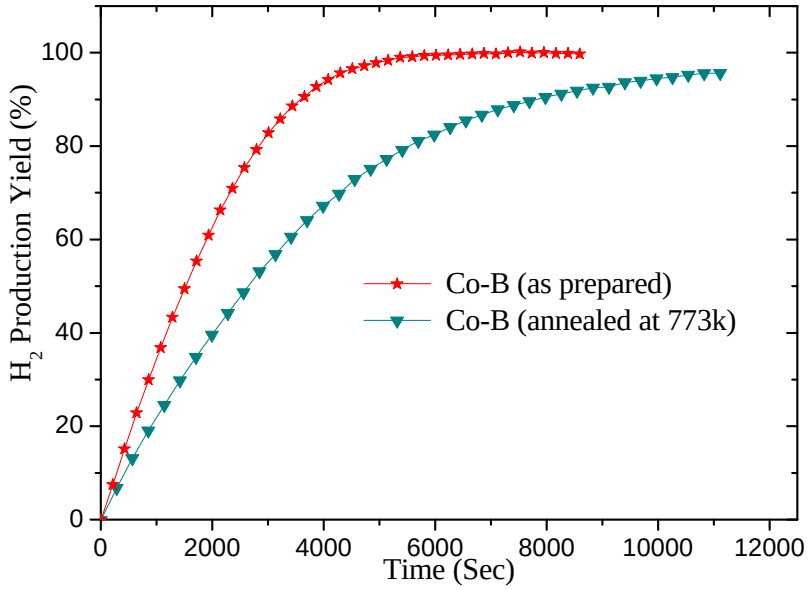

Figure 3.11 – Hydrogen generation yield as a function of reaction time with Co-B catalyst powder untreated and heat-treated at 773 K obtained by hydrolysis of alkaline $NaBH_4$ (0.025 M) solution

3.3 P-doped Co-B catalyst

Effect of different $^{Co}/_{P}$ molar ratios

Co-P-B powder catalyst was synthesized by chemical reduction of cobalt salt ($CoCl_2$) and sodium hypophosphite (NaH_2PO_2) in aqueous solution (see 2.1.1). In order to have the complete reduction of cobalt salt, the molar ratio of $\frac{(P+B)}{Co}$ was kept at about 4. The Co-P powder was prepared as reported elsewhere [83] by heating the aqueous solution of $CoCl_2$ and NaH_2PO_2 at 343 K under vigorous stirring. The pH value (equal to 11) was controlled by using NaOH solution.

Catalyst activity measurement Fig. 3.12 presents the hydrogen generation yield as a function of time obtained from the hydrolysis of alkaline $NaBH_4$ (0.025 M) solution with Co-P, Co-B, and Co-P-B catalyst powders at 298 K. The B/P molar ratio of 2.5 was used in Co-P-B catalyst. The expected total amount of H_2 was measured for all the catalysts used. The Co-P-B catalyst shows much higher catalytic activity as compared to the same amount ($15\,mg$) of Co-B and Co-P powder. The maximum values of hydrogen generation rate (R_{max}): these values are summarized in Table 3.3. The Co-P catalyst powder yields negligible R_{max} as compared to that by Co-B and

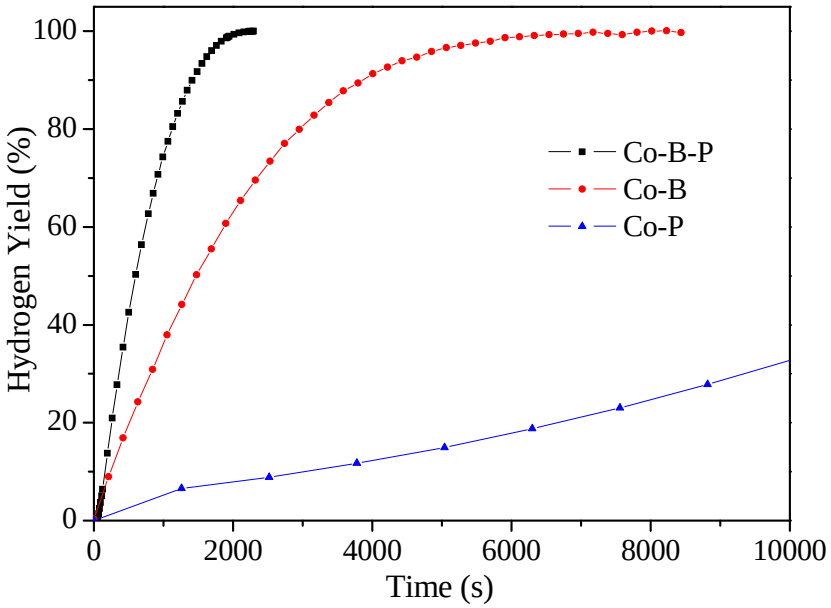

Figure 3.12 – Hydrogen generation yield as a function of reaction time obtained by hydrolysis of alkaline $NaBH_4$ (0.025 M) solution with Co-B, Co-P, and Co-P-B (B/P molar ratio = 2.5) catalyst powders. Inset shows the extended plot of hydrogen generation yield as function of time for Co-P catalyst

Co-P-B catalyst powders. On the contrary, the Co-P-B catalyst yields the highest R_{max} which is about 2.5 times higher than that obtained for Co-B catalyst.

Catalyst powder ($15\,mg$)	Maximum H_2 generation rate, R_{max} ($ml\,min^{-1}g^{-1}$ catalyst)
Co-B	850
Co-P	100
Co-P-B	2120

Table 3.3 – Maximum hydrogen generation rate obtained fromthe hydrolysis of alkaline $NaBH_4$ (0.025 M) solution by the catalyst powders

Fig. 3.13 presents the SEM images of Co-B, Co-P, and Co-P-B (molar ratio B/P = 2.5) powders. The SEM images of Co-B and Co-P-B powders show particle like morphology with average particle size in the range between $30-40\,nm$. In the cases of Co-B and Co-P-B catalyst preparations, an efficient reducing agent in the form of $NaBH_4$ was used which is able to cause the rapid reduction of Co ions and thus does not permit the particles to grow above a few nanometers. This kind of morphology

is helpful to enhance the active surface area of catalyst. On the contrary, crystallite structure (Fig. 3.13 b) with bigger irregular particles is clearly visible in the case of Co-P catalyst. The reduction of Co ions proceeds gradually in presence of NaH_2PO_2 due to its lower strength as a reducing agent, as compared to that of $NaBH_4$, allowing the growth of large particles in Co-P catalyst. Thus, small surface area achieved in Co-P catalyst might be one of the reasons for the low efficiency of Co-P powder for H_2 generation.

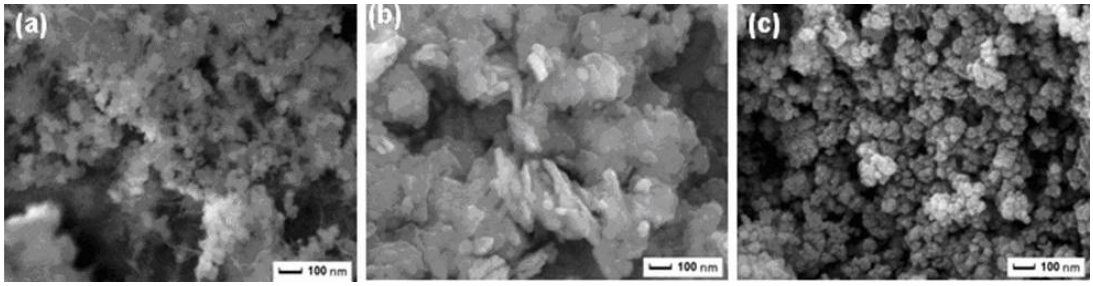

Figure 3.13 – SEM micrographs of (a) Co-B, (b) Co-P, and (c) Co-P-B (B/P molar ratio= 2.5) catalyst powders

XRD patterns (Fig. 3.17)[3] of Co-B, Co-P, and Co-P-B (with molar ratio B/P= 2.5) powders show a single broad peak at around $2\theta = 45^{o}$ attributed to the amorphous state of cobalt–metalloid alloy [91]. This indicates that all the catalyst powders produced by chemical reduction method are amorphous. It may be inferred that a short-range ordered and long-range disordered structure might be helpful for the catalytic activity [92]. To understand the enhanced efficiency of Co-P-B (with molar ratio B/P = 2.5) catalyst and low efficiency of Co-P catalyst, it is necessary to gain insight into the surface electronic interaction between the elemental atoms in the compound. Thus, XPS spectra of Co-B, Co-P, and Co-P-B (with molar ratio B/P = 2.5) catalyst powders were acquired and are shown in Fig. 3.14.

3.3.1 XPS Analysis

For Co-B and Co-P-B catalyst powders, two peaks appear corresponding to the $Co_{2p_{3/2}}$ level at the binding energies of 778.4 and 781.6 eV, indicating that Co metal exists in both elemental and oxidized states respectively. On the contrary, only one peak appears corresponding to the $Co_{2p_{3/2}}$ level for Co-P catalyst, at the binding energy of 781.6 eV, signifying that the element cobalt is present in completely oxidized

[3] Figure not shown for Co-P

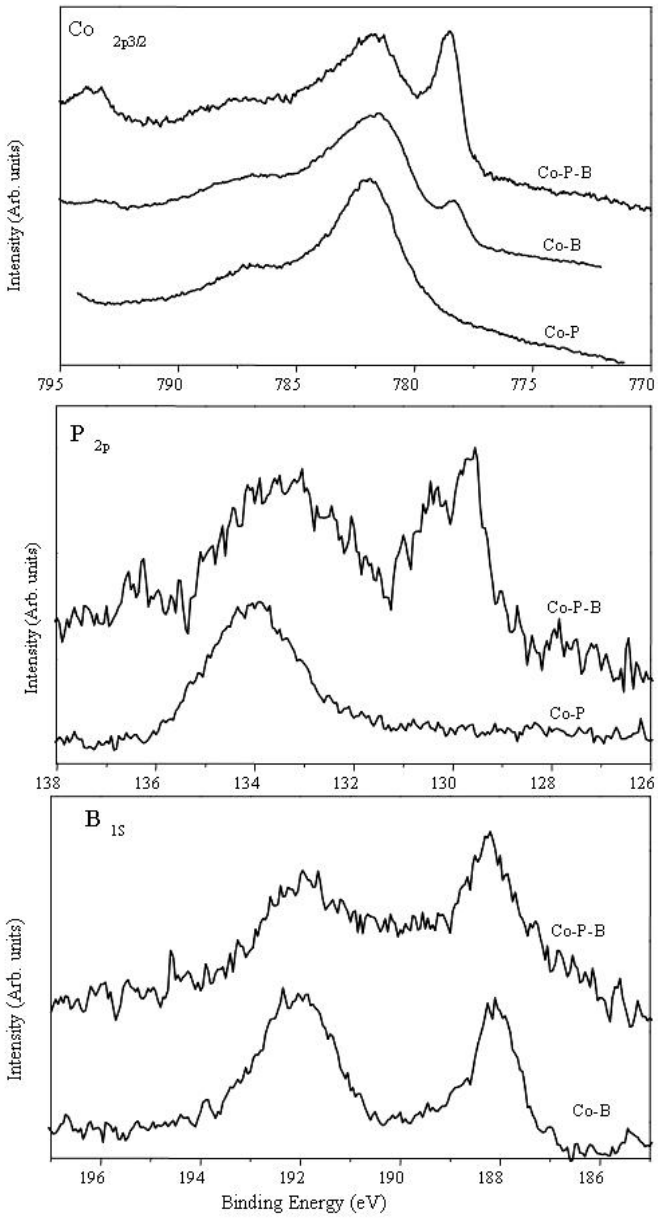

Figure 3.14 – X-ray photoelectron spectra of $Co_{2p_{3/2}}$, P_{2p}, and B_{1s} level for Co-B, Co-P, and Co-P-B (B/P molar ratio = 2.5) catalyst powders

state. The peak due to oxidized cobalt is mainly present in form of +2 state attributed to $Co(OH)_2$, which would have been formed during the catalyst preparation reaction between the reducing agent and the metal salt in aqueous medium [84, 85]. The amount of $Co(OH)_2$ is minimum in Co-P-B catalyst as compared to Co-B and Co-P. Two XPS peaks with binding energy (BE) of 188.2 and 192.1 eV are also observed corresponding to the B_{1s} level in Co-B and Co-P-B, which are assigned to elemental and oxidized boron respectively [84, 85]. By comparing the BE of pure boron (187.1eV) [86] with that of boron in the catalyst, one observe a positive shift of 1.1 eV. This shift indicates an electron transfer from alloying B to vacant $d-$orbital of metallic Co which makes the boron atom electron deficient and the cobalt atom enriched with electrons in the catalyst powders. In the X-ray photoelectron spectra corresponding to the P_{2p} level, one observes signature of two kinds of phosphorous species in Co-P-B catalyst producing peaks with binding energy of 130 eV and 133.3 eV. The lower BE is attributed to the metallic phosphorous while the higher BE is assigned to the oxidized phosphorous. No significant shift in BE of metallic phosphorous was observed with respect to the elemental one, indicating that the electron transfer between Co and P in Co-P-B could be neglected. However in Co-P catalyst powder only BE peak due to oxidized phosphorous is seen. The above XPS results are now considered to understand the differences observed in catalytic activity with different catalyst powders. In the case of Co-B and Co-P-B catalyst, boron interacts with cobalt by transferring electron from alloying B to vacant d orbital of metallic Co which makes boron electron-deficient and Co electron-enriched. Looking at the mechanism proposed for metal catalyzed hydrolysis of $NaBH_4$, electron-enriched metal active sites will be able to facilitate the catalysis reaction by providing the electron required by the hydrogen atom to leave the metal site in hydridic form (H^-) which then could react with the water molecule to produce H_2 and OH^- ion. This means that the higher electron density on active metal site is an important aspect for the enhancement of the catalytic activity of catalyst powder for hydrolysis of $NaBH_4$, as in the present case of Co-B and Co-P-B catalysts. To this purpose, note that the XPS result clearly shows that there is no electronic interaction between Co and P atoms in Co-P catalyst. The XPS analysis of Co-P powder prepared in a similar manner, as reported by H. Li et al. [82], showed no electronic transfer between Co and P. However, in the literature, many contradictory results are reported for the Ni-P powder: observation of some authors [93, 94] are similar to our Co-P powder while others [83, 95] showed that there is an electron transfer from Ni to P atoms making the former element electron deficient. Electron transfer also plays an important role in the oxide formation on

the surface of the active metal sites. In Co-B and Co-P-B catalysts, electron enriched metal active sites repel the adsorption of oxygen atoms from the ambient atmosphere, while they are strongly adsorbed by the electron-deficient B. In other words, alloying B effectively protects metals from oxidation in ambient condition [87, 88]. Due to the lack of electronic interaction between metal and metalloid in Co-P catalyst, P is unable to protect Co from oxidation. This is clearly evidenced by the fact that Co on the surface is in form of completely oxidized state in our Co-P catalyst powder as observed in the XPS spectra. Hence it seems that the lack of electronic interaction between Co and P atoms might be the main reason for the less active nature of Co-P as catalyst in hydrolysis of $NaBH_4$ as compared to Co-B and Co-P-B catalysts. The surface atomic composition, calculated from XPS spectra, shows that the amount of the surface Co sites is maximum for Co-P (∼77 at.%) and minimum for Co-B (∼60 at.%) catalyst. This shows that phosphorus plays some role to favour the enrichment of the catalyst surface with Co sites. In the case of the Co-P-B catalyst, the concentration of the surface Co sites is between that of Co-P and Co-B, being about $69\,at.\%$. This result reveals that the role of P in the Co-P-B catalyst is to favour the enrichment of the surface with Co active sites. Li et al. [82] also observed higher Co concentration on the surface of Co-P and Co-P-B as compared to Co-B catalyst. Lee et al. [83] reported the same results using Ni-based amorphous alloy (Ni-P-B, Ni-P, and Ni-B). On the basis of the above results, we may conclude that the higher catalytic activity of the Co-P-B powder, as compared to Co-B and Co-P, may be attributed to the synergistic effects occurring from the alloying P and B in which the former element is able to create high number of Co active sites on the surface, while the later element provides the necessary electron density to Co active sites for the catalytic activity.

Role of metalloids (P and B)

After these preliminary studies, Co-P-B amorphous alloys were synthesized with different B/P molar ratio in order to further investigate the effect of B and P concentration on catalytic activity. The hydrogen generation yield was measured as a function of time (Fig. 3.15) by hydrolysis of alkaline $NaBH_4$ (0.025 M) solution using different B/P molar ratio in Co-P-B catalyst powders. The inset of Fig. 3.15 shows the value of R_{max} obtained with Co-P-B catalyst having different B/P molar ratio. It is clearly evident that Co-P-B powder shows higher R_{max} than the Co-B independent of B/P molar ratio used: this further proves that the inclusion of P creates more Co active sites on the surface while B provides them with the required electron density.

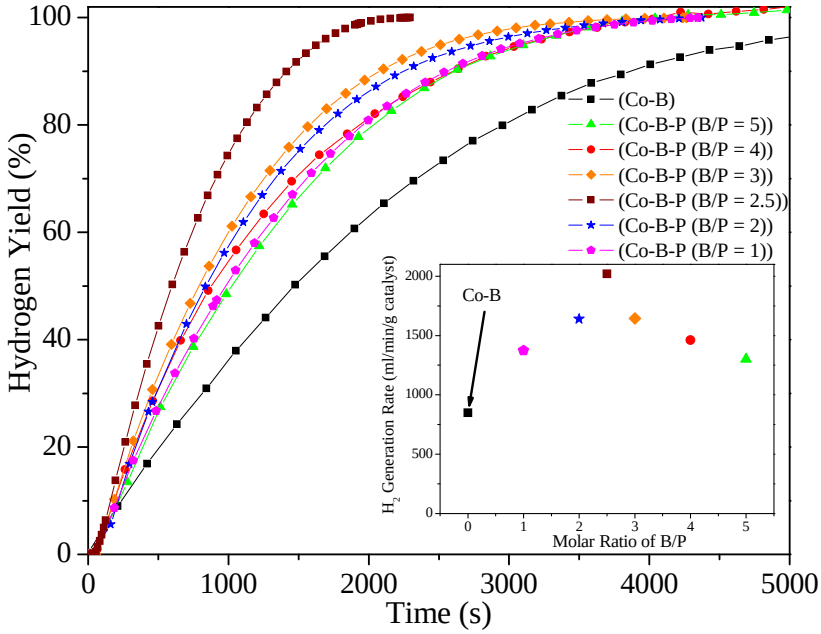

Figure 3.15 – Hydrogen generation yield as a function of reaction time obtained by hydrolysis of alkaline $NaBH_4$ (0.025 M) solution with Co-B and Co-P-B catalysts with different B/P molar ratio ranging from 1 to 5. Inset shows the maximum H_2 generation rate (R_{max}) obtained with Co-P-B catalyst as a function of B/P molar ratio.

Initially R_{max} increases with the B/P ratio, to reach the maximum when B/P molar ratio is equivalent to 2.5, and then decreases further. At high B/P molar ratio the concentration of P is unable to provide enough active Co sites on the surface, while at low B/P molar ratio the concentration of B is insufficient to fulfill the requirement of electron density to all the excess Co active site on the surface. The above considerations help to explain the trend of the results in the inset of Fig. 3.15, although the maximum H_2 generation rate obtained at the B/P molar ratio of 2.5 is not clearly understood. Basic calculations of atomic site occupation as well as of electron transfer are necessary to further understand the mechanism.

3.4 Co-Ni-P-B powder catalyst.

Earlier in the chapter, we have seen that by adding phosphorous to Co-B, we are able to increase the catalytic activity of about 2 times with respect to that of Co-B catalyst. Such an enhancement was attributed to synergic effects of B and P in the interaction with Co, favouring electron transfer. We also proved that mixing Ni with Co-B in a proper proportion leads to an enhancement in catalytic ability of the Co-B catalyst, where Ni is able to provide additional electrons to the Co metal which favours

the catalytic reaction. Because of these considerations, it is interesting to investigate the performance of a single mixed catalyst (Co-Ni-P-B), possibly including a variety of synergic effects in electron transfer to Co.

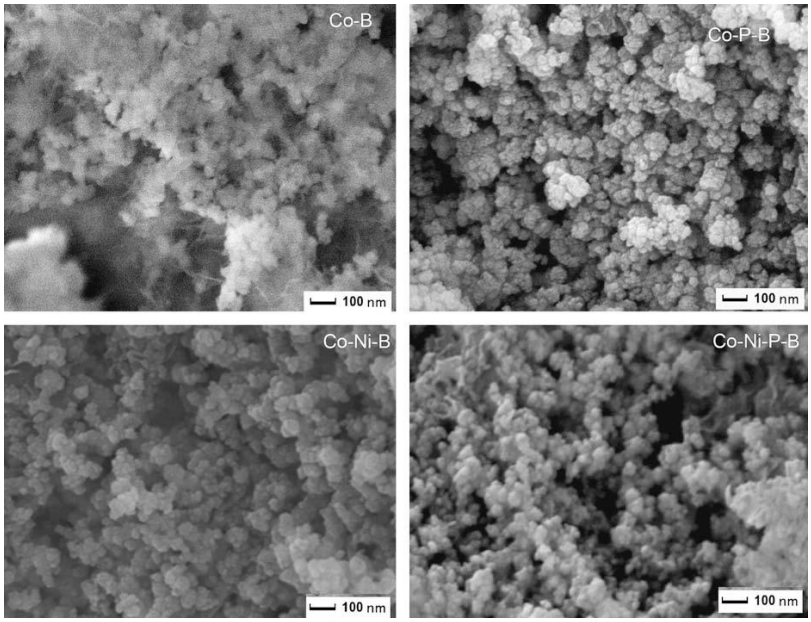

Figure 3.16 – SEM micrographs of Co-B, Co-P-B, Co-Ni-B, and Co-Ni-P-B (molar ratio B/P = 2.5 and $\frac{Co}{Co+Ni} = 0.85$) catalyst powders

The present work reports on the synthesis and characterization of mixed Co-Ni-P-B catalyst powder for hydrogen generation by hydrolysis of $NaBH_4$ solution. The molar ratio of B/P and Co/Ni was varied in order to understand the role of composition in the Co-Ni-P-B catalytic activity which indeed, for appropriate composition, results greater than that of Co-B, Co-Ni-B, and Co-P-B powders.

In Fig. 3.16 we present SEM images of Co-B, Co-P-B, Co-Ni-B, and Co-Ni-P-B (molar ratio B/P = 2.5 and $\frac{Co}{Co+Ni} = 0.85$) powders. The SEM images of all the catalyst powders show particle like morphology with average particle size in the range between 30 and $40nm$. During catalyst preparation, an efficient reducing agent in form of $NaBH_4$ was utilized which is able to cause the rapid reduction of Co ions and thus it does not permit particle growth above a few nanometers. However, this kind of morphology is helpful in enhancing the active surface area of catalysts.

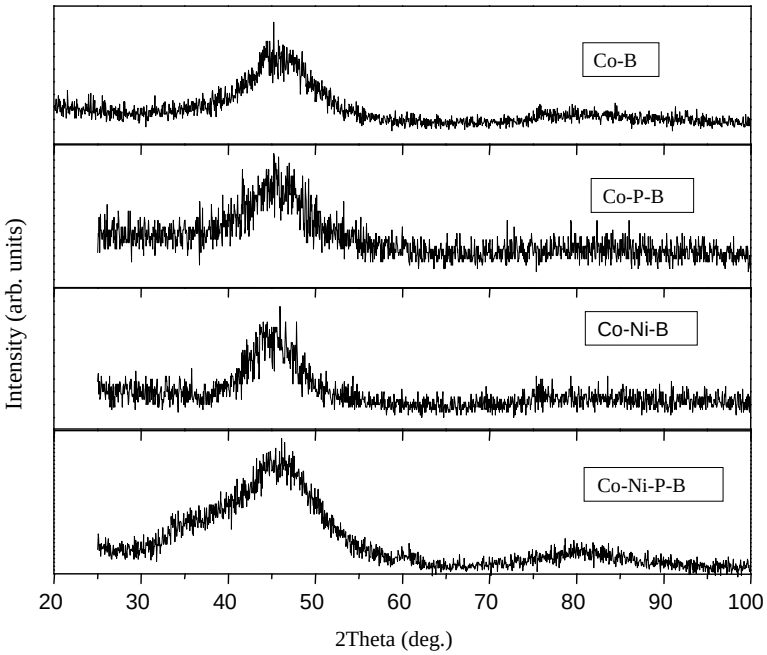

Figure 3.17 – XRD pattern of Co-B, Co-P-B, Co-Ni-B, and Co–Ni-P– B (molar ratio of B/P= 2.5 and of $\frac{Co}{Co+Ni} = 0.85$) catalyst powders.

XRD patterns (Fig. 3.17) of Co-B, Co-P-B, Co-Ni-B, and Co-Ni-P-B (molar ratio B/P = 2.5 and $\frac{Co}{Co+Ni}$ = 0.85) catalyst powders show a single broad peak at around $2\theta = 45^{o}$ thus indicating that all the catalyst powders, produced by chemical reduction method, are almost amorphous. Here it may be inferred that a short-range ordered and long-range disordered structure might be helpful for the catalytic activity [92].

Catalyst activity measurement

The catalyst powders efficiency was determined by measuring the hydrogen generation yield as function of time by hydrolysis of alkaline $NaBH_4$ (0.025 M) solution with Co-B, Co-P-B, Co-Ni-B, and Co-Ni-P-B catalyst powders at 298 K and presented in Fig. 3.18 The B/P and $\frac{Co}{Co+Ni}$ molar ratio was kept at 2.5 and 0.85, respectively, in Co-Ni-P-B catalyst. The hydrogen production starts immediately without any induction time and reaches the 100% of the theoretical H_2 yield, irrespective of the type of catalyst used. The H_2 generation rate decreases with time (as it can be easily seen) because, during reaction, the $NaBH_4$ concentration decreases in the solution by hydrogen evolution : this suggests the non-zero order of the reaction kinetics.

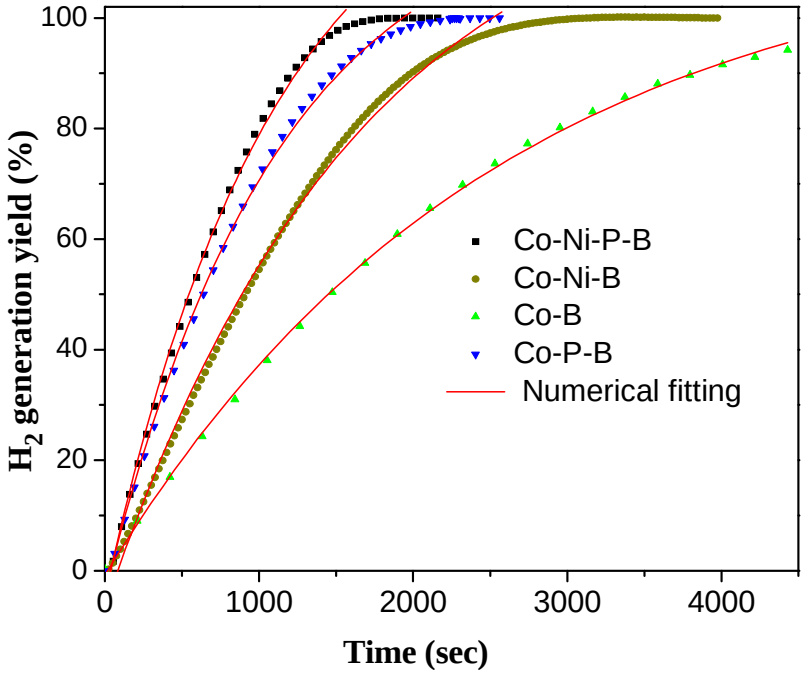

Figure 3.18 – Hydrogen generation yield as a function of reaction time obtained by hydrolysis of alkaline $NaBH_4$ (0.025 M) solution with Co-B, Co-P-B, Co-Ni-B, and Co-Ni-P-B (molar ratio of B/P= 2.5 and $\frac{Co}{Co+Ni} = 0.85$ catalyst powders at 298 K.

This can be further understood by considering the two simple steps involved in the catalytic hydrolysis reaction of $NaBH_4$ on the surface of metal catalyst [49, 96]: 1) absorption of BH_4 on the surface active sites of the catalyst, and 2) reaction of this absorbed species to generate H_2. Thus as the concentration of $NaBH_4$ decreases the hydride/catalyst molar ratio decreases in the solution which means that the catalyst surface is not completely covered with BH_4 reactants and there are some unsaturated active sites on the surface available for the reaction. In this case the first order kinetics involving diffusion of BH_4 on the catalyst surface is the rate limiting step. In addition, hydrogen evolution data has been well fitted by using the exponential function (Fig. 3.18). Hence it shows that by using low hydride/catalyst ratio, as in the present case, the hydrolysis reaction proceeds with first order kinetics. The Co-Ni-P-B catalyst shows highest catalytic activity as compared to the same amount ($15\,mg$) of Co-B, Co-Ni-B, and Co-P-B catalyst powders. Fitting numerical procedure, as used in our previous work [97], has been applied to obtain maximum hydrogen generation rates (R_{max}), for catalyst powders, which are summarized in Table 3.4.

The Co-Ni-P-B catalyst shows R_{max} which is about 2.8 times higher than that obtained for Co-B catalyst. The R_{max} value acquired with the several catalyst powders

Catalyst powder	Maximum H_2 generation rate R_{max} ($ml/min/g$ catalyst)
Co-B	680
Co-Ni-B	1170
Co-P-B	2000
Co-Ni-P-B	2400

Table 3.4 – Maximum hydrogen generation rate obtained from the hydrolysis of alkaline $NaBH_4$ (0.025 M) solution by the catalyst powders.

decreases in following order: Co-Ni-P-B > Co-P-B > Co-Ni-B> Co-B. The measurements are repeated at least 3 times to verify the results obtained in the present case. All the catalyst powders exhibit similar morphology (Fig. 3.16) and structural properties (Fig. 3.17), hence the above obtained trends in hydrogen generation rate should be explained in terms of elemental interaction in the catalyst powders. Earlier in the chapter, we have analyzed Co-Ni-B catalyst powder proving that the presence of mixed Co-Ni, with B atoms in a proper amount, results in an enhanced catalytic activity for hydrogen production by hydrolysis of $NaBH_4$ with respect to Co-B or Ni-B powders. The specific role of the atomic elements in the catalyst powders was established by X-ray Photoelectron Spectroscopy (XPS) [97–99]. The role of B in the catalyst compound is to protect metal active sites from oxidation and to assist catalysis reaction, by transferring electrons to unfilled *d*-orbital of the Co metallic element. XPS analysis of catalyst powders also revealed that Co in Co-Ni-B powder possesses a greater electron density as compared to Co in Co-B catalyst. This electron enriched metal active site is able to facilitate the catalysis reaction by providing the electron required by the hydrogen atom to be released in hydridic form (H) from the catalyst surface [42]. Thus the role of nickel in the Co-Ni-B catalyst powder is to provide electrons to Co active sites in addition to that provided by B. This explains the higher activity of Co-Ni-B catalyst as compared to that of the Co-B catalyst. In addition, we found that ternary alloy catalyst in form of Co-P-B was able to produce hydrogen with much higher rate as compared to the binary alloy Co-P and Co-B catalyst powders by hydrolysis of $NaBH_4$ [99]. Synergic effects caused by P and B atoms in the Co-P-B catalyst are the reason found behind this enhancement. In Co-P-B catalyst, as revealed by XPS analysis, the role of phosphorous is to create high number of Co active sites on the surface, while the boron provides the necessary electron density to

Co active sites for the catalytic activity [99]. The highest H_2 generation rate achieved by Co-Ni-P-B catalyst powder can be understood by considering the fact that the role of phosphorous is to enrich the catalyst surface with active cobalt sites while boron and nickel provide electrons to the active Co sites. The highest catalytic performance achieved by Co-Ni-P-B catalyst powder may be attributed to the combined synergic effects similar to that obtained with Co-Ni-B and Co-P-B catalysts

3.4.1 Role of metalloids (P and B)

In order to further investigate the effect of B and P concentration on catalytic activity, the Co-Ni-P-B amorphous alloys were synthesized with different B/P molar ratio by keeping $\frac{Co}{Co+Ni}$ molar ratio constant at 0.85. The hydrogen generation yield was measured as a function of time (Fig. 3.19) by hydrolysis of alkaline $NaBH_4$ (0.025 M) solution using different B/P molar ratio in Co-Ni-P-B catalyst powder. The inset of Fig. 3.19 shows the plot of R_{max} as function of B/P molar ratio in Co-Ni-P-B catalyst. It is clearly evident that Co-Ni-P-B powder shows higher R_{max} than the Co-Ni-B, independent of the used B/P molar ratio: this further proves that the inclusion of P creates more Co active sites on the surface while B and Ni provide the catalytic sites with an increased electron density. Initially R_{max} increases with the B/P ratio, then it reaches the maximum value when B/P molar ratio is equivalent to 2.5, and then it decreases. At high B/P molar ratio the concentration of P is unable to provide enough number of active Co sites on the surface, while at low B/P molar ratio the concentration of B is insufficient to fulfill the requirement of electron density to all the excess Co active sites on the surface. At B/P molar ratio of 2.5, there might be enough amount of boron to provide the electron density to all the active Co sites created by phosphorous thus inducing the highest H_2 generation rate. The above qualitative considerations help to explain the trend of the results in the inset of Fig. 3.19. Basic calculations of atomic sites occupation as well as of electrons transfer are necessary to quantitatively understand the mechanisms leading to the enhanced catalytic activity, but this investigation is outside the scope of the present study. Here we would like to only remark that the Co-Ni-P-B catalyst powders, for any B/P molar ratio, exhibit similar particle like morphology with average size of $30 - 40\,nm$ (figure not shown). The above trend of H_2 generation rate as function of B/P molar ratio in Co-Ni-P-B catalyst is analogous to that achieved with the Co-P-B catalyst powder, as investigated in our previous studies, exhibiting the highest R_{max} when the B/P molar ratio is equivalent to 2.5.

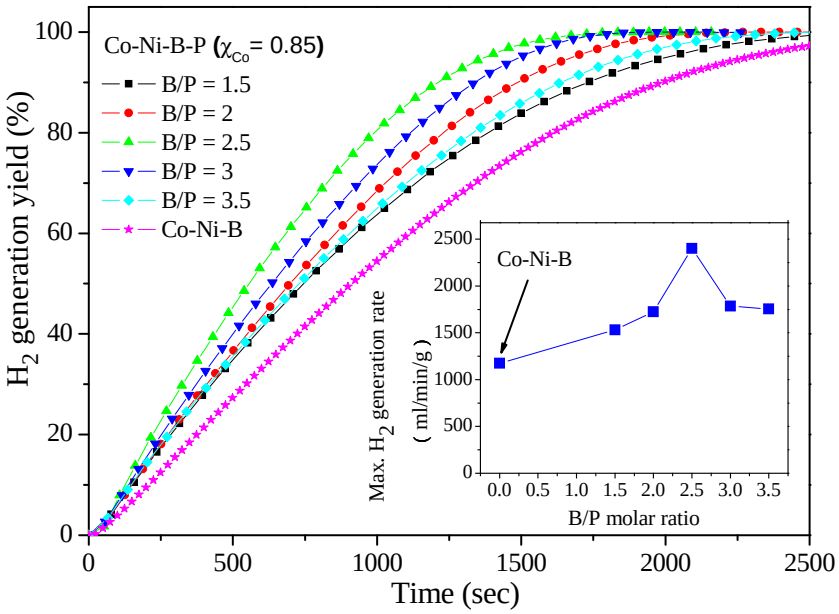

Figure 3.19 – Hydrogen generation yield as a function of reaction time obtained, at 298 K, by hydrolysis of alkaline $NaBH_4$ (0.025 M) solution with Co-Ni-B and Co-Ni-P-B (molar ratio of $\frac{Co}{Co+Ni} = 0.85$ catalysts with different B/P molar ratio ranging from 1.5 to 3.5. Inset shows the maximum H_2 generation rate (R_{max}) obtained with Co-Ni-P-B catalyst as a function of B/P molar ratio.

3.4.2 Effect of Co/Ni molar ratio

$\frac{Co}{Co+Ni}$ molar ratio (χ_{Co}) was varied from 0.75 to 0.9 in the Co-Ni-P-B powder catalyst in order to study the effect of active metal concentration on catalytic activity while keeping the B/P molar ratio constant at 2.5. Fig. 3.20 presents the hydrogen generation yield as function of time measured by hydrolysis of alkaline $NaBH_4$ ($0.025M$) solution using Co-Ni-P-B catalyst powder with different molar ratio of Ni and Co. The inset of Fig. 3.20 shows the plot of R_{max} as function of χ_{Co}. By increasing the Co content with respect to Ni in the Co-Ni-P-B powder, the hydrogen generation rate increases and it reaches the highest R_{max} of about $\sim$2400 $ml/min/g$ with $\chi_{Co} = 0.85$. With further increase of the molar ratio χ_{Co} to 0.9, the activity of the powder decreases. As observed in the earlier, the Co-B catalyst shows much higher catalytic activity as compared to Ni-B thus indicating that Co metal is a more active site than Ni for catalytic hydrolysis reaction. The increment in the activity by increasing the amount of Co is due to the fact that less active Ni sites are replaced by more active Co sites. However, when χ_{Co} exceeds 0.85 the atomic surface composition and possibly atomic arrangement do not favour the appropriate electrons transfer to enhance the catalytic activity. Here also, basic calculations are necessary to clarify

the experimental results. Similar trend in H_2 generation rate with respect to $\frac{Co}{Co+Ni}$ molar ratio was observed with Co-Ni-B catalyst powders earlier.

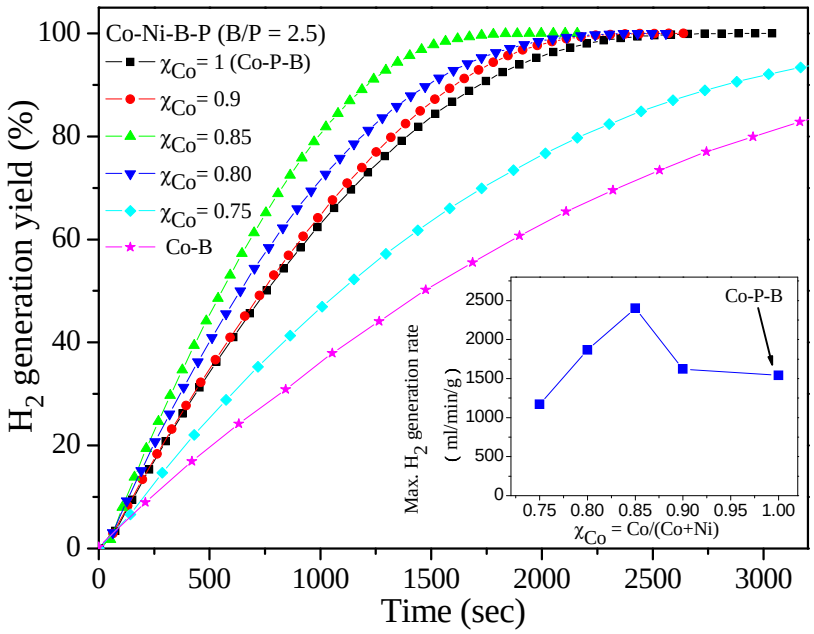

Figure 3.20 – Hydrogen generation yield as a function of reaction time obtained, at 298 K, by hydrolysis of alkaline $NaBH_4$ (0.025 M) solution with Co-B, Co-P-B and Co-Ni-P-B (molar ratio of B/P = 2.5 and with different $\frac{Co}{Co+Ni}$ molar ratio ranging from 0.75 to 1.00. Inset shows the maximum H_2 generation rate (R_{max}) obtained with Co-Ni-P-B catalyst as a function of $\frac{Co}{Co+Ni}$ molar ratio.

3.4.3 Effect of solution temperature

Fig. 3.21 presents the H_2 generation yield as a function of time at different solution temperatures using alkaline $NaBH_4$ (0.025 M) solution and 15 mg of Co-Ni-P-B catalyst (molar ratio of B/P = 2.5 and of $\frac{Co}{Co+Ni} = 0.85$) powder. As expected, the H_2 generation rate increases with the temperature. The Arrhenius plot of the hydrogen production rate (inset of Fig. 3.21) gives activation energy of the catalytic hydrolysis process of about $29 \pm 1\, kJmol^{-1}$, within the experimental errors. The trend in H_2 generation rate obtained with Co-Ni-P-B, Co-P-B, Co-Ni-B, and Co-B catalyst powders by hydrolysis of $NaBH_4$ is also related to their activation energy value. The Co-Ni-P-B catalyst (molar ratio of B/P = 2.5 and of $\frac{Co}{Co+Ni} = 0.85$) powder shows the lowest activation energy ($29 \pm 1\ kJmol^{-1}$) with respect to Co-P-B ($32 \pm 1\ kJmol^{-1}$) , Co-Ni-B ($34 \pm 1\ kJmol^{-1}$), and Co-B ($45 \pm kJmol^{-1}$) catalyst powders. This value is also lower than the activation energy found by Amendola ($47\, kJmol^{-1}$) [16] by using

Ru catalyst. Kaufman and Sen [45], by using different bulk metal catalysts, obtained $75\,kJmol^{-1}$ for cobalt, $71\,kJmol^{-1}$ for nickel, and $63\,kJmol^{-1}$ for Raney nickel. The favourable activation energy value obtained in the present work is an evidence of the synergetic effects of Ni, P, and B in Co-Ni-P-B to enhance the catalytic reaction.

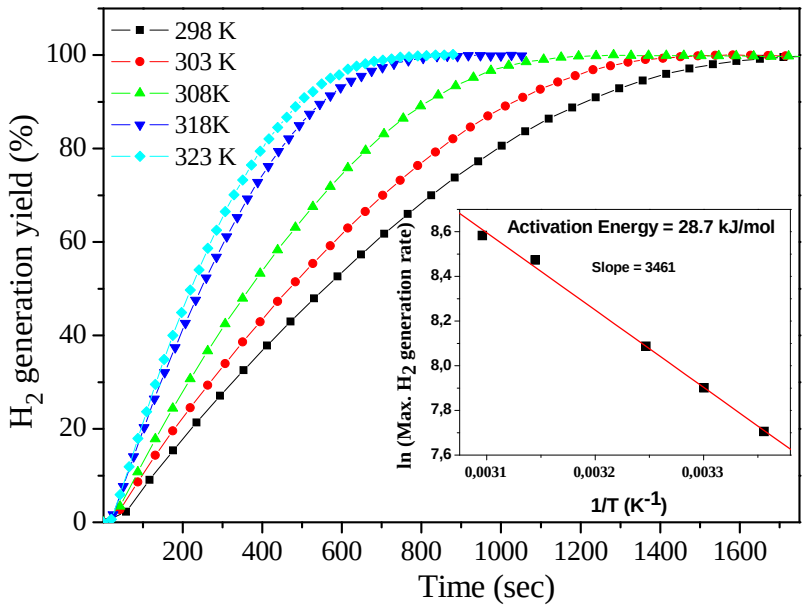

Figure 3.21 – Hydrogen generation yield as a function of reaction time with Co-Ni-P-B (molar ratio of B/P= 2.5 and of $\frac{Co}{Co+Ni} = 0.85$) catalyst measured at 5 different solution temperatures by hydrolysis of alkaline $NaBH_4$ (0.025 M) solution. Inset shows the Arrhenius plot of the H_2 generation rates.

3.4.4 Effect of heat-treatment

To study the effect of structural modification on catalytic activity, Co-Ni-P-B powder (molar ratio of B/P = 2.5 and of $\frac{Co}{Co+Ni} = 0.85$) was heat-treated in Ar atmosphere at different temperatures up to 573 K for $2h$. The hydrogen generation yields, as a function of time, obtained by hydrolysis of alkaline $NaBH_4$ $(0.025M)$ solution using heat-treated Co-Ni-P-B powders $(15\,mg)$ are reported in Fig. 3.22. There is no much change in the catalytic activity of the Co-Ni-P-B powder after heat-treatment up to 523 K, as compared to untreated powder. The heat-treated sample at 573 K shows a decrease in the H_2 generation rate, however reaching 100% of the nominal H_2 yield. This decrease in the catalytic activity might be due to the structural variation or particle agglomeration caused by the heat-treatment. The XRD spectra of the catalyst powder show amorphous nature for both untreated (Fig. 3.17) and

heat treated Co-Ni-P-B powder at 523 K in Ar atmosphere (Fig. 3.23 A). Co-Ni-P-B powder annealed below 523 K shows similar structure and morphology as that of untreated powder and heat-treated at 523 K (figure not shown).

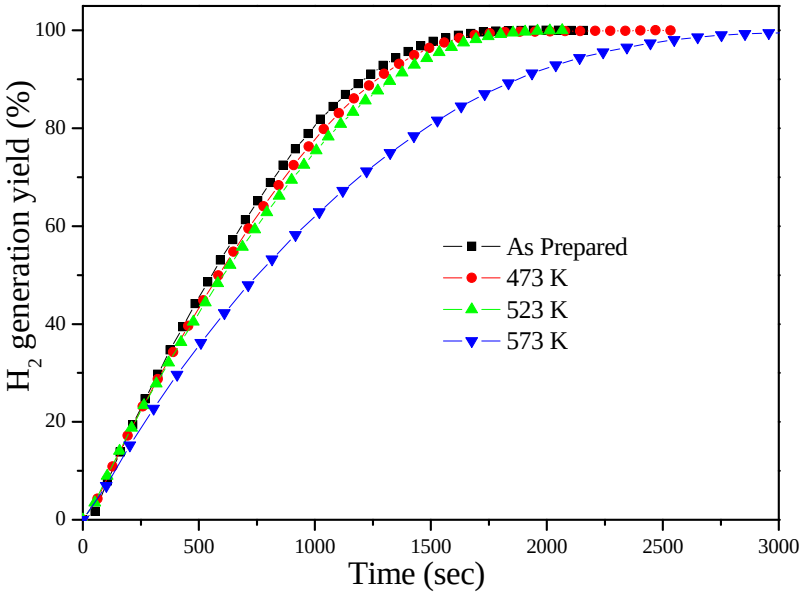

Figure 3.22 – Hydrogen generation yield as a function of reaction time obtained by hydrolysis of alkaline $NaBH_4$ (0.025 M) solution with heat-treated Co-Ni-P-B (molar ratio of B/P= 2.5 and $\frac{Co}{Co+Ni} = 0.85$) catalyst powder in Ar atmosphere at different temperatures for $2h$.

However SEM micrograph (Fig. 3.24 B) of samples treated at 573 K shows a different morphology: we see particles embedded in cotton-like filamentary matrix of nanometer size (the relevant result of Co-crystallites formation is signaled by XRD). Co metal can exhibit catalytic activity only when alloyed with metalloid atoms such as B or P: this suggests that the low catalytic activity after the heat-treatment of Co-Ni-P-B powder at 573 K may be attributed to the formation of surface Co crystallites [78]. However, heat-treatment at 573 K in Ar atmosphere for $2h$ causes partial crystallization of the powder as indicated by the presence of weak reflections of Co peaks in the XRD pattern (Fig. 3.23 B). Thus after heat-treatment at 573 K, the amorphous Co-Ni-P-B powder starts to partially decompose into crystalline Co metal phase. SEM images clearly show the same surface morphology (particle nature) for the untreated Co-Ni-P-B powder (Fig. 3.16) and heat-treated sample at 523 K in Ar atmosphere (Fig. 3.24 A).

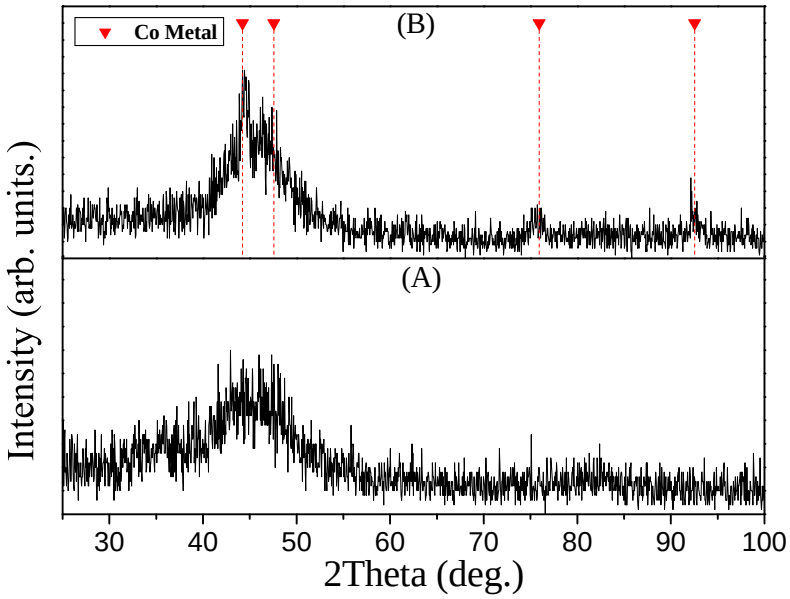

Figure 3.23 – XRD spectra of heat-treated Co-Ni-P-B (molar ratio of B/P = 2.5 and $\frac{Co}{Co+Ni}$ = 0.85) catalyst powder (A) at 523 K and (B) at 573 K in Ar atmosphere for $2h$.

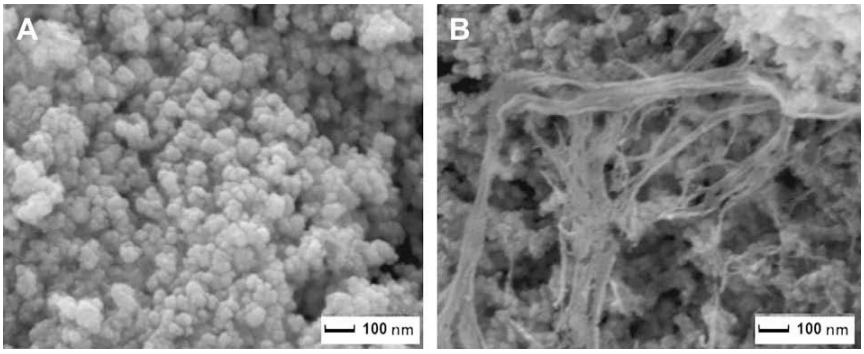

Figure 3.24 – SEM micrographs of heat-treated Co-Ni-P-B (molar ratio of B/P = 2.5 and of $\frac{Co}{Co+Ni}$ = 0.85) catalyst powder (A) at 523 K and (B) at 573 K in Ar atmosphere for $2h$

3.5 Conclusion

We have studied and compared the catalytic efficiency of amorphous Co-Ni-B, Co-B-P and Co-Ni-P-B powders in hydrogen generation by hydrolysis of $NaBH_4$. The Co-Ni-P-B catalyst exhibits the highest catalytic efficiency. To try to understand such a result we investigated the role of each chemical element in Co-Ni-B, Co-B-P and Co-Ni-P-B catalysts by regulating the B/P and Co/Ni molar ratios in the analyzed

powders. The highest efficiency of the Co-Ni-P-B powder catalyst was attributed to: 1) large active surface area, 2) amorphous short-range structure, and 3) synergic effects caused by each chemical element in the catalyst when mixed in well defined proportion (molar ratio of B/P= 2.5 and of $\frac{Co}{Co+Ni} = 0.85$). Heat-treatment at 573 K in Ar atmosphere causes a decrease in hydrogen generation rate that was attributed to partial Co crystallization in the Co-Ni-P-B powder. The synergic effects observed with Co-Ni-B and Co-P-B, now act in combined form in Co-Ni-P-B catalyst powder to lower the activation energy ($29\,kJmol^{-1}$) for hydrolysis of $NaBH_4$.

Chapter 4

Comparative studies on doped Co-B powder catalyst for hydrolysis of alkaline $NaBH_4$

"The greatest discovery of my generation is that a human being can alter his life by altering his attitudes of mind".
-William James

4.1 Introduction

Amorphous cobalt-boride (Co-B) catalysts, prepared by reduction of metal salts, have attracted great attention in catalysis owing to their unique properties such as isotropic structure, high concentration of coordinative unsaturated sites, relevant chemical stability, and low cost [100]. However, the exothermic nature of the reduction reaction involves high surface energy causing Co-B particles to agglomerate. This particle agglomeration lowers the effective surface area of the catalyst powder thus limiting its catalytic activity. In recent years, several routes have been adopted to improve the catalytic activity of the Co-B catalyst, mainly by increasing the surface area. This was achieved by depositing Co-B on a support material having high specific surface area [50, 101] or by using organic templates during the reduction reaction [102] : the final surface area of these catalyst powders is much higher than that of the ‘‘normal” Co-B powder. Another efficient route to avoid agglomeration of Co-B particles is by introducing an atomic diffusion barrier in the form of transition metals like Cr, Mo, or W [103]. These promoter metals, mainly in form of oxides, are very efficient and even a small atomic concentration significantly increases the surface area of the metal-borides catalyst powder [104] by avoiding agglomeration. In addition, they also

contribute to the overall catalytic reaction by acting as acidic sites to improve the absorption of the reactant species on the surface [105]. The second metal also acts as an electron donor ligand, thus increasing the electron density on the active metal atoms which favours the reaction kinetics [98]. These combined effects, along with the simple preparation method, make such alloy catalysts very attractive. In the present chapter, we investigated the effect of various dopant transition metals (such as *Ni, Fe, Cu, Cr, Mo,* and *W*) in Co-B catalyst powder on hydrogen production by hydrolysis of $NaBH_4$. These dopant metals behave in a specific manner to enhance the catalytic performance of the Co-B catalyst. On the basis of characterization results, the role of each metal species, in the electron exchange mechanisms involved in the $NaBH_4$ hydrolysis is discussed.

4.2 Metal doped Co-B powder catalyst.

Ternary alloy catalysts in the form of Co-Ni-B, Co-Fe-B, Co-W-B, Co-Cu-B, Co-Cr-B, or Co-Mo-B powder were synthesized by mixing nickel chloride ($NiCl_2$), iron chloride ($FeCl_2$), sodium tungstate dihydrate ($Na_2O_4W \cdot 2H_2O$) , copper nitrate ($Cu(NO_3)_2$), chromium nitrate ($Cr(NO_3)_3$), or molybdenum chloride ($MoCl_2$) salts, respectively, in the cobalt chloride ($CoCl_2$) aqueous solution. Further, these different mixture solutions were reduced by sodium borohydride ($NaBH_4$) under vigorous stirring. An excess amount of borohydride was used in order to completely reduce the metal cations. The black powder separated from the solution during reaction course was filtered and then extensively washed with distilled water and ethanol before drying at around 323 K under continuous N_2 flow. The metal to cobalt molar ratio ($\chi_M = \frac{M}{Co+M}$, where M = Ni, Fe, Cu, W, Cr or Mo) was adjusted in the final ternary alloy catalysts by varying the molar concentration of metal salts to cobalt salt in the aqueous solution. For comparison, we also prepared *Co–B* powder with same procedure by reducing only cobalt salt.

4.2.1 Effect of doped molar ratio on metal in catalyst

Firstly, the effect of dopants concentration on the catalytic activity of Co-B catalyst was studied by synthesizing the alloy catalyst with different $\frac{metal}{Co+metal}$ molar ratio χ_M. Fig. 4.1 - 4.6 presents the hydrogen generation yield, as function of time, measured by hydrolysis of alkaline $NaBH_4$ (0.025 M) solution using Co-Ni-B, Co-Fe-B, Co-Cu-B, Co-Cr-B, Co-Mo-B, and Co-W-B, catalyst powders with different Ni, Fe, Cu, Cr, Mo, and W concentration, respectively. Inset of Figs. 4.1 - 4.6 presents the plot of R_{max}

value (the maximum H_2 generation rate, for all the catalyst powders) as a function of $\chi_M\%$ (where, M = Ni, Fe, Cu, Cr, Mo, and W). The H_2 generation rate increases with the increase in $\chi_M\%$ and reaches the maximum with further increase in χ_M, the activity of the powder decreases (each measurement is repeated at least three times). The promoting effect of Cr, Mo, and W on catalytic activity is achieved at low concentration doping ($4-5\,molar\,\%$), and it is so evident that even a small amount of doping ($1\,molar\,\%$) is able to double the activity of the Co-B catalyst. Much higher concentrations of Ni, Fe, and Cu have to be used in Co-B catalyst to attain a pronounced promoting effect in H_2 generation rate. No significant effect was observed on the catalytic activity of Co-B catalyst with low concentration (below $10\,molar\%$) doping of these metals (Ni, Fe, and Cu)

Comparative analysis of the alloy catalysts powders was carried out with $\chi_M\%$ values where R_{max} is highest (see inset of Figs. 4.1 - 4.6), for the hydrolysis of $NaBH_4$. Hydrogen generation yield was measured, as a function of time, during the hydrolysis of alkaline $NaBH_4$ ($0.025M$) solution in presence of Co-B, Co-Ni-B($\chi_{Ni} = 15\%$), Co-Fe-B($\chi_{Fe} = 35\%$), Co-Cu-B($\chi_{Cu} = 35\%$), Co-Cr-B($\chi_{Cr} = 4\%$), Co-Mo-B($\chi_{Mo} = 5\%$), and Co-W-B($\chi_W = 5\%$) powder catalysts at 298 K (Fig. 4.7). The expected total amount of H_2 was measured irrespective of the type of catalyst used. The H_2 generation yield values, reported in Fig. 4.7, were perfectly fitted by using a single exponential function [99], as described by:

$$[H_2](t) = [H_2]_{max} \times (1 - e^{-k_1 t}) = 4[[BH_4^-]_0 \times (1 - e^{-k_1 t})] \tag{4.1}$$

where, $[BH_4^-]_0$ is the initial molar concentration of $NaBH_4$ in the solution and k_1 is the overall rate constant of the first-order reaction. This indicates that hydrolysis reaction is first-order reaction with respect to $NaBH_4$. In the present case, a low hydride/catalyst ratio was used which means that the first-order kinetics involving diffusion of BH_4 on the catalyst surface is the rate-limiting step during the hydrolysis reaction [99]. R_{max}, for all the catalyst powders, are summarized in Table 4.2. We observe that these values decrease in the following order: Co-Cr-B > Co-Mo-B > Co-W-B > Co-Cu-B > Co-Fe-B > Co-Ni-B > Co-B. The measurements are repeated to verify the obtained results. Co-Cr-B catalyst powder ($3400\,ml/min/g$), with $\chi_{Cr} = 4\%$, shows about four times higher H_2 generation rate when compared to that achieved with Co-B catalyst powder ($850\,ml/min/g$).

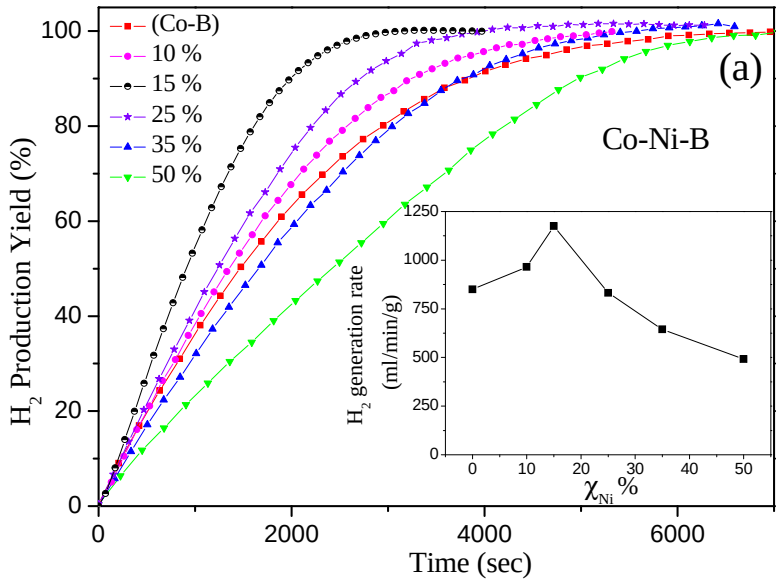

Figure 4.1 – Hydrogen generation yield as a function of reaction time obtained by hydrolysis of alkaline $NaBH_4$ (0.025 M) with Co-Ni-B with different χ_{Ni} values. Inset shows the maximum H_2 generation rate (R_{max}) as a function of χ_{Ni}.

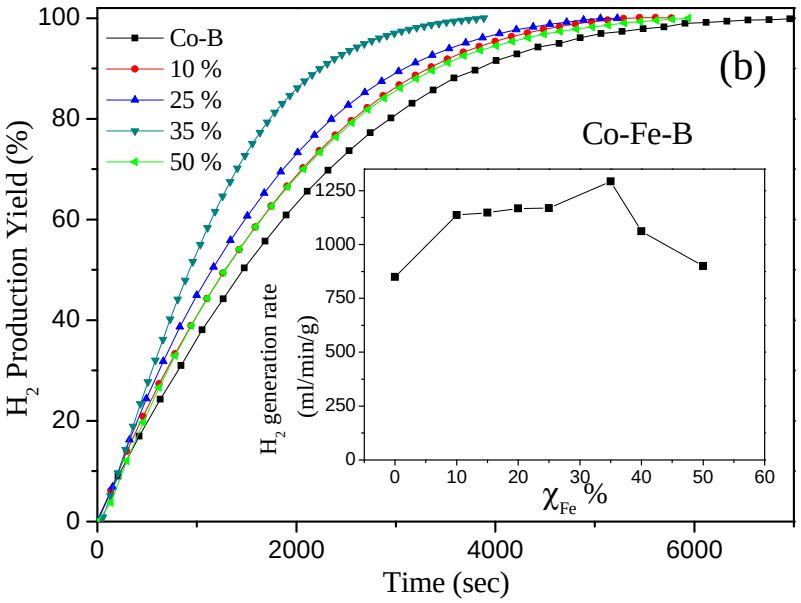

Figure 4.2 – Hydrogen generation yield as a function of reaction time obtained by hydrolysis of alkaline $NaBH_4$ (0.025 M) with Co-Fe-B with different χ_{Fe} values. Inset shows the maximum H_2 generation rate (R_{max}) as a function of χ_{Fe}.

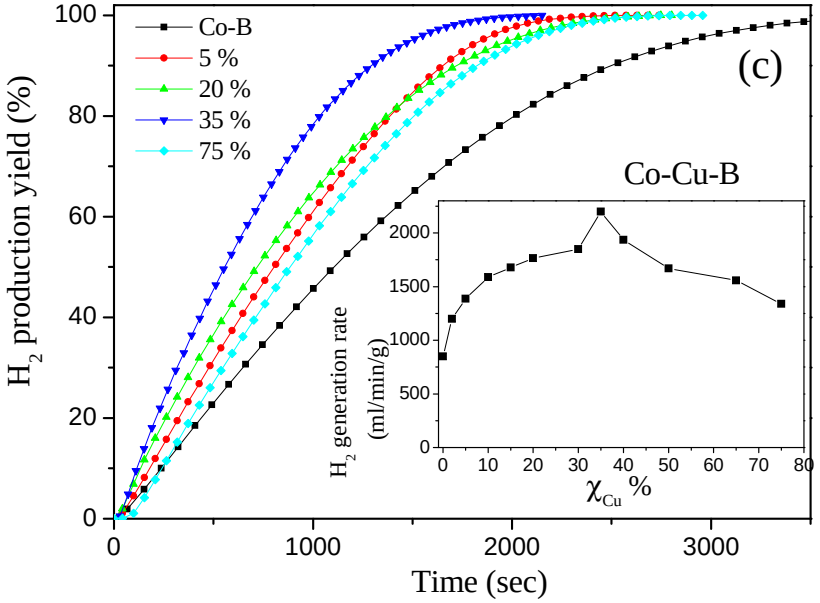

Figure 4.3 – Hydrogen generation yield as a function of reaction time obtained by hydrolysis of alkaline $NaBH_4$ (0.025 M) with Co-Cu-B with different χ_{Cu} values. Inset shows the maximum H_2 generation rate (R_{max}) as a function of χ_{Cu}.

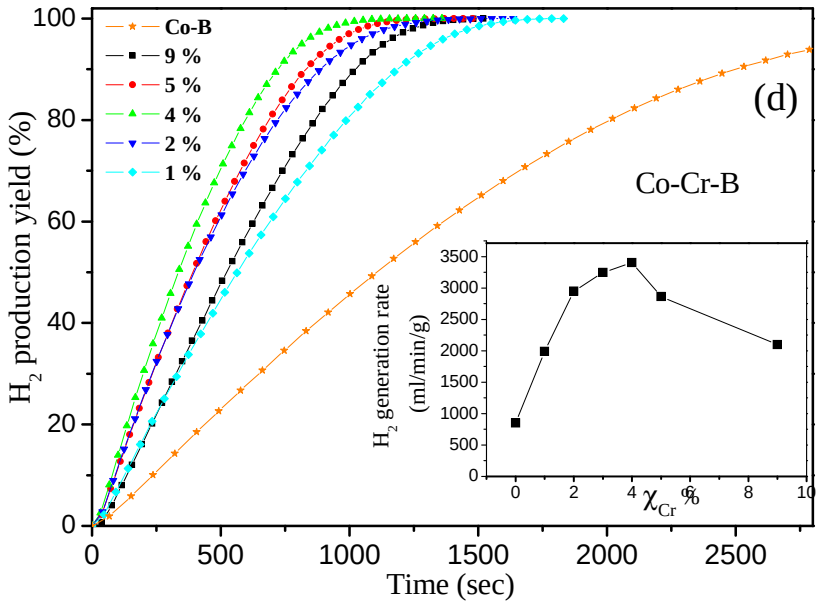

Figure 4.4 – Hydrogen generation yield as a function of reaction time obtained by hydrolysis of alkaline $NaBH_4$ (0.025 M) with Co-Cr-B with different χ_{Cr} values. Inset shows the maximum H_2 generation rate (R_{max}) as a function of χ_{Cr}.

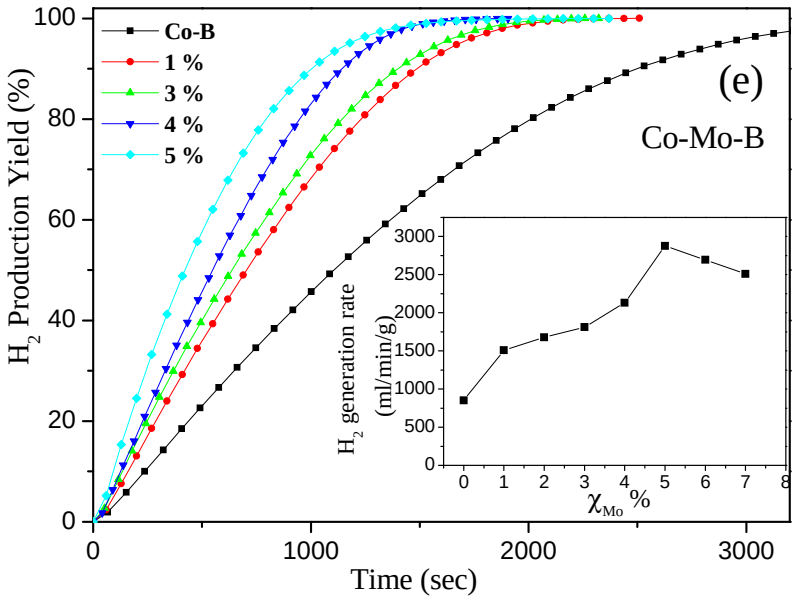

Figure 4.5 – Hydrogen generation yield as a function of reaction time obtained by hydrolysis of alkaline $NaBH_4$ (0.025 M) with Co-Mo-B with different χ_{Mo} values. Inset shows the maximum H_2 generation rate (R_{max}) as a function of χ_{Mo}.

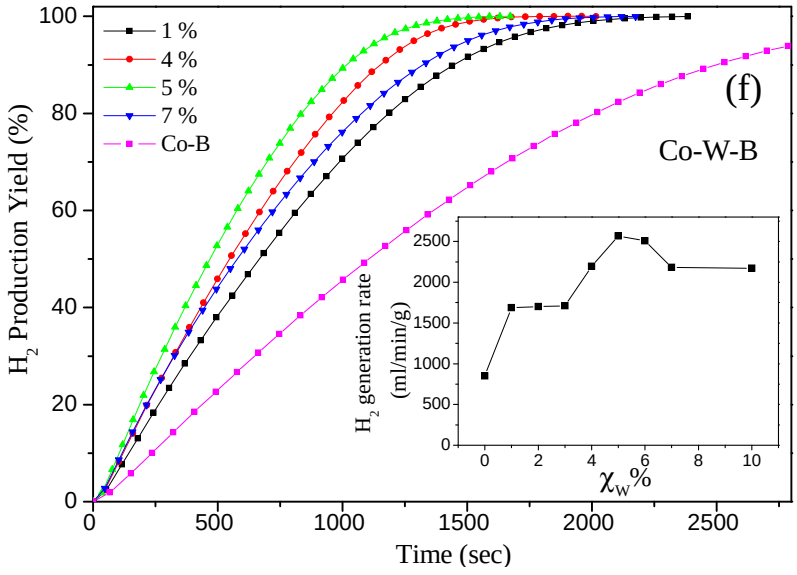

Figure 4.6 – Hydrogen generation yield as a function of reaction time obtained by hydrolysis of alkaline $NaBH_4$ (0.025 M) with Co-W-B with different χ_W values. Inset shows the maximum H_2 generation rate (R_{max}) as a function of χ_W.

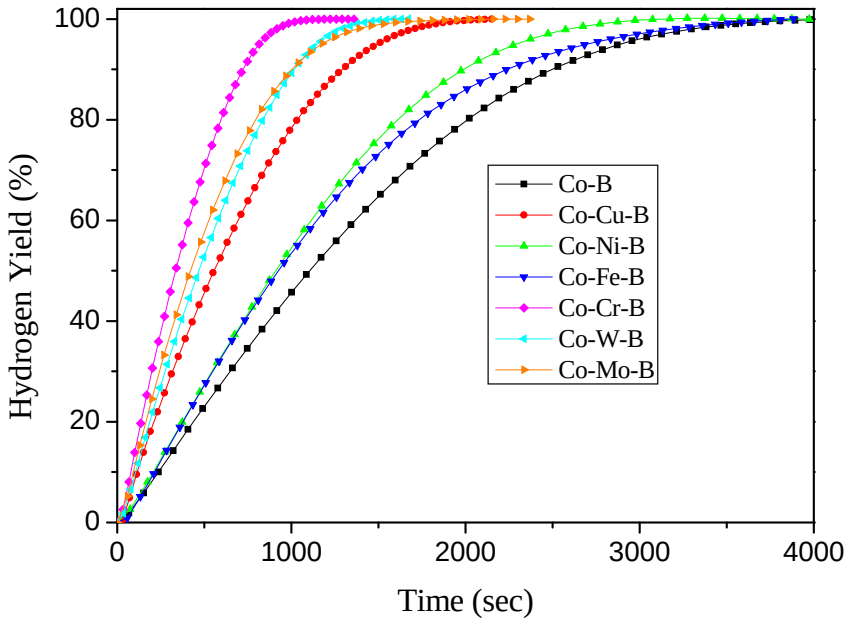

Figure 4.7 – Hydrogen generation yield as a function of reaction time obtained by hydrolysis of alkaline $NaBH_4$ (0.025 M) with of *Co-B*, Co-Ni-B (χ_{Ni} = 15%), Co-Fe-B (χ_{Fe} = 35%), Co-Cu-B (χ_{Cu} = 35%), Co-Cr-B (χ_{Cr} = 4%), Co-Mo-B (χ_{Mo} = 5%), and Co-W-B (χ_{W} = 5%) powder catalysts at 298 K

Above results prove that doping Co-B powder with any of the transition metals (Cr, Mo, W, Cu, Fe, and Ni), with small or large concentration, enhances the catalytic efficiency of the catalyst. Morphological, structural, and electronic changes, occurring in the Co-B powder with addition of the different transition metals, have been studied to understand the promoting role of each transition metal.

4.2.2 Characterization

Scanning Electron Microscope (SEM)

In Fig. 4.8, we present the SEM images of all the alloy powder catalysts. All samples show similar particle-like morphology with particles having spherical shape and size of a few nanometers. During catalyst preparation, the use of $NaBH_4$ as a reducing agent causes a fast reduction of Co ions that inhibits particle growth above a few nanometers. However, at higher SEM magnification, it is evident that these particles are mostly in agglomerated state in the case of Co-B, Co-Ni-B, and Co-Fe-B powders. On the contrary, a lower degree of agglomeration is observed with Co-Cu-B, Co-W-B, Co-Cr-B, and Co-Mo-B powders, and such a morphology is helpful to enhance the

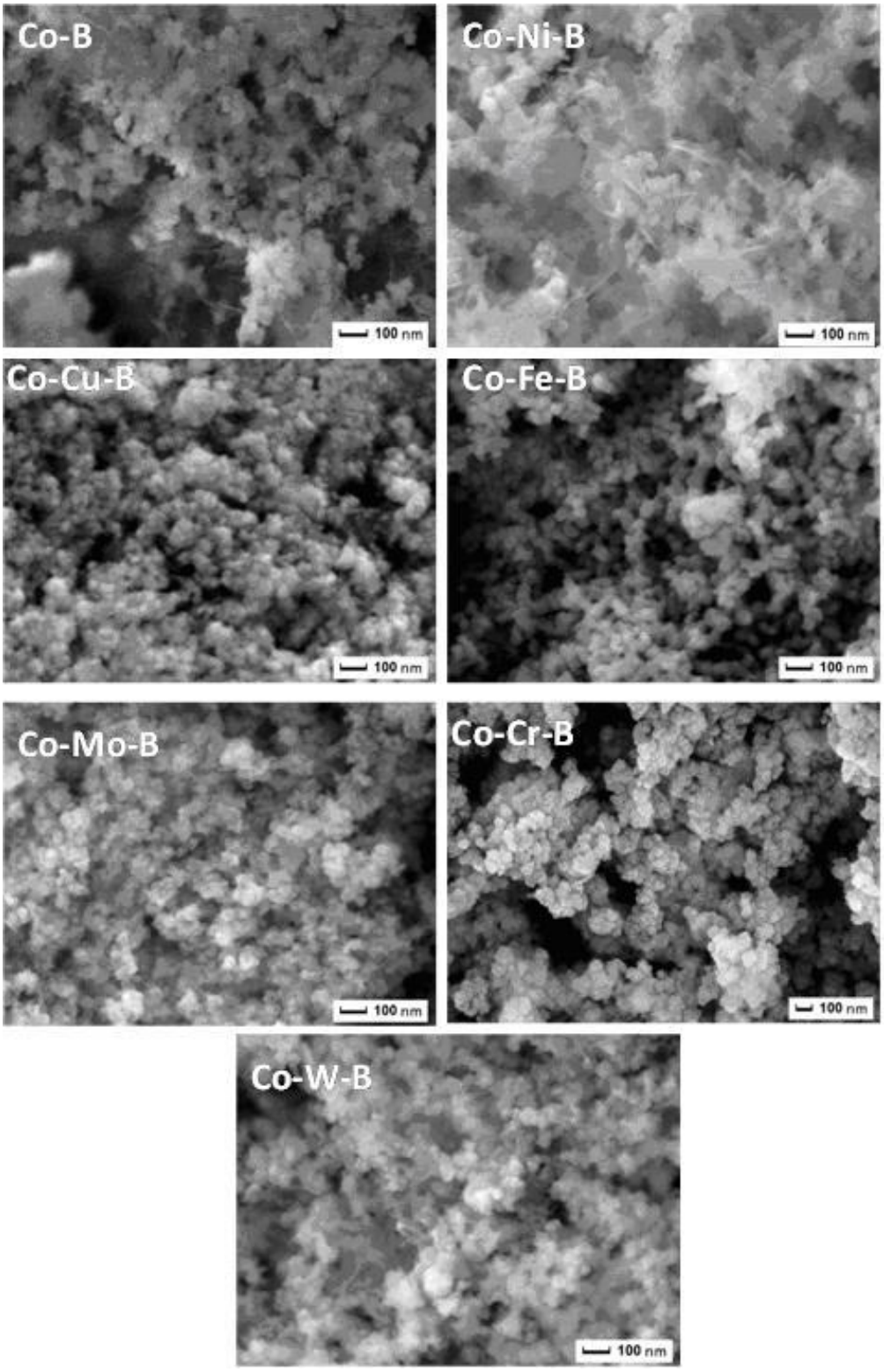

Figure 4.8 – SEM micrographs of Co-B, Co-Ni-B (χ_{Ni} = 15%), Co-Fe-B (χ_{Fe} = 35%), Co-Cu-B (χ_{Cu} = 35%), Co-Cr-B (χ_{Cr} = 4%), Co-Mo-B (χ_{Mo} = 5%), and Co-W-B (χ_{W} = 5%) powder catalysts.

active surface area of catalysts (as discussed later on the basis of BET measurement).

X-Ray Diffraction (XRD)

XRD patterns (Fig. 4.9) of all the Co-B based alloy powders show a broad peak at around $2\theta = 45^{o}$, which is assigned to the amorphous state of Co-B alloy. Other broad peaks at around 35^{o} and 43^{o}, attributed to the presence of Cr_2O_3 and Cu metal, are also observed for Co-Cr-B and Co-Cu-B catalyst powders, respectively. Finally, the diffraction spectra indicate short-range order and long-range disorder, and both these features might contribute to enhance the catalytic activity [92].

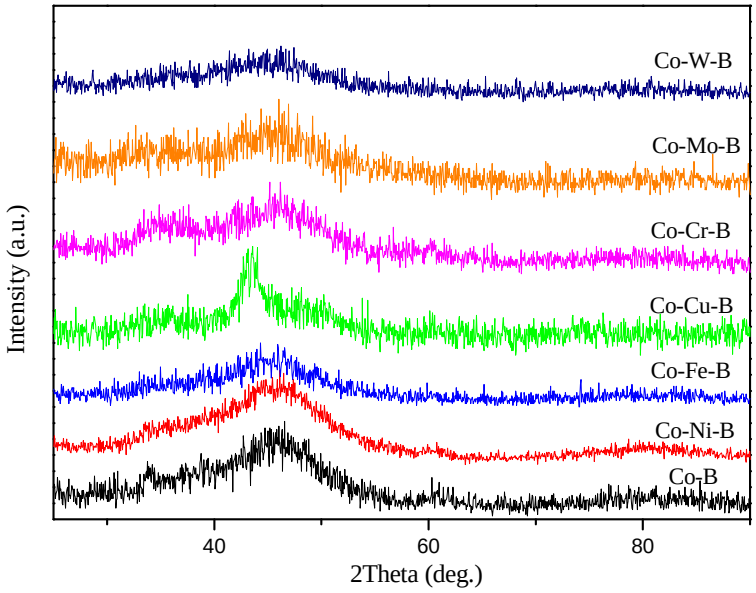

Figure 4.9 – XRD pattern of Co-B, Co-Ni-B ($\chi_{Ni} = 15\%$), Co-Fe-B ($\chi_{Fe} = 35\%$), Co-Cu-B ($\chi_{Cu} = 35\%$), Co-Cr-B ($\chi_{Cr} = 4\%$), Co-Mo-B ($\chi_{Mo} = 5\%$), and Co-W-B ($\chi_{W} = 5\%$) powder catalysts.

X-Ray Photoelectron Spectroscopy (XPS)

XPS was used to gain insight into the electronic states and surface interaction between atoms in all catalyst compounds. Fig. 4.10 a and b shows the XPS spectra of $Co_{2p_{3/2}}$ and B_{1s} electronic levels, respectively, in all the catalyst powders. Two peaks appear, for all the catalyst compounds, corresponding to the $Co_{2p_{3/2}}$ level at the binding energies (BE) in a range of $778.2 - 778.4\,eV$ and $781.6 - 781.8\,eV$. This suggests that Co element exists in both elemental and oxidized states, respectively. The +2 state related to the peak of the oxidized cobalt is attributed to $Co(OH)_2$: this

molecule would have been formed possibly during catalyst preparation [84] or when it was exposed to ambient atmosphere before transferring to the reaction chamber. This cobalt hydroxide ($Co(OH)_2$) does not cause major effects on catalytic activity, because it can be easily reduced by sodium borohydride in the course of the hydrolysis forming Co-B active phase. Liu and Li [106] showed experimentally that $Co(OH)_2$ intermediate acts as nuclei for the precipitation of Co-B active phase during the reaction with $NaBH_4$. There is no significant shift in the present Co BE peak when compared to the standard binding energy of metallic Co for all the catalyst powders, except for the Co-Ni-B catalyst. Two XPS peaks are also observed at BE values of $188.1-188.3\,eV$ and $192.1-192.3\,eV$, which correspond to elemental and oxidized B_{1s} levels, respectively, for all catalyst powders [84]. A positive shift of around $1.0-1.2\,eV$ is evident when comparing the BE of pure boron ($187.1\,eV$) to that of boron in the catalyst. This shift indicates an electron transfer from alloying B to vacant *d*-orbital of metallic Co, which makes the B atom electron deficient and the Co atom electron enriched: this is true for all the catalyst powders [94]. The lack of shift in Co peak in compound catalyst is due to the heavy mass of the atom. Fig. 4.11 presents the XPS spectra of Ni_{2p}, Fe_{2p}, Cu_{2p}, Cr_{2p}, Mo_{3d}, and W_{4f} electronic levels in Co-Ni-B, Co-Fe-B, Co-Cu-B, Co-Cr-B, Co-Mo-B, and Co-W-B, powders, respectively. The XPS result for each catalyst powder is separately discussed below:

Co-Ni-B Two peaks appear in $Ni_{2p_{3/2}}$ levels with binding energies of 852.6 and $856.3\,eV$ (Fig. 4.11 a), indicating that Ni metal exists in both the elemental and oxidized states, respectively. The oxide is mainly in the form of $Ni(OH)_2$ which would have been formed during the catalyst preparation reaction between $NaBH_4$ and metal salts, similarly to cobalt oxide. However, only a few amount of Ni is present in oxidized form ($15\,at.\%$), while most of it is in the form of metallic Ni ($85\,at.\%$). The BE of metallic Co in Co-Ni-B is $0.2\,eV$ lower than that in the Co-B, whereas BE of metallic Ni in Co-Ni-B is also $0.2\,eV$ lower than that in Ni-B [98]. This proves that in Co-Ni-B catalyst, there is an electronic enrichment on Co and Ni metals when compared with the Co-B and Ni-B catalysts: this is mainly attributed to the B-enrichment in Co-Ni-B catalyst as seen by the compositional analysis of XPS spectra (as reported in our previous Chapter and also reported by Li et al. [89]). These authors also performed theoretical calculations using DFT method to show that the increase in the B content on the surface would contribute more electrons to metallic Ni or Co in their corresponding amorphous alloys.

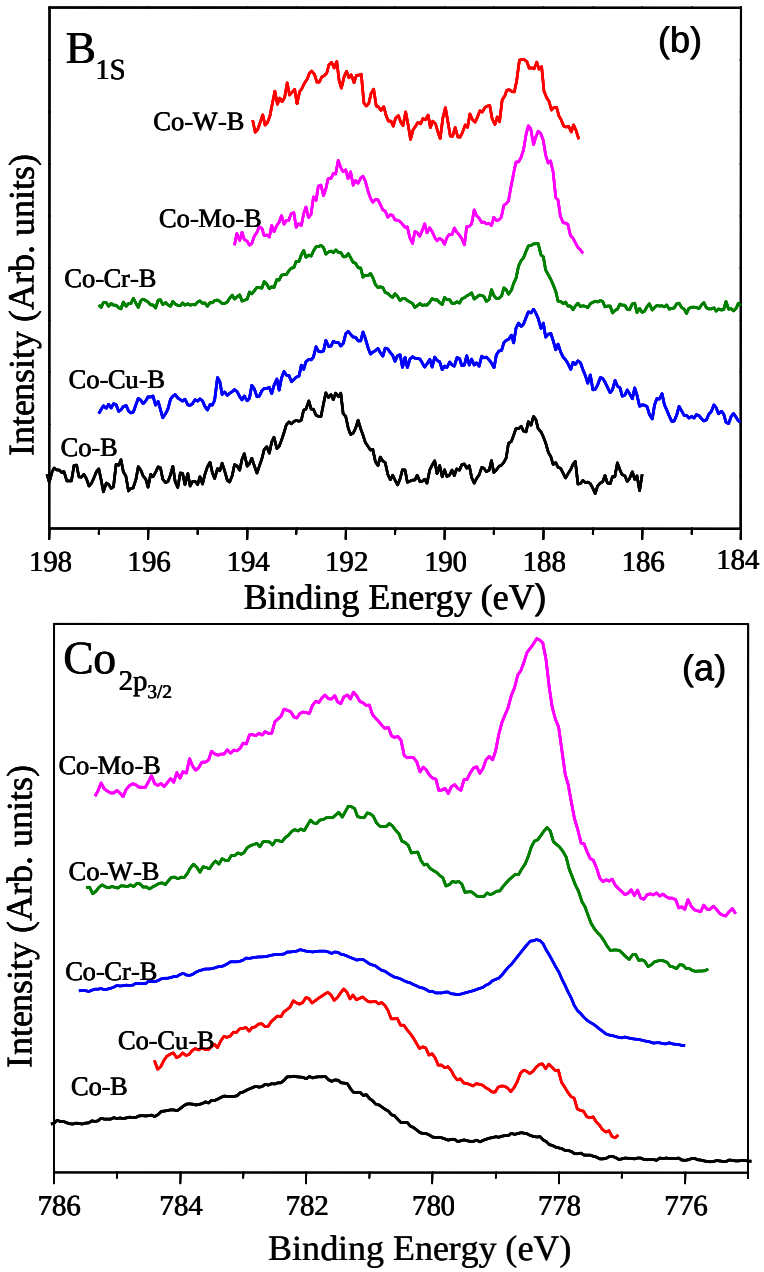

Figure 4.10 – X-ray photoelectron spectra of $Co_{2p_{3/2}}$ and B_{1s} levels for Co-B, Co-Ni-B ($\chi_{Ni} = 15\%$), Co-Fe-B ($\chi_{Fe} = 35\%$), Co-Cu-B ($\chi_{Cu} = 35\%$), Co-Cr-B ($\chi_{Cr} = 4\%$), Co-Mo-B ($\chi_{Mo} = 5\%$), and Co-W-B ($\chi_{W} = 5\%$) powder catalysts.

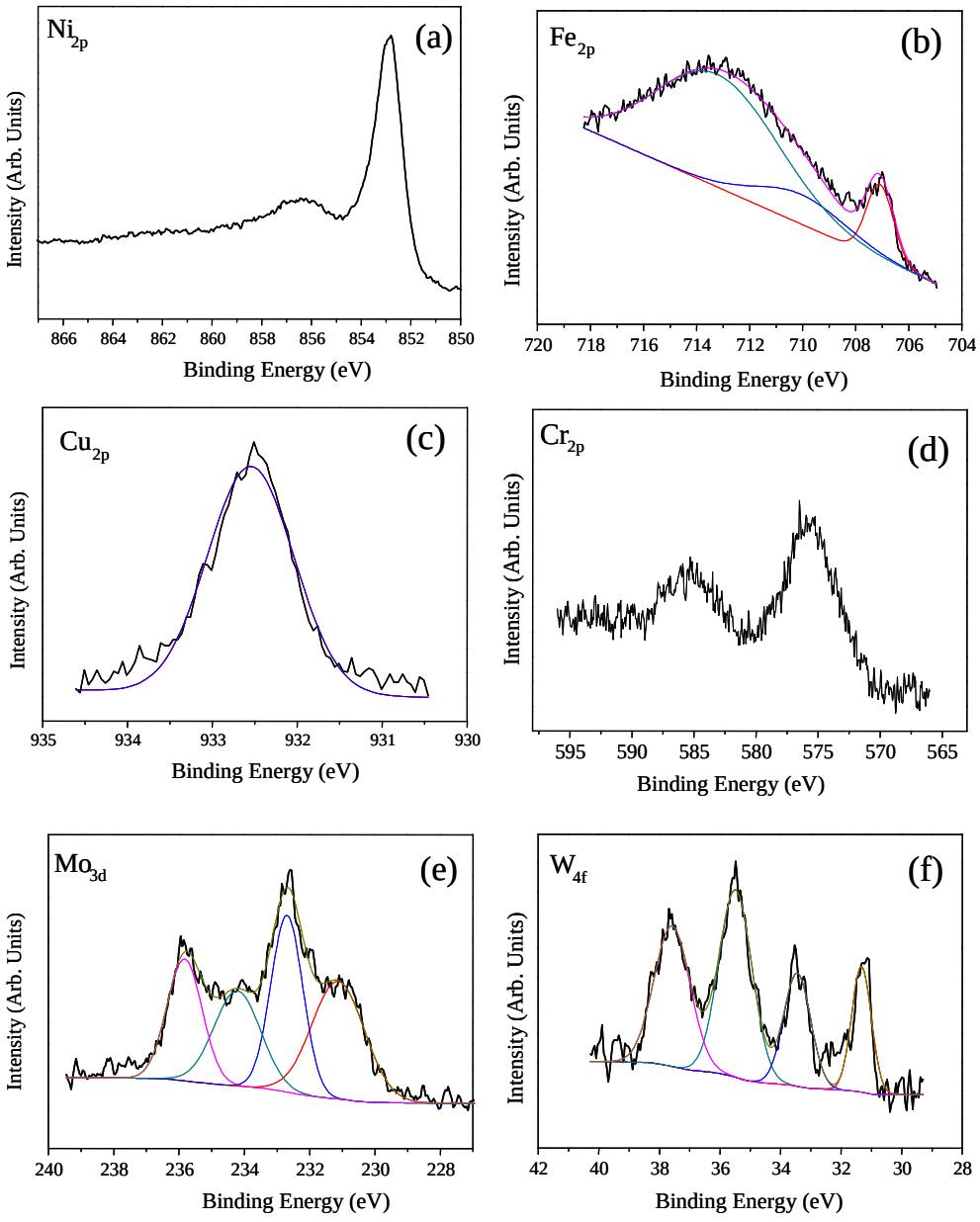

Figure 4.11 – X-ray photoelectron spectra of (a) Ni_{2p} level for Co-Ni-B ($\chi_{Ni} = 15\%$), (b) Fe_{2p} level for Co-Fe-B ($\chi_{Fe} = 35\%$), (c) Cu_{2p} level for Co-Cu-B ($\chi_{Cu} = 35\%$), (d) Cr_{2p} level for Co-Cr-B ($\chi_{Cr} = 4\%$), (e) Mo_{3d} level for Co-Mo-B ($\chi_{Mo} = 5\%$) and (f) W_{4f} level for Co-W-B ($\chi_{W} = 5\%$) powder catalysts

Co-Fe-B The elemental Fe in Co-Fe-B catalyst is present in both metallic and oxidized state with binding energies of 707.1 and 712.7 eV, respectively (Fig. 4.11 b). The oxidized Fe species on the catalyst surface is mostly in the form of Fe_2O_3 state (90 $at.\%$) probably formed during the preparation. The metallic Fe (10 $at.\%$) shows a positive shift of about 0.3 eV in its corresponding BE peak, which suggests electron transfer from Fe to Co atoms. However, no shift is observed in the BE of the Co peak probably because very few Fe atoms are present in metallic state to transfer electrons to Co atoms.

Co-Cu-B For Cu, only a single peak corresponding to a metallic state is apparent at BE of 932.6 eV (Fig. 4.11 c). This is consistent with XRD result which signals indeed the presence of metallic Cu. In addition, no shifts in the BE of Co and Cu peaks are observed indicating the lack of electronic interaction between these atoms. The electronic exchange between Co and B atoms is also not affected by the Cu addition.

Co-Cr-B The Cr_{2p} spectrum for Co-Cr-B catalysts exhibits two peaks at 575.7 and 585.3 eV (Fig. 4.11 d), attributed to $Cr_{2p_{3/2}}$ and $Cr_{2p_{1/2}}$peaks of Cr^{3+} species, respectively. This shows that Cr is in completely oxidized state (Cr_2O_3), which is in agreement with the XRD result. It is also noticed that Cr does not modify the electronic interaction between Co and B, because their relevant BEs remain unchanged after the Cr addition.

Co-Mo-B The XPS spectra of Mo $3d$ levels (Fig. 4.11 e) reveal two peaks assigned to MoO_2 (BE of 231.1 and 232.6 eV are ascribed to Mo $3d_{5/2}$ and Mo $3d_{3/2}$levels of Mo^{4+}, respectively) and two peaks assigned to MoO_3 (BE of 233.7 and 235.8 eV are ascribed to Mo $3d_{5/2}$ and Mo $3d_{3/2}$ levels of Mo^{6+}, respectively). There is no evidence of metallic Mo in the spectra indicating that Mo atoms on the catalyst surface are in completely oxidized state. The BE value for Co and B is unaffected by the addition of Mo in Co-B catalyst.

Co-W-B The $W-4f$ spectrum (Fig. 4.11 f) of Co-W-B catalyst shows the presence of both oxidized and elemental state of W. The XPS spectrum of $W_{4f_{7/2}}$ ($4f_{5/2}$) shows two peaks at BE values of 31.3 (33.4) eV and 35.5 (36.9) eV assigned to metallic W and WO_3 species, respectively. About 33% of the XPS signal rises from elemental W, whereas 67% is associated to the oxidized W. By comparing with the undoped Co-B sample, no significant change in XPS spectra is observed

in connection with the presence of the W-dopant: this means that W does not affect the electronic states of Co and B.

The above XPS results prove that all the transition metal dopants in Co-B catalyst exist in different states (elemental, oxidized, oxidized in different proportion). This may be the prime reason to explain the different promoting effects on Co-B catalyst powders as we will discuss in the following sections.

BET (Brunauer, Emmett & Telle) surface area measurement

Gas adsorption is the most widely used and accurate technique for total surface area measurements. The BET surface area of the powder catalysts was determined by nitrogen absorption at 77 K (Micromeritics ASAP 2010) after degassing. The measured BET surface area of all the catalyst powders is reported in Table 4.2. The specific surface area decreases in following order: Co-Cu-B>Co-W-B>Co-Mo-B>Co-Cr-B>Co-Fe-B>Co-Ni-B>Co-B. This shows that doping the Co-B catalyst with transition metals (Cr, Mo, W, Fe, Cu and Ni) causes an increment in the specific surface area irrespective of the type of dopant. However, the trend obtained in the increment of the surface area is quite different from that of the catalytic activity (Fig. 4.7). When small amount of Cr, Mo, or W ($\chi_{Cr,Mo,W} = 4 - 5$) is included as a dopant in Co-B, the specific surface area of the catalyst increases by almost $2 - 2.5$ times, due to the limited particle agglomeration process when compared to pure Co-B (see Fig. 4.8). Surface characterization (Figs. 4.8, 4.10 and 4.11) of these catalyst powders suggests that Cr, Mo, and W in the form of oxides are located on the surface of the catalyst. These metal oxides act as a kind of atomic barrier between the several Co-B nanoparticles, thus avoiding agglomeration caused by their high surface energy. As a result, the effective surface area increases significantly for Co-Cr-B, Co-Mo-B, and Co-W-B catalyst. A remarkable increment in the surface area, a factor of about 5.5, is observed for Co-Cu-B catalyst when compared to undoped Co-B. As observed by XRD and XPS, the Cu on the catalyst surface is in completely metallic state which prevents the agglomeration of Co-B nanoparticles. The highest surface area of Co-Cu-B is mainly due to the high concentration of Cu when compared to Cr, Mo, and W-dopant in Co-B catalyst. When Cr is added at high concentration ($\chi_{Cr} = 10\%$) in Co-B catalyst, the surface area increases by one order of magnitude when compared to undoped Co-B catalyst [104]. Similar result is reported by Chen et al. for Mo-promoted Co-B catalyst. However, a deleterious effect in catalytic activity is detected with high concentration of the dopant metals (Cr, Mo, and W) as we will

Catalyst powders	$\frac{M}{M+Co}$ molar ratio $(\chi_M)(\%)$	BET surface area (m^2/g)	Max H_2 generation rate (R_{max}) $(ml/min/g\,catalyst)$		Lewis acid	Activation energy $(kJmol^{-1})$
			Alkaline $NaBH_4$	Non-alkaline $NaBH_4$		
Co–B		20	850	860	No	45
Co–Ni–B	15	22	1175	1160	No	34
Co–Fe–B	35	33	1300	1270	No	31
Co–Cu–B	35	115	2210	2180	No	30
Co–Cr–B	4	40	3400	2250	Yes	37
Co–Mo–B	5	43	2875	2210	Yes	39
Co–W–B	5	54	2570	1940	Yes	41

Table 4.2 – Molar ratio (%) of $\frac{M}{Co+M}$ (χ_M, where M stands for: Ni, Fe, Cu, Cr, Mo, and W), surface area, maximum H_2 generation rate, ability to act as Lewis acid sites, and activation energy of the as-prepared alloy catalyst powders

discuss later. Co-Fe-B shows a moderate enhancement in the surface area, when compared to Co-B, even at high concentration of Fe ($\chi_{Fe} = 35\%$), probably attributed to the formation of Fe_2O_3 on the surface. On the other hand, negligible rise in surface area is monitored for Co-Ni-B catalyst powder. For the moment, it is not clear why Fe and Ni are ineffective to significantly increase the surface area of Co-B powder.

Role as Lewis acid site

In a binary metal alloy catalyst, the addition of a new metal, or its oxide, may act as an electrophilic or Lewis acid site for the absorption and activation of the reactants to increase the overall reaction rate. To establish the possible role of the dopant metal as a Lewis acid site in CoB catalyst, it is initially important to recall the $NaBH_4$ hydrolysis mechanism involving a solid-state catalyst. The H_2 production from the metal-catalyzed hydrolysis reaction of $NaBH_4$ takes place, according to Guella et al. [49][1], by the following kinetics steps: (1) BH_4^- ions are chemisorbed on the metal (Co) atoms; (2) H^- is transferred from BH_4^- to an unoccupied adjacent (Co) metal atom; (3) the hydrogen atom acquires an electron from the metal and leaves the site in hydridic form (H^-), while BH_3^- species remains attached to the Co atom; (4) this H^- reacts with water molecule to produce H_2 and OH^-; and (5) OH^- reacts with boron in BH_3^- to produce the $BH_3(OH)^-$ ion. Again, H is transferred from $BH_3(OH)^-$ ion to an unoccupied adjacent (Co) metal atom. The cycle of hydrogen absorption on metal sites continues till $BH_3(OH)^-$forms $B(OH)_4^-$ and molecular hydrogen is released during each cycle. However, during the last step, the reaction between OH^- and BH_3^- ions is not favoured by the catalyst which may cause lower reaction rate. In present Co-B-based alloy catalyst, the dopant metal or its oxides may act as the Lewis acid sites, which are readily available for the absorption of Lewis base such as OH ions. During the hydrolysis reaction, the hydroxyl molecule in the solution can be absorbed on these sites via donating the lone electron from OH group. This bonding polarizes the hydroxyl group, which creates favourable condition for the reaction with BH_3^- ions attached to the neighbouring active Co sites and thus increasing the overall reaction rate. A set of experiments was conducted to find out which dopant transition metal in Co-B catalyst acts as Lewis acid site to assist the absorption of the OH ions. For the catalytic hydrolysis reaction, two types of hydride solution ($0.025M$) were prepared, namely: (1) $NaBH_4$ solution stabilized with $NaOH$ ($0.025M$) (designated as solution A) and (2) $NaBH_4$ solution without $NaOH$ (designated as solution B). The hydrogen generation rate

[1]See Appendix B

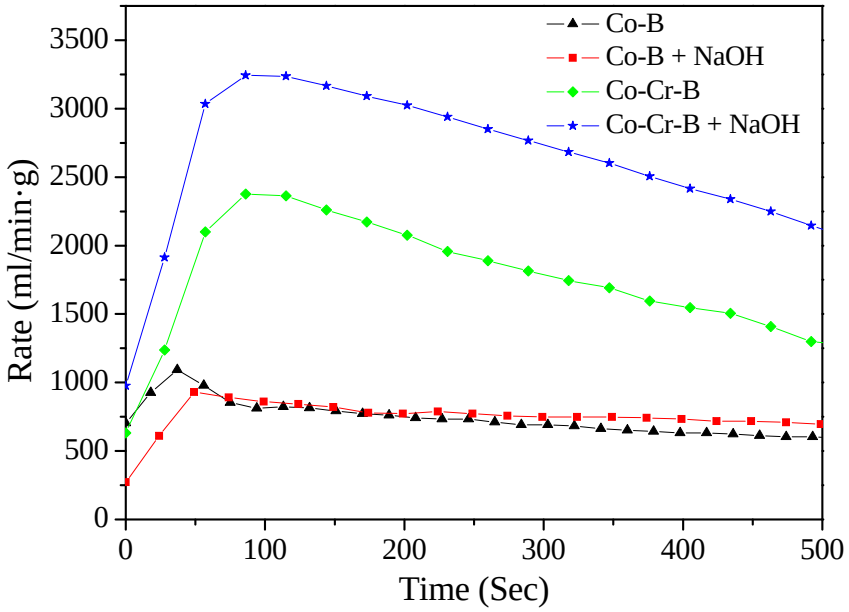

Figure 4.12 – Hydrogen generated rate as a function of reaction time obtained by hydrolysis of alkaline and non-alkaline $NaBH_4$ solution using Co-B, and Co-Cr-B ($\chi_{Cr} = 4\%$) catalyst powders

was measured by hydrolysis of solutions A and B using all the alloy catalyst powders and reported in Table 4.2. No significant change in H_2 generation rate was observed through hydrolysis of alkaline and non-alkaline $NaBH_4$ in the presence of Co-B, Co-Ni-B, Co-Fe-B, or Co-Cu-B catalyst powders. On the contrary, the H_2 generation rate obtained in the presence of Co-Cr-B, Co-Mo-B, or Co-W-B for solution A was much higher than that of solution B (see Fig. 4.12). This proves that during the hydrolysis reaction, in the presence of hydroxyl molecule in the solution, Cr, Mo, and W species, in the form of oxides, act as the Lewis acid sites to absorb the OH group and catalyze the reaction between OH and boron species (BH_3^-, $BH_2(OH)^-$, and $BH(OH)_2^-$). However, it is observed that the increment in H_2 generation rate, by addition of $NaOH$ during the hydrolysis of $NaBH_4$, is far better for Co-Cr-B catalyst when compared to Co-Mo-B or Co-W-B catalyst powders. The Cr^{3+}species might have a stronger affinity for the oxygen of hydroxyl group than W^{4+} or Mo^{4+} species, thus Cr-additives exhibit a stronger promoting effect than *Mo-* or *W*-additives.

4.2.3 The role of each dopant transition metal in Co-B catalyst, in enhancing the H_2 generation rate

Co-Ni-B catalyst Nickel on the catalyst surface is mostly in a metallic state, which neither increases the surface area of Co-B powder significantly nor acts as a

Lewis acid site for OH^- ions absorption. However, Ni is able to increase the density of electrons on the Co active sites due to boron enrichment. These electron-enriched metal active sites will favor the catalysis reaction by providing the electrons required by the hydrogen atom during the hydrolysis reaction. Thus, the catalytic activity is moderately higher for Co-Ni-B catalyst, when compared to the Co-B, due to the electron-enriched active metal site: this is the case for the Ni-doping concentration with $\chi_{Ni} = 10\%$ and 15%. However, the H_2 generation rate is maximum with $\chi_{Ni} = 15\%$ and further increase in Ni concentration causes the activity to decrease. As observed in our previous chapter (see Fig. 3.4), Co-B showed much higher catalytic activity when compared to Ni-B for hydrolysis of $NaBH_4$, thus indicating that Co metal is a more active site than Ni for catalytic hydrolysis reaction. The decrement in the activity by increasing the amount in Ni is due to the fact that more active Co sites are replaced by less active Ni sites.

Co-Fe-B catalyst By increasing χ_{Fe}, the activity of Co-Fe-B catalyst first increases and then decreases. The maximum activity is obtained with $\chi_{Fe} = 35\%$. By knowing that Fe-B alloy catalyst is less active than Co-B for the hydrolysis of $NaBH_4$, it is easily understood that only metallic Co acts as a main active site in the Co-Fe-B alloy and that Fe-dopant behaves as a promoter. At χ_{Fe} values from 10% to 35%, the promoting effect of Fe-dopant is mainly attributed to the increased surface area of the Co-Fe-B catalyst due to the existence of Fe_2O_3 species, on the catalyst surface, which act as an inhibitor against agglomeration of the Co-B particles. The presence of a little amount of metallic Fe could also make a minor contribution to the enhancement of catalytic activity by electron transfer to the active Co sites as observed by XPS (Fig. 4.11 b). Electron-enriched Co active sites will facilitate the catalysis reaction as explained for previous Co-Ni-B catalyst. At larger concentration of Fe-dopant, the catalytic activity decreases because too many surface Co active sites would be covered by inactive Fe species.

Co-Cu-B catalyst As with the above two catalysts, Co-Cu-B catalyst also requires high dopant (Cu) concentration to have the promoting effect. The catalytic activity increases with the amount of Cu-dopant in Co-B alloy catalyst, it reaches maximum at the optimum concentration of $\chi_{Cu} = 35\%$, then it decreases. Copper, in fully metallic state, is unable to either cause any electron transfer to active Co site or act as Lewis acid site for OH^- ions absorption. However, Cu

on the catalyst surface acts as a promoter by increasing the specific surface area by more than five times, when compared to Co-B catalyst, by preventing particle agglomeration. According to the above reported hydrolysis reaction mechanism, the initial reaction occurs between BH_4^- ions and metal sites, which means that the reaction rate is proportional to the number of available metal sites for the absorption of BH_4^- ions in the solution. In this reaction scheme, the Co-Cu-B catalyst powder, having a surface area almost five times higher than that of Co-B, may provide an ideal condition for BH_4^- ions absorption for catalytic hydrolysis reaction. However, a concentration of the Cu promoters exceeding $\chi_{Cu} = 35\%$ is deleterious to the hydrolysis reaction, because major portion of the surface Co active sites would be covered by the Cu metallic species.

Co-Cr-B, Co-Mo-B, Co-W-B catalysts These three powders seem to be acting as a catalyst with a similar mechanism, because in all the three cases, a small amount of dopant (Cr, Mo, or W) is enough to create the promoting effect in the Co-B catalyst. Even in these cases, by increasing the dopant concentration, the activity first increases and then decreases. The optimum contents of Cr, Mo, and W promoters are: $\chi_{Cr} = 4\%$, $\chi_{Mo} = 5\%$, and $\chi_W = 5\%$, respectively. The promoting effect is mainly caused by the corresponding oxide species of the dopant transition metals (Cr, Mo, or W) which, on the catalyst surface, inhibit the particle agglomeration thus increasing the surface area of the Co-B catalyst by favoring a better dispersion of the particles. In addition, the Cr^{3+}, Mo^{4+}, and W^{4+} species also act as Lewis acid sites for OH^- absorption due to the strong affinity of these sites toward oxygen of the OH^- group. A polarization of the *O-H* bond occurs which favors the reaction between hydroxyl group and boron species attached to the neighboring Co active sites. In conclusion, the oxide species provide high surface area and act as Lewis absorption sites for OH^- ions: these are the two main reasons involved in the significant enhancement of R_{max} observed for Co-Cr-B, Co-Mo-B, and Co-W-B catalysts with respect to that observed with the Co-B catalyst. *Cr*-doped Co-B shows the highest R_{max} when compared to *W*- and *Mo*-doping: this is attributed to the superior capability of Cr^{3+} species to absorb OH group ions. The deleterious effect on catalytic activity at higher dopant content is attributed to the surface covering of the active Co metal by Cr, Mo, or W species. To summarize, the transition metals Ni, Fe, Cu, Cr, Mo, and W, when added to the Co-B, promote the catalysis efficiency through three effects, namely by: 1. Creating higher electron density on to the active Co sites. 2. Increasing the specific surface area of

the final catalyst powder by inhibiting Co-B particle agglomeration and thus favouring better particle dispersion. 3. Acting, in the form of oxides on the catalyst surface, as the Lewis acid sites for the absorption of OH^- group ions and catalyzing its reaction with boron species. The investigated transition metals are able to enhance the catalytic efficiency of the Co-B catalyst by only one of the three above effects (Co-Ni-B and Co-Cu-B catalyst) or a combination of two effects (Co-Cr-B, Co-Mo-B, Co-W-B, and Co-Fe-B catalyst).

4.3 Activation Energy of metal doped Co-B powder catalyst

The H_2 generation yield as a function of time was measured at different solution temperatures by hydrolysis of alkaline $NaBH_4$ (0.025 M) solution using Co-Ni-B ($\chi_{Ni} = 15\%$), Co-Fe-B ($\chi_{Fe} = 35\%$), Co-Cu-B ($\chi_{Cu} = 35\%$), Co-Cr-B ($\chi_{Cr} = 4\%$), Co-Mo-B ($\chi_{Mo} = 5\%$), and Co-W-B ($\chi_{W} = 5\%$) powder catalysts as reported in Figs. 4.13 - 4.18, respectively. As expected, H_2 generation rate increases with the temperature. Using the Arrhenius plot (inset of Figs. 4.13 - 4.18) for the hydrogen production rate, the activation energies are obtained and summarized in Table 4.2. The results clearly show that in Co-B catalyst doped with transition metal, the activation energy is always lower when compared to undoped Co-B catalyst powder ($45\,kJmol^{-1}$) Fig. 3.6 [98]. In general, the obtained activation energies are lower than that obtained with *Raney Co* ($53.7\,kJmol^{-1}$) [53], carbon supported Co-B ($57.8\,kJmol^{-1}$) and Co-B nanoparticles ($42.7\,kJmol^{-1}$) [107]. The values are also lower than that found by Amendola ($47\,kJmol^{-1}$) [16] by using Ru catalyst. Kaufman and Sen [45], by using different bulk metal catalysts, obtained $75\,kJmol^{-1}$ for cobalt, $71\,kJmol^{-1}$ for nickel, and $63\,kJmol^{-1}$ for Raney nickel. The activation energy values obtained in the present case are comparable to that obtained with nanoparticle-assembled Co-B thin film ($30\,kJmol^{-1}$) [97], Pd/C powder ($28\,kJmol^{-1}$)) [108], Co supported on $\gamma - Al_2O_3$ ($33\,kJmol^{-1}$)) [101], Ru nanoclusters ($29\,kJmol^{-1}$) [52], and Ru-C ($37\,kJmol^{-1}$) [109]. The favorable activation energy values obtained in the present work are attributed to promoting effects, caused by the different transition metals, to enhance the catalytic hydrolysis reaction.

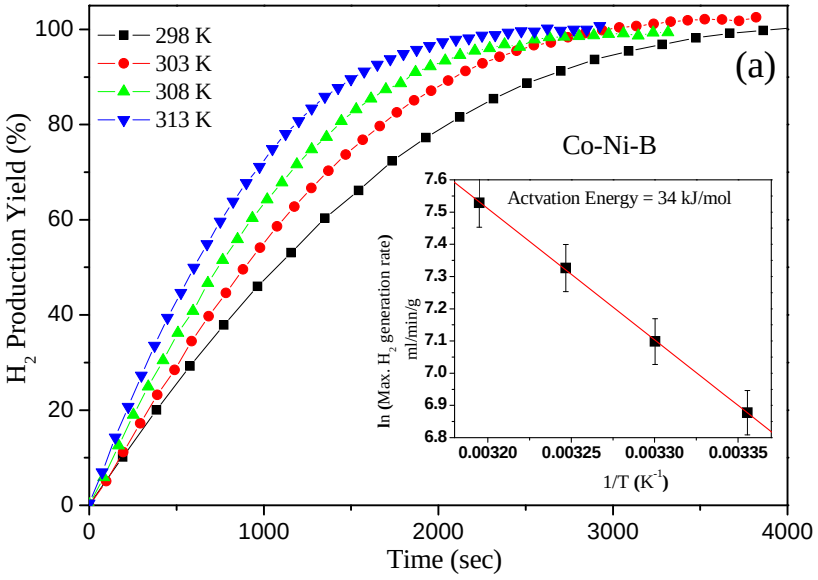

Figure 4.13 – Hydrogen generation yield as a function of reaction time by hydrolysis of alkaline $NaBH_4$ (0.025 M) solution measured at different solution temperatures with Co-Ni-B ($\chi_{Ni} = 15\%$) powder catalysts. Inset shows the Arrhenius plot of the H_2 generation rates.

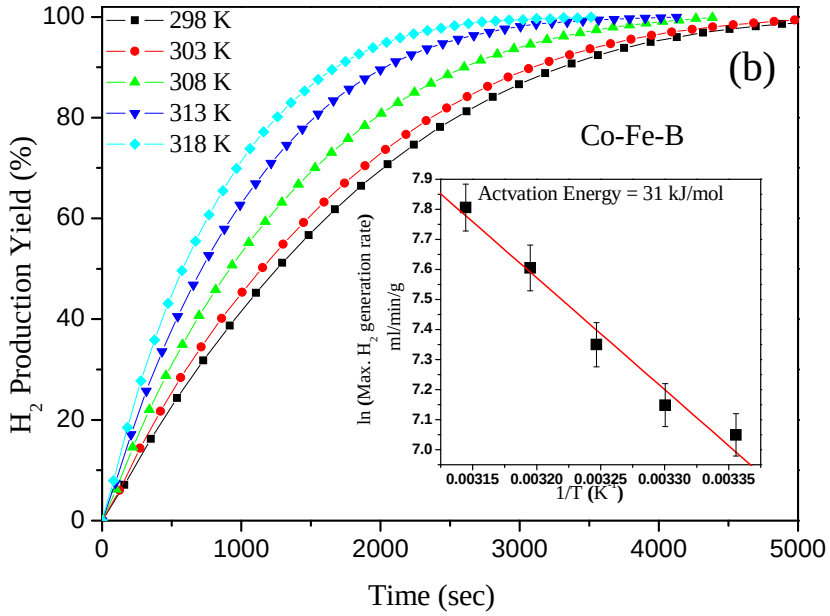

Figure 4.14 – Hydrogen generation yield as a function of reaction time by hydrolysis of alkaline $NaBH_4$ (0.025 M) solution measured at different solution temperatures with Co-Fe-B ($\chi_{Fe} = 35\%$) powder catalysts. Inset shows the Arrhenius plot of the H_2 generation rates.

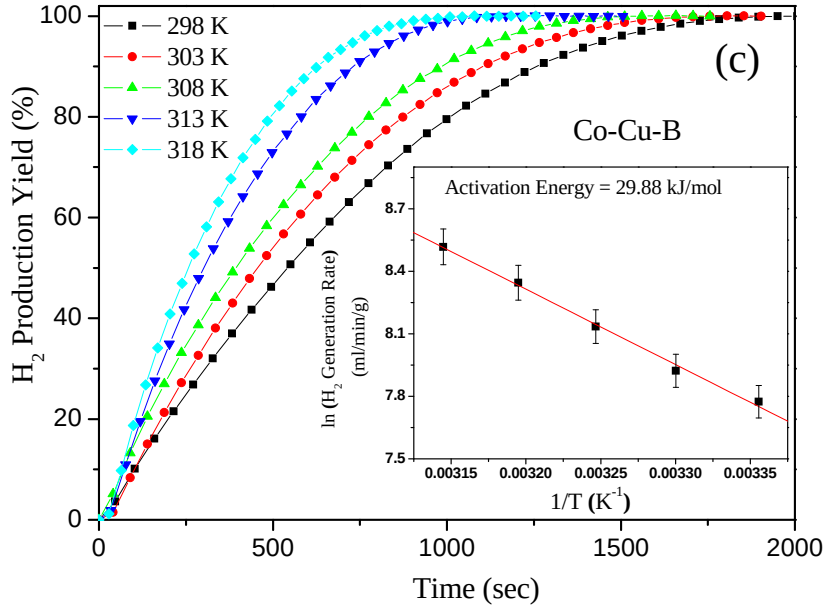

Figure 4.15 – Hydrogen generation yield as a function of reaction time by hydrolysis of alkaline $NaBH_4$ (0.025 M) solution measured at different solution temperatures with Co-Cu-B ($\chi_{Fe} = 30\%$) powder catalysts. Inset shows the Arrhenius plot of the H_2 generation rates.

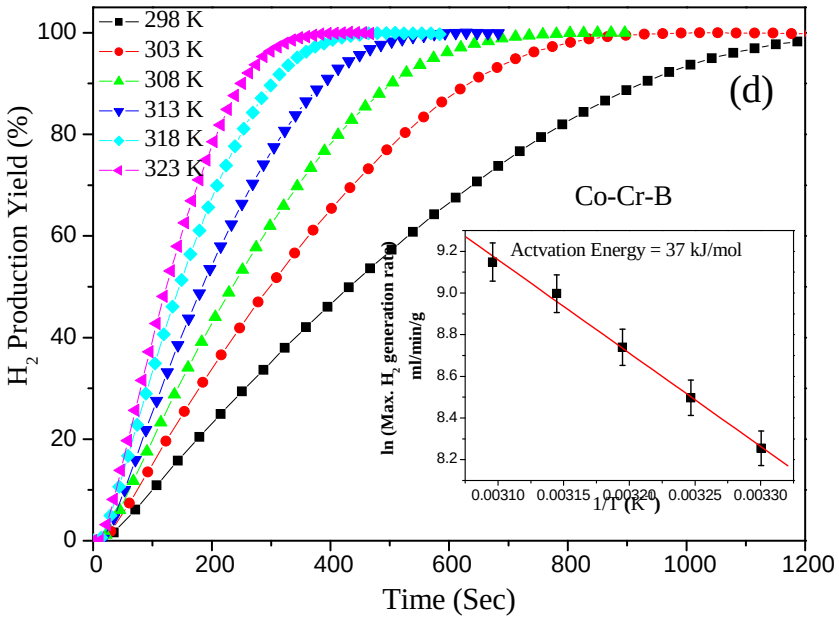

Figure 4.16 – Hydrogen generation yield as a function of reaction time by hydrolysis of alkaline $NaBH_4$ (0.025 M) solution measured at different solution temperatures with Co-Cr-B ($\chi_{Cr} = 4\%$) powder catalysts. Inset shows the Arrhenius plot of the H_2 generation rates.

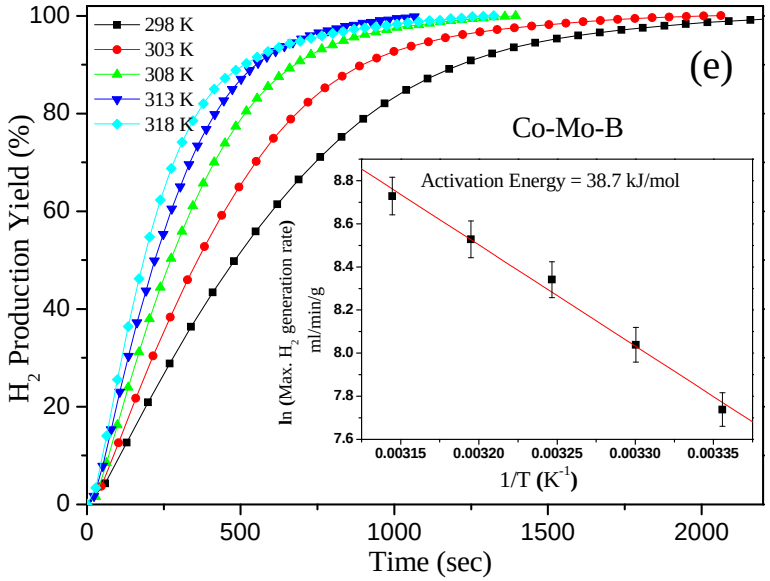

Figure 4.17 – Hydrogen generation yield as a function of reaction time by hydrolysis of alkaline $NaBH_4$ (0.025 M) solution measured at different solution temperatures with Co-Mo-B ($\chi_{Mo} = 35\%$) powder catalysts. Inset shows the Arrhenius plot of the H_2 generation rates.

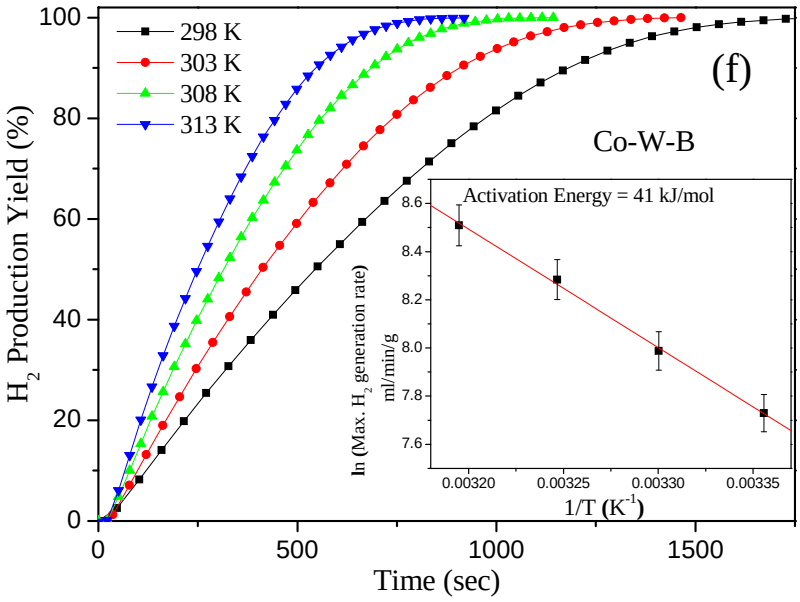

Figure 4.18 – Hydrogen generation yield as a function of reaction time by hydrolysis of alkaline $NaBH4$ (0.025 M) solution measured at different solution temperatures with Co-W-B ($\chi_W = 35\%$) powder catalysts. Inset shows the Arrhenius plot of the H_2 generation rates.

4.4 Effect of $NaBH_4$ and $NaOH$ concentration.

The effect of $NaBH_4$ concentration on the hydrogen generation rate was studied for Co-Cr-B catalyst by performing a series of experiments using several concentrations of $NaBH_4$ while keeping catalyst and NaOH concentration constant. Fig. 4.19 presents the plot of hydrogen generated volume, as a function of time, obtained from hydrolysis of alkaline $NaBH_4$ solution by using four different $NaBH_4$ concentrations, namely: 0.05, 0.75, 0.10, and 0.15 M in the starting solution. The concentration of NaOH and Co-Cr-B catalyst ($\chi_{Cr} = 4\%$) was kept constant at 0.1 M and 15 mg, respectively, during the hydrolysis reaction. The figure clearly shows no significant changes in the hydrogen generation rate with the increase of the $NaBH_4$ concentration. Inset of Fig. 4.19 shows ln(R_{max}) vs ln(concentration of $NaBH_4$).

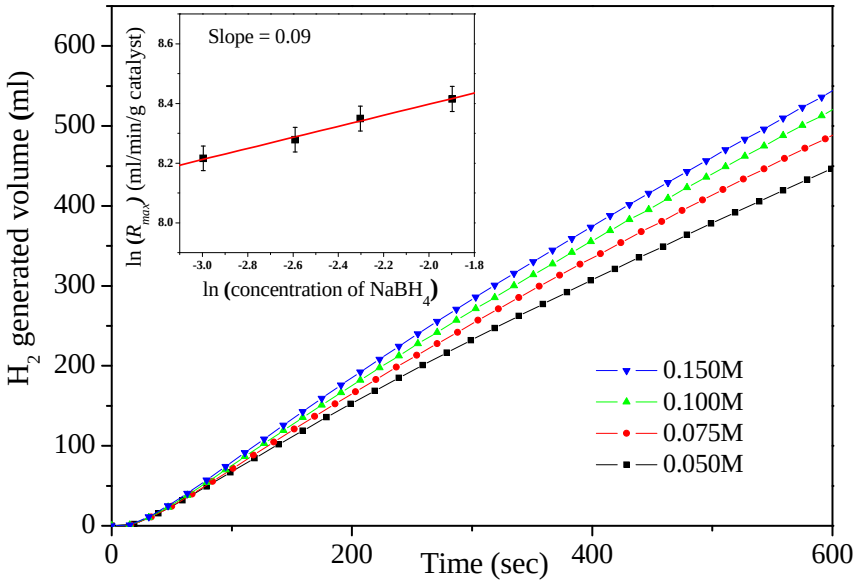

Figure 4.19 – Hydrogen generated volume as a function of reaction time with Co-Cr-B ($\chi_{Cr} = 4\%$) catalyst obtained by hydrolysis of alkaline $NaBH_4$ solution with four different concentrations of $NaBH_4$ ranging from 0.05 to 0.15 M. Inset shows the plot of ln(H_2 generation rate) vs ln(concentration of $NaBH_4$) to determine the reaction order with respect to $NaBH_4$.

The experimental points were fitted with a line having a slope of 0.09: the near-zero value of the slope indicates the zero order kinetics of the reaction with respect to the $NaBH_4$ concentration. The zero order of the reaction is explained on the basis that the initial hydride/catalyst molar ratio used for the measurement is high leading to BH_4 induced dynamic saturation of the active sites on the catalyst [99]. Similar zero order kinetics was proposed by Amendola et al. [110] (Ru catalyst), Kojima et al. [47] ($Pt - LiCoO_2$), and Ozkar et al. [52] (Ru nanoclusters) for reactions

with high $NaBH_4$ concentration. The hydrolysis reaction of $NaBH_4$ in water, without any catalyst, is suppressed by controlling the pH of the reaction solution; therefore, it is important to investigate the effect of NaOH concentration on the hydrolysis reaction. This was carried out by measuring the volume of the generated H_2 from hydrolysis of alkaline $NaBH_4$ using only Co-Cr-B catalyst by using 5 different NaOH concentrations, namely: 0.25, 0.50, 1.00, 1.85, and 2.50 M in the starting solution. The results are reported in Fig. 4.20. The concentration of $NaBH_4$ and Co-Cr-B catalyst ($\chi_{Cr} = 4$) was kept constant at 0.25 M and 15 mg respectively, during the hydrolysis reaction. By increasing the NaOH content from 0.25 to 2.5 M, no change is observed in the hydrogen generation rate (R_{max}): this proves the zero order reaction, with respect to NaOH concentration. This behavior can be explained in terms of $NaBH_4$ hydrolysis reaction mechanism, mentioned above, with the Co-Cr-B catalyst. The reaction between the boron species (BH_3^-, $BH_2(OH)^-$, and $BH(OH)_2^-$) and OH^- ions is catalyzed by absorption of OH^- ions on the Cr^{3+} surface species present in small amount. Thus a low initial concentration of OH^- ions is enough to dynamically cover these $Cr3^+$ species and, as the reaction proceeds, the OH^- ions are provided by breaking of H_2O molecules. This explains the constant hydrogen generation rate at higher NaOH concentration.

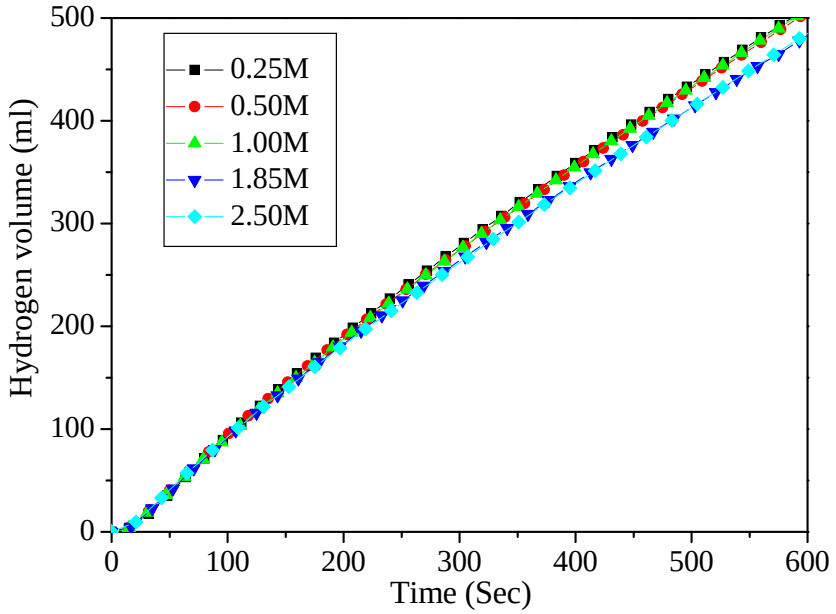

Figure 4.20 – Hydrogen generated volume as a function of reaction time with Co-Cr-B ($\chi_{Cr} = 4\%$) catalyst obtained by hydrolysis of alkaline $NaBH_4$ (0.25 M) solution with five different concentrations of NaOH ranging from 0.25 to 2.5 M. It is noticed that there is no relevant changes on generated hydrogen volume by changing the NaOH concentration.

4.5 Endurance test

For the catalyst to be commercially used, the catalyst need to be stable and not deteriorate with time and use. The catalyst need to be studied thoroughly under various conditions. For these reasons, four of the best catalysts were chosen, i.e. (Co-Cu-B($\chi_{Cu} = 35\%$), Co-Cr-B($\chi_{Cr} = 4\%$), Co-Mo-B($\chi_{Mo} = 5\%$), and Co-W-B($\chi_W = 5\%$)) and tested their behavior under various condition. We study the effect of high temperature treatment, durability and repeatability on these catalysts.

4.5.1 Effect of temperature on metal doped Co-B powder catalyst

Since the hydrolysis of $NaBH_4$ is highly exothermic with heat of reaction of ca. $210\,kJ/mol$, the reactor temperature often increases over 100^{o}C, especially when the reactor is operated in a continuous flow mode. Considering that catalyst in the hydrolysis of $NaBH_4$ is exposed to a hot caustic environment, catalyst high temperature durability is crucial for practical application. To study the effect of structural modification on catalytic activity, powders were heat-treated in Ar atmosphere at different temperatures upto 873 K for $2h$. The hydrogen generation yield, as a function of time, were obtained by hydrolysis of alkaline $NaBH_4$ (0.025 M) solution using these heat treated powders. The changes in the catalytic activity are discussed on based on XRD and SEM analysis.

Co-Cu-B

The hydrogen generation yield, as a function of time, obtained by hydrolysis of alkaline $NaBH_4$ (0.025 M) solution using these heat treated Co-Cu-B powders ($15\,mg$) are reported in Fig. 4.21 There was no change in the catalytic activity of the Co-Cu-B powder after heat treatment at 673 K as compared to the untreated powder. On the contrary, the heat treated sample at 773 K and 873 K shows a decrease in the H_2 generation rate, in any case, it is able to reach the 100% H_2 yield. This decrease in the catalytic activity might be due to the structural variation or particle agglomeration caused by heat treatment at 773 K. XRD pattern (Fig. 4.22) of the catalyst powder shows amorphous nature for both untreated Co-Cu-B powder and heat-treated sample at 673 K in Ar atmosphere. However, heat-treatment at 773 K in Ar atmosphere for $2h$ causes partial crystallization of the powder as indicated by the presence of weak reflections of Co and Cu peaks at in the XRD pattern. These peaks become more prominent at 873 K. Thus after heat treatment at 773 K and 873 K the amorphous

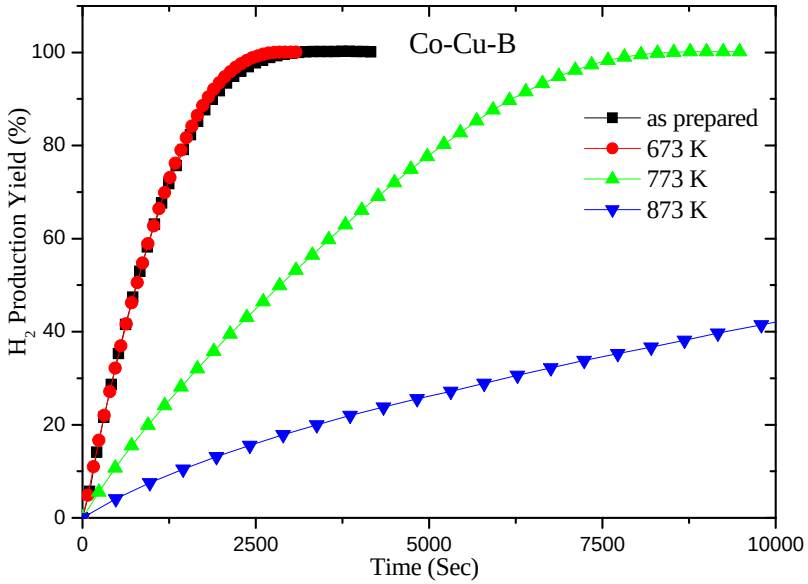

Figure 4.21 – Hydrogen generation yield as a function of reaction time obtained by hydrolysis of alkaline $NaBH_4$ (0.025 M) solution with Co-Cu-B catalyst powders untreated and heat-treated in Ar atmosphere at 673, 773, and 873 K for $2h$.

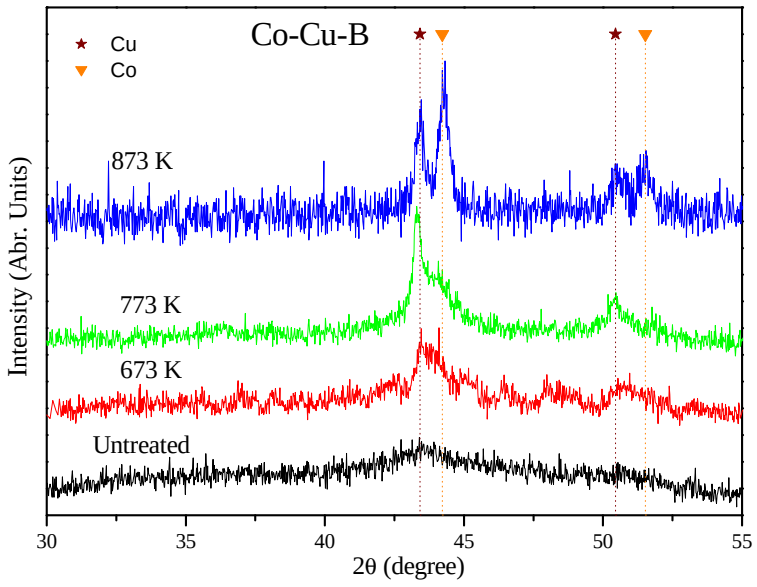

Figure 4.22 – XRD pattern of Co-Cu-B catalyst powder untreated and heat-treated in Ar atmosphere at 673, 773, and 873 K for $2h$.

Co-Cu-B powder starts to partially decompose into crystalline Co metal phase. The catalytic activity begins to drop, as Co metal can exhibit catalytic activity only when alloyed with metalloid atoms such as B [78]. SEM images (Fig. 4.23) clearly show

similar particle like surface morphology for the untreated Co-Cu-B powder and heat-treated sample at 673 K in Ar atmosphere. However at 773 K and 873 K, particle agglomeration can be observed, reducing the surface area and adding to the deterioration of the catalyst.

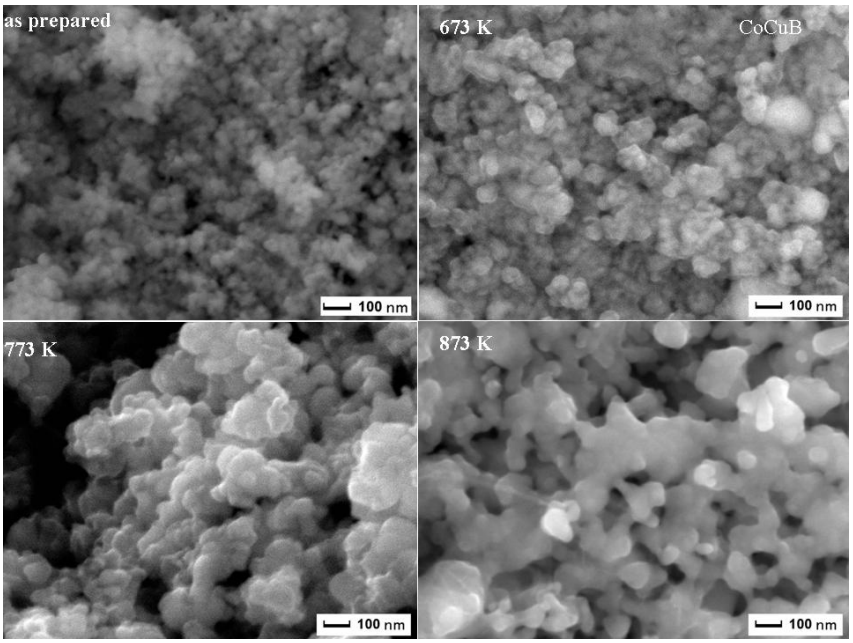

Figure 4.23 – SEM micrographs of: (a) untreated Co-Cu-B catalyst powder and heat-treated (b) at 673 K, (c) 773 K and (d) at 873 K in Ar atmosphere for $2h$.

Co-W-B

The hydrogen generation yield, as a function of time, obtained by hydrolysis of alkaline $NaBH_4$ (0.025 M) solution using heat treated Co-W-B powders ($15\,mg$) are reported in Fig. 4.24. There was no change in the catalytic activity of the Co-W-B powder after heat treatment at 673 K as compared to the untreated powder, while at 773 K there is slight drop in the catalytic activity. At 873 K, catalytic activity drops further as the amorphous Co-W-B powder decomposes into crystalline Co metal phase as seen in XRD pattern (Fig. 4.25), in any case, it is able to reach the 100% H_2 yield. SEM images (Fig. 4.26) clearly show similar particle like surface morphology for the untreated Co-W-B powder and heat-treated sample at 673 K in Ar atmosphere. At 773 K the Co-Cu-B particle just begins to agglomerate, while at 873 K the agglomeration can be clearly seen in the SEM image resulting in deterioration of the catalytic activity.

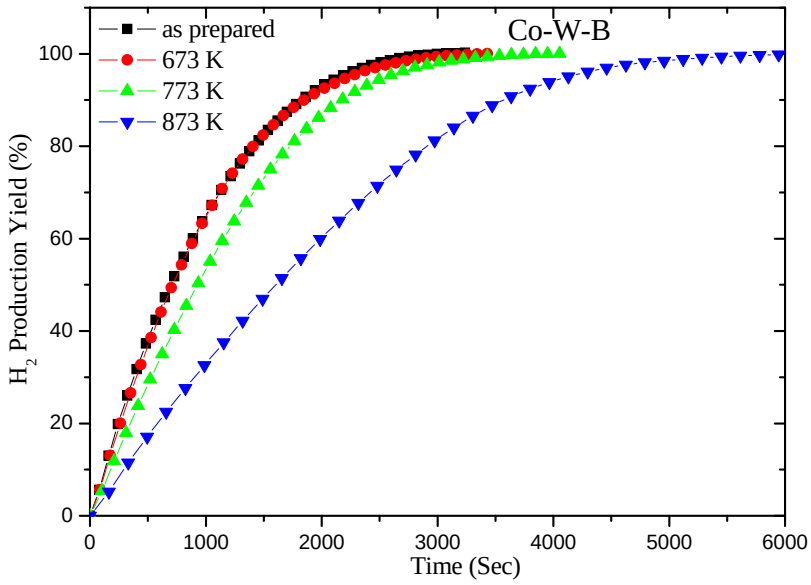

Figure 4.24 – Hydrogen generation yield as a function of reaction time obtained by hydrolysis of alkaline $NaBH_4$ (0.025 M) solution with Co-W-B catalyst powders untreated and heat-treated in Ar atmosphere at 673, 773, and 873 K for $2h$.

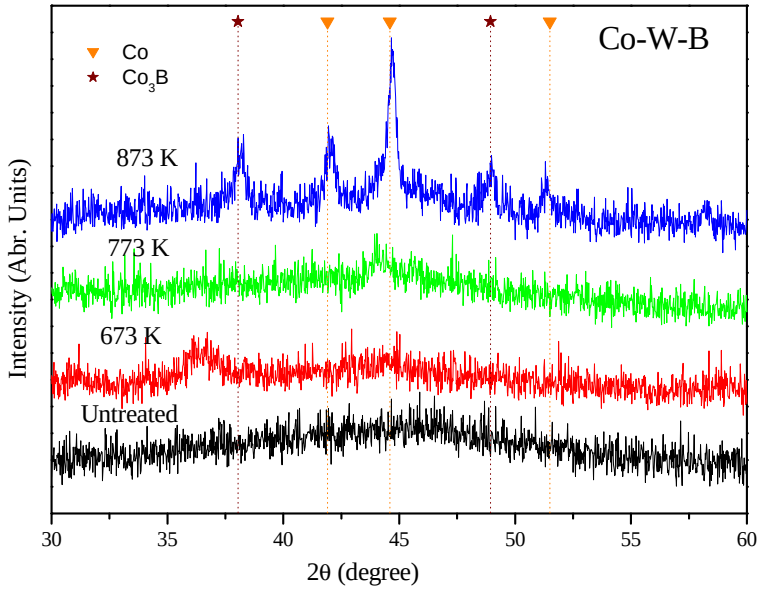

Figure 4.25 – XRD pattern of Co-W-B catalyst powder untreated and heat-treated in Ar atmosphere at 673, 773, and 873 K for $2h$.

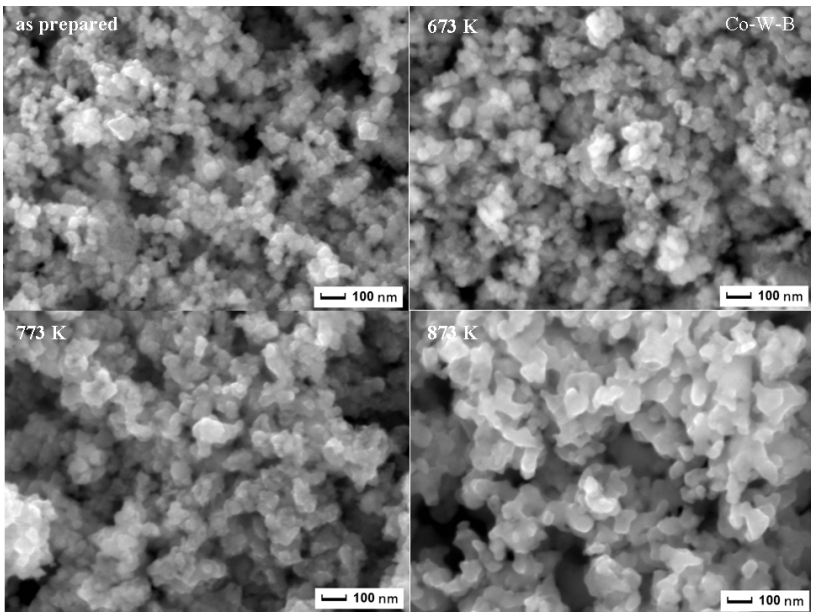

Figure 4.26 – SEM micrographs of: (a) untreated Co-W-B catalyst powder and heat-treated (b) at 673 K, (c) 773 K and (d) at 873 K in Ar atmosphere for $2h$.

Co-Mo-B

The hydrogen generation yield, as a function of time, obtained by hydrolysis of alkaline $NaBH_4$ (0.025 M) solution using heat treated Co-W-B powders ($15\,mg$) are reported in Fig. 4.27. There was hardly any change visible in the catalytic activity of the Co-W-B powder after heat treatment at 673 K and 773 K as compared to the untreated powder. Even after heat treatment at 773 K, the catalyst powder is still in particle form and there is not much sign of agglomeration, as seen in the SEM images (Fig. 4.29). The XRD pattern (Fig. 4.28) also shows no signs of crystallization. At 873 K, peaks of metal Co and Co-oxide are clearly visible in the XRD pattern. The Hydrogen generation rates drops, but is able to reach the 100% H_2 yield. Co-Mo-B powder can maintain its catalytic efficiency even at 873 K, thus this shows that the Co-MoB catalyst is stable and can be useful for high temperature application. The presence of Mo could be responsible for preserved catalytic effect even after annealing of the Co-Mo-B powder at 773 K. Further investigation is required to confirm and better understand the role of Mo.

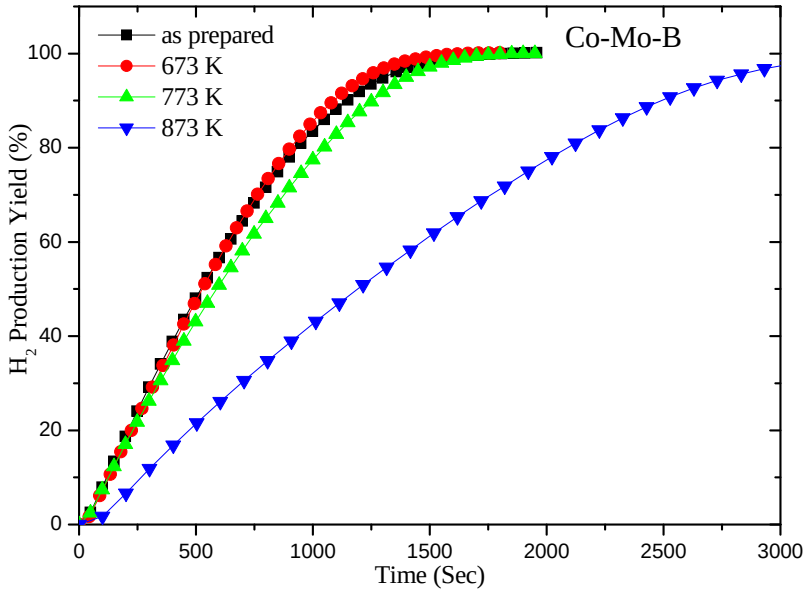

Figure 4.27 – Hydrogen generation yield as a function of reaction time obtained by hydrolysis of alkaline $NaBH_4$ (0.025 M) solution with Co-Mo-B catalyst powders untreated and heat-treated in Ar atmosphere at 673, 773, and 873 K for $2h$.

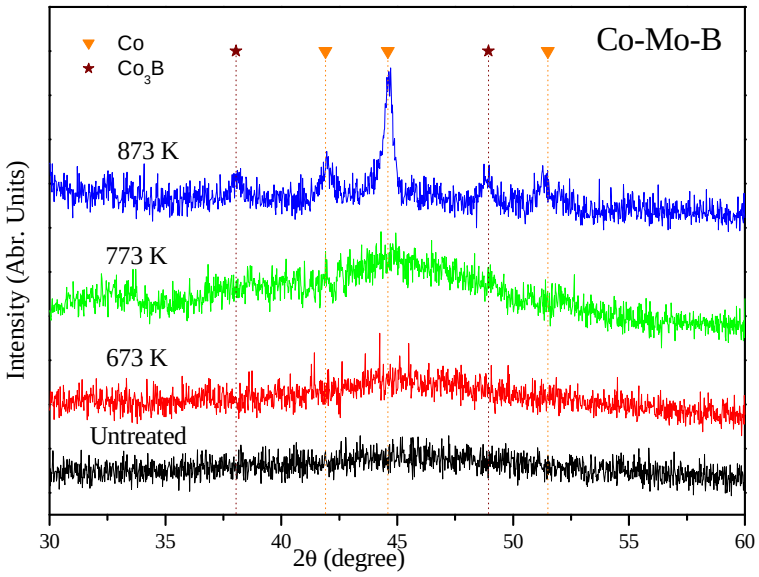

Figure 4.28 – XRD pattern of Co-Mo-B catalyst powder untreated and heat-treated in Ar atmosphere at 673, 773, and 873 K for $2h$.

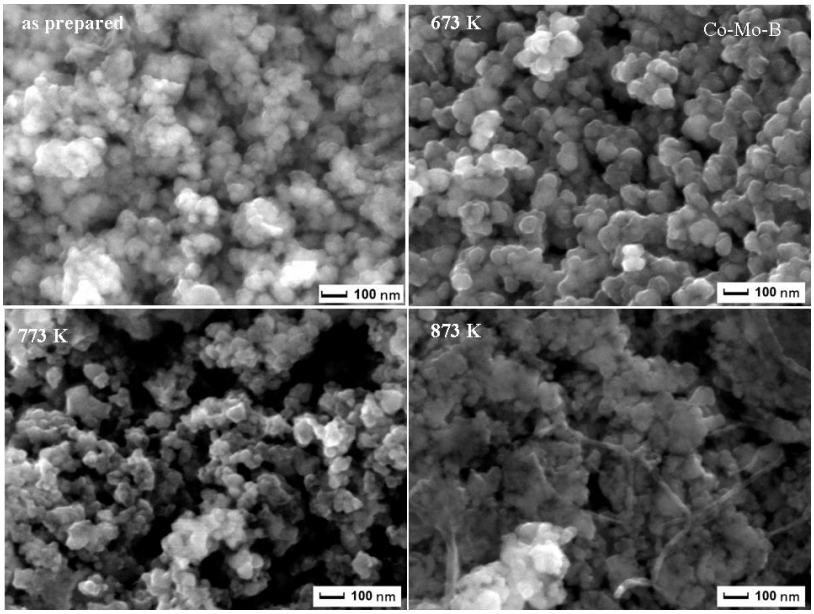

Figure 4.29 – SEM micrographs of: (a) untreated Co-Mo-B catalyst powder and heat-treated (b) at 673 K, (c) 773 K and (d) at 873 K in Ar atmosphere for $2h$.

Co-Cr-B

The hydrogen generation yield, as a function of time, obtained by hydrolysis of alkaline $NaBH_4$ (0.025 M) solution using heat treated Co-Cr-B powders (15 mg) are reported in Fig. 4.30 There was no change in the catalytic activity of the Co-Cr-B powder after heat treatment at 573K (figure not shown) as compared to the untreated powder, while at 673 K there is slight drop in the catalytic activity. At 773 K and 873 K the catalytic activity drops further as the amorphous Co-Cr-B powder decomposes into crystalline Co metal phase as seen in XRD pattern (Fig. 4.31), in any case, it is able to reach the 100% H_2 yield. SEM images (Fig. 4.32) clearly show particle agglomeration for heat-treated samples. The particle like morphology is completely lost when heat treated at 873 K.

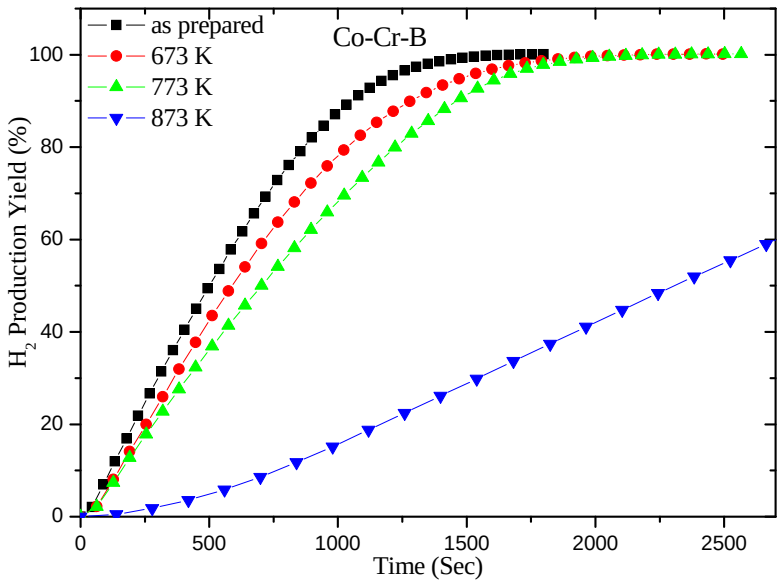

Figure 4.30 – Hydrogen generation yield as a function of reaction time obtained by hydrolysis of alkaline $NaBH_4$ (0.025 M) solution with Co-Cr-B catalyst powders untreated and heat-treated in Ar atmosphere at 673, 773, and 873 K for $2h$.

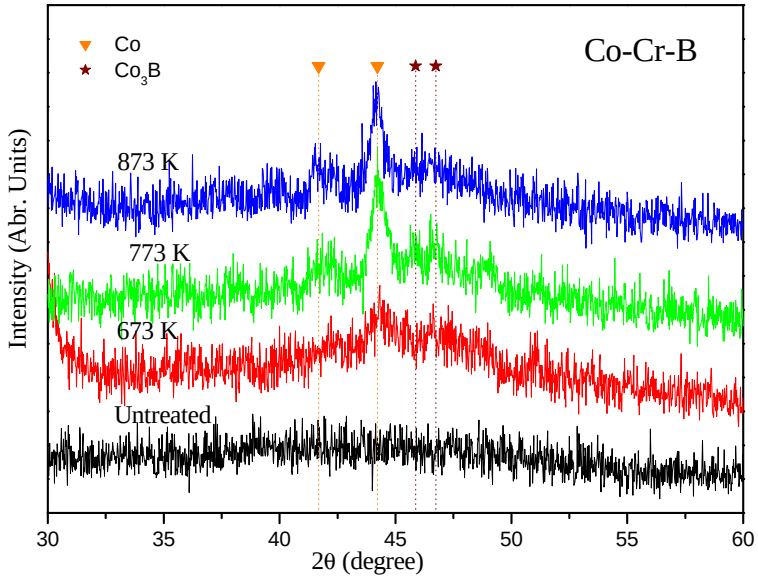

Figure 4.31 – XRD pattern of Co-Cr-B catalyst powder untreated and heat-treated in Ar atmosphere at 673, 773, and 873 K for $2h$.

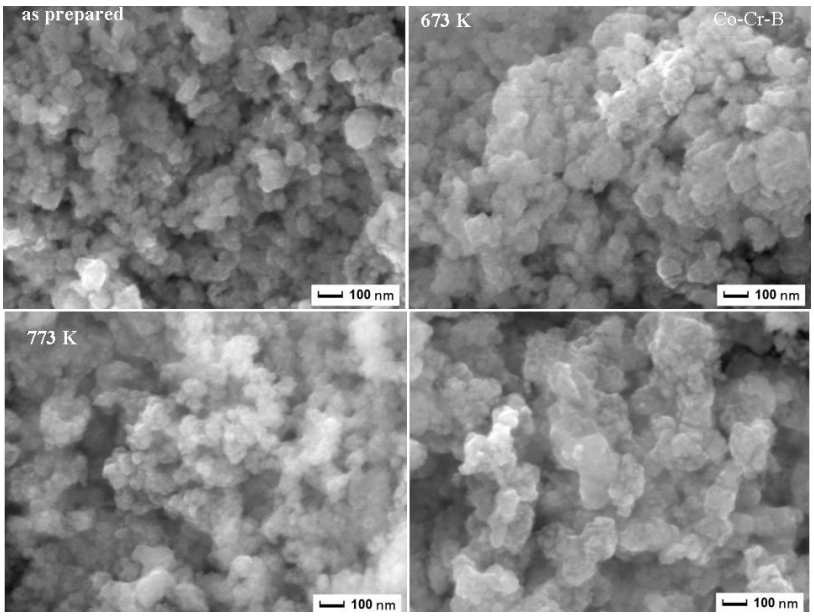

Figure 4.32 – SEM micrographs of: (a) untreated Co-Cr-B catalyst powder and heat-treated (b) at 673 K, (c) 773 K and (d) at 873 K in Ar atmosphere for $2h$.

4.5.2 Durability of metal doped Co-B powder catalysts

One of the major difficulties for the development of the Borohydride- PEMFC is the catalyst tolerance to deactivation [111]. In application field, the catalyst generally remains exposed to the ambient atmosphere and deactivation may intervene. To investigate the effect of ambient atmosphere on the catalytic properties, four powders were chosen, i.e. (Co-Cu-B($\chi_{Cu} = 35\%$), Co-Cr-B($\chi_{Cr} = 4\%$), Co-Mo-B($\chi_{Mo} = 5\%$), and Co-W-B($\chi_{W} = 5\%$)) The catalyst powders were exposed to the ambient condition and were tested at an interval of 7 days for catalytic hydrolysis of alkaline $NaBH_4$ solution (0.025 M) (Figs 4.33 - Fig 4.36). The exposure of these catalysts to the ambient condition even after 28 days does not cause much change in the case of Co-Cu-B and Co-W-B. A minor decrease in the reaction rate is observed in case of Co-Mo-B and Co-Cr-B, as compared to the fresh powder, however, the expected hydrogen yield is produced. This reduction in efficiency might be due to the formation of an oxide layer on the surface of the catalyst during exposure to the ambient atmosphere [83]. Further exposure of the catalyst does not cause much change in R_{max} and each time 100% hydrogen yield is obtained. This study shows that our catalysts are quite stable against deactivation from exposure to ambient atmosphere.

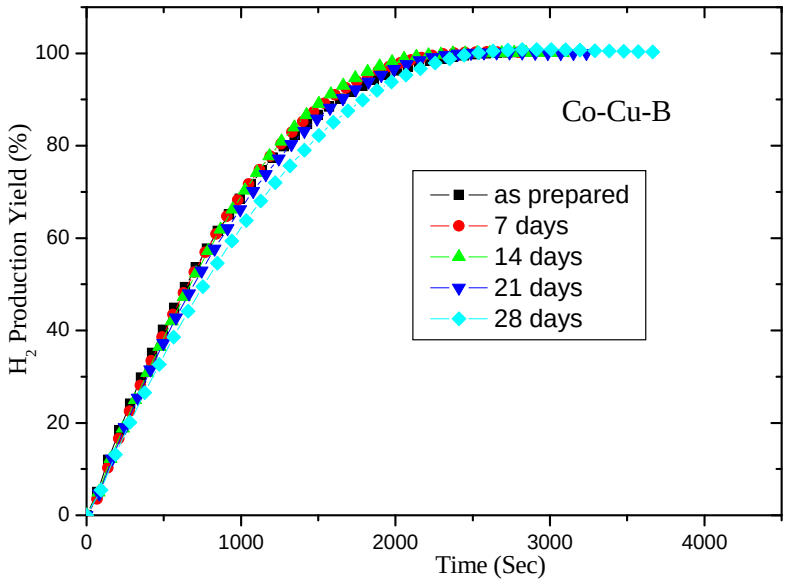

Figure 4.33 – Hydrogen generation yield as a function of reaction time obtained by hydrolysis of alkaline $NaBH_4$ (0.025 M) solution with Co-Cu-B catalyst exposed to ambient atmosphere with time intervals.

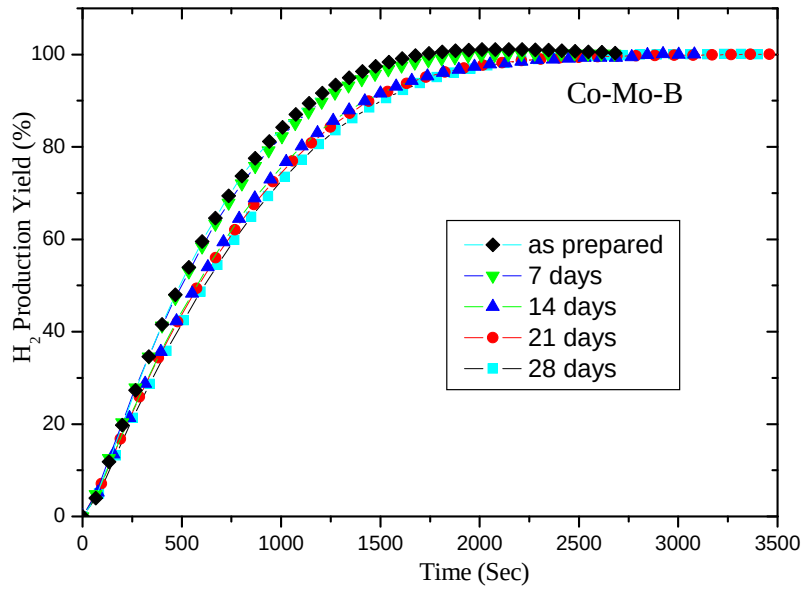

Figure 4.34 – Hydrogen generation yield as a function of reaction time obtained by hydrolysis of alkaline $NaBH_4$ (0.025 M) solution with Co-Mo-B catalyst exposed to ambient atmosphere with time intervals.

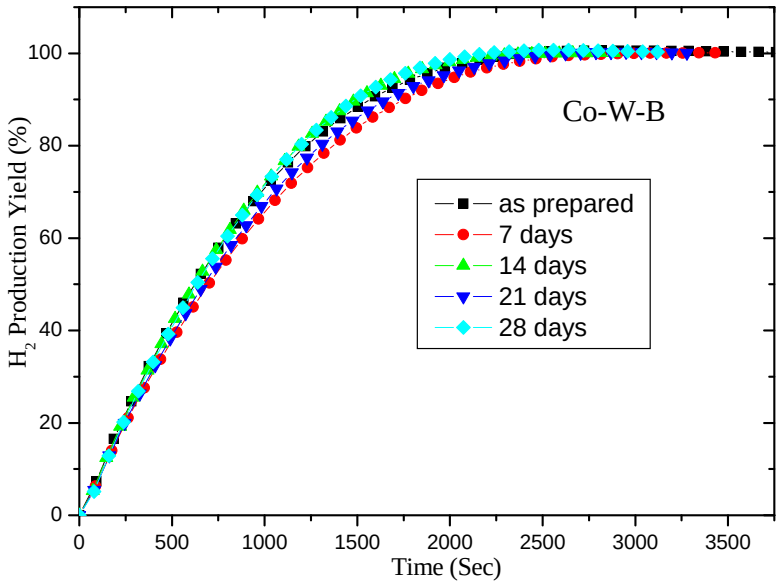

Figure 4.35 – Hydrogen generation yield as a function of reaction time obtained by hydrolysis of alkaline $NaBH_4$ ($0.025M$) solution with Co-W-B catalyst exposed to ambient atmosphere with time intervals.

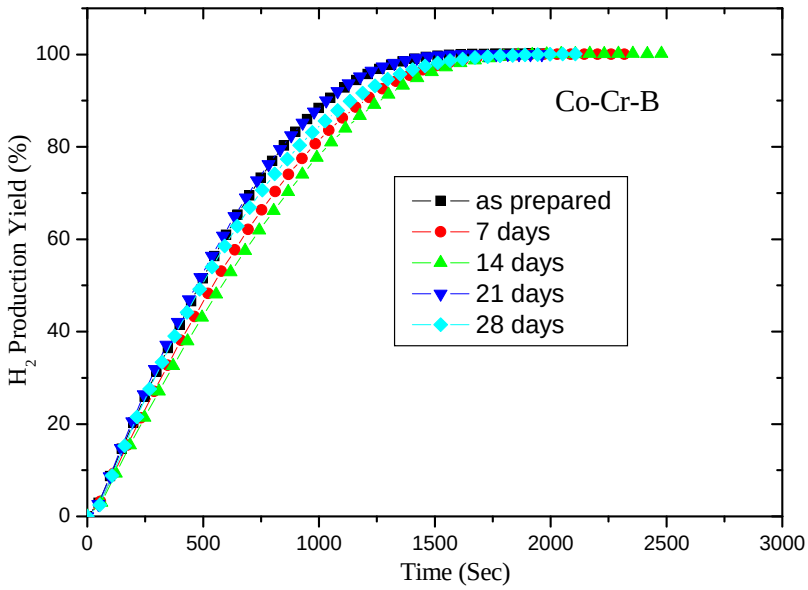

Figure 4.36 – Hydrogen generation yield as a function of reaction time obtained by hydrolysis of alkaline $NaBH_4$ (0.025 M) solution with Co-Cr-B catalyst exposed to ambient atmosphere with time intervals.

4.5.3 Repeatability of metal doped Co-B powder catalyst

A good catalyst must be able to completely hydrolyze alkaline solution of $NaBH_4$ even after being used number of times. For this reason a specific experiment was carried out to recycle the catalyst powder sample for a number of times as described in the following steps: (1) hydrolysis reaction course, (2) recollection of the powder, (3) washing with distilled water and ethanol before drying at around 323 K under continuous N_2 flow.

Hydrogen generation yield as a function of time was carried out for all the four catalyst (Co-Cu-B(χ_{Cu} = 35%), Co-Cr-B(χ_{Cr} = 4%), Co-Mo-B(χ_{Mo} = 5%), and Co-W-B(χ_W = 5%)) for 6 runs (Fig. 4.37 - Fig. 4.40) For all the catalyst, it can be clearly observed that after every run the R_{max} decreases, but each time the catalyst is able to produce 100% hydrogen yield. The small decrease in efficiency may be due to partial inactivation caused on the surface of the catalyst by the $NaBO_2$ formation during the reaction.

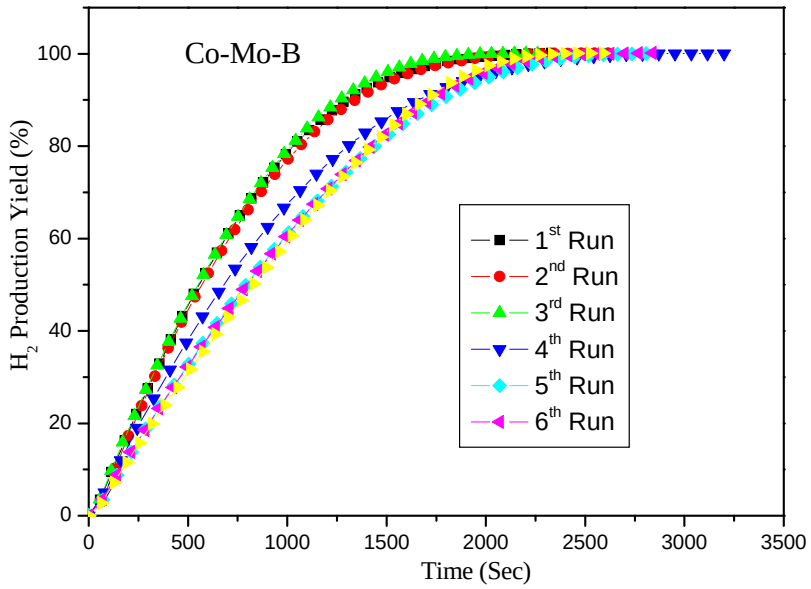

Figure 4.37 – Cyclic behavior of Co-Mo-B catalyst powder on hydrogen generation yield as a function of reaction time measured using hydrolysis of 0.025 M $NaBH_4$ alkaline solution.

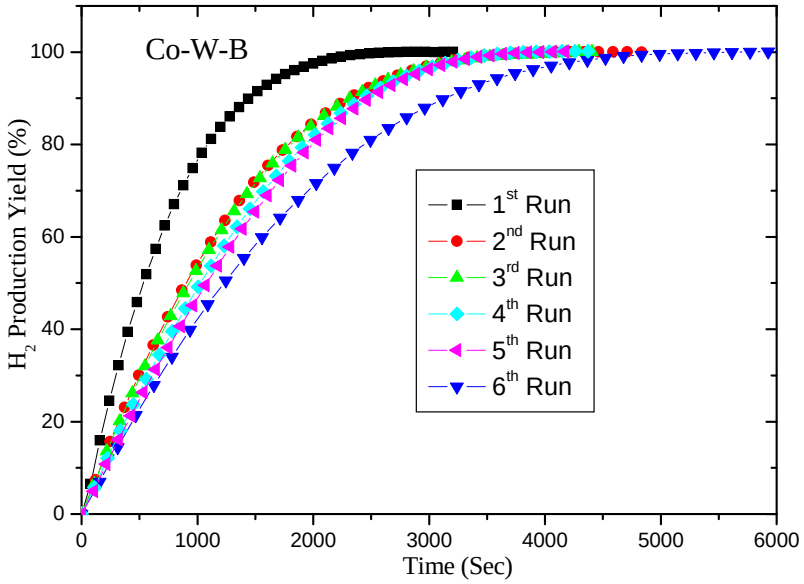

Figure 4.38 – Cyclic behavior of Co-W-B catalyst powder on hydrogen generation yield as a function of reaction time measured using hydrolysis of 0.025 M $NaBH_4$ alkaline solution.

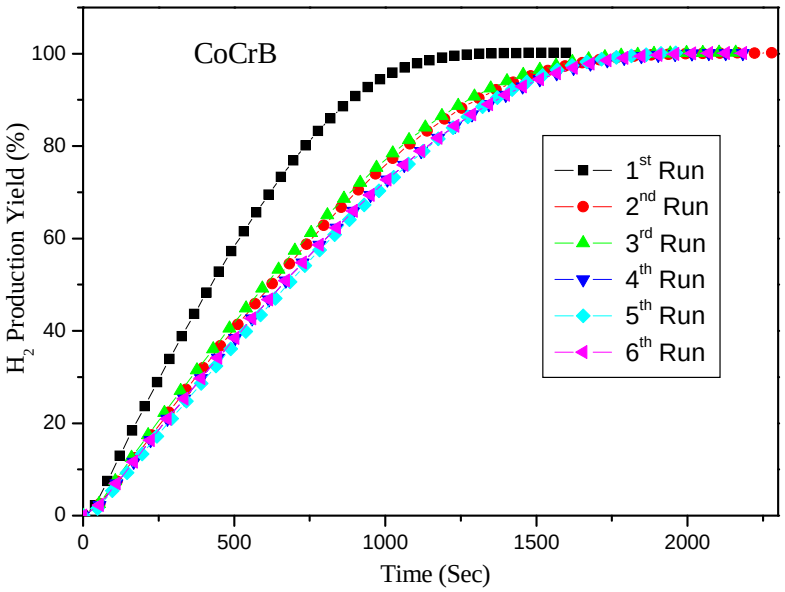

Figure 4.39 – Cyclic behavior of Co-Cr-B catalyst powder on hydrogen generation yield as a function of reaction time measured using hydrolysis of 0.025M $NaBH_4$ alkaline solution.

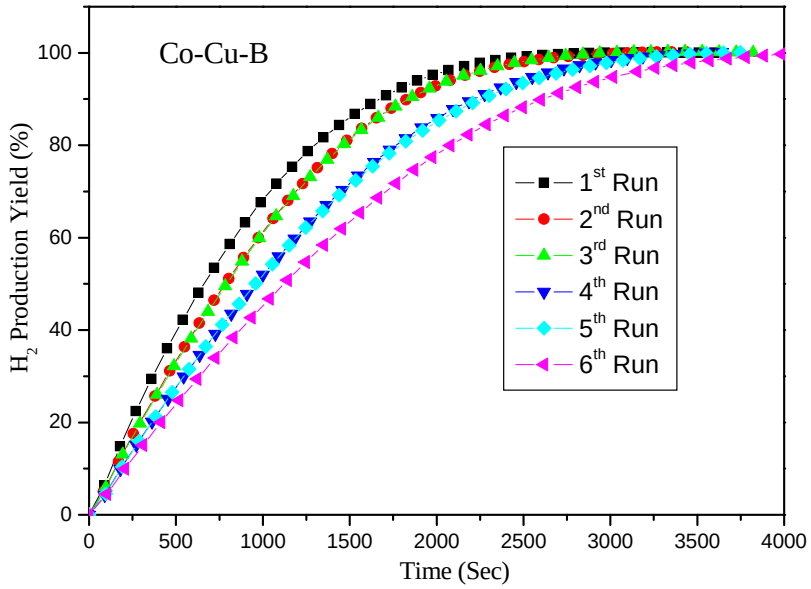

Figure 4.40 – Cyclic behavior of Co-Cu-B catalyst powder on hydrogen generation yield as a function of reaction time measured using hydrolysis of 0.025 M $NaBH_4$ alkaline solution.

4.6 Conclusion

We have investigated the role of the dopant transition metals: Ni, Fe, Cu, Cr, Mo, and W on the catalytic efficiency of the Co-B powder for H_2 generation by hydrolysis of $NaBH_4$. Transition metals added to the Co-B catalyst behave in a different way while influencing the catalytic activity. Cr, W, Mo, and Cu impose significant catalytic effects on the H_2 generation rate by increasing about $3-4$ times, as compared to Co-B catalyst. On the contrary, Ni and Fe cause only marginal increment in the catalytic performance of the Co-B catalyst. The $\frac{Metal}{Co+Metal}$ molar ratio was varied in order to study the effect of each metal dopant concentration on the catalytic efficiency. The best promoting effects were obtained with specific molar concentration of the transition metals. The promoting effects of the dopants are related to: (1) large active surface area of the catalysts (Co-Fe-B, Co-Cu-B, Co-Cr-B, Co-Mo-B, Co-W-B), (2) ability to act as Lewis acid sites for better absorption of OH groups (Co-Cr-B, Co-Mo-B, Co-W-B), (3) electronic interaction with Co active metal (Co-Ni-B, Co-Fe-B), and (4) amorphous nature of the alloy catalyst (all investigated catalysts). Finally, all the activation energies involved in the catalytic hydrolysis of $NaBH_4$ are comparable to the lowest values of the reported literature catalysts. Stability, reusability, and durability for Co-Cu-B, Co- Cr-B, Co-Mo-B, Co-W-B catalyst were

investigated and found relevant for applications such as on-board hydrogen generation method for portable PEM fuel cells.

Chapter 5

Film catalyst for hydrolysis of alkaline $NaBH_4$

"Every block of stone has a statue inside it
and it is the task of the sculptor to discover it.
I saw the angel in the marble and carved until I set him free."
-Michelangelo

A Proton-Exchange-Membrane Fuel Cell (PEMFC) is a system which uses an on-site H_2 generated via $NaBH_4$ hydrolysis reaction in the reactor directly connected with the PEMFC. However, the two main challenges in borohydride based PEMFC are: 1) the synthesis of low cost catalyst material which provide high reaction conversion and H_2 generation rate, and 2) the development of an efficient and compact reactor to connect the H_2 supply to the PEMFC [96, 112]. The former hurdle was almost overcome in the recent literatures [46, 52, 98] with synthesis of efficient and durable catalysts for hydrolysis of $NaBH_4$ solution. The later can be addressed by designing compact hydrolysis reactor with controllable continuous flow system, fixed catalyst bed, easy refuelling system of the fresh $NaBH_4$ solution, effortless separation of the by-product, and trouble free path for the H_2 to PEMFC.

However, catalysts in the form of very fine powders have been mainly used in previous studies to investigate the catalytic activity, which are not applicable for continuous-flow fixed bed reactor system because of the following points : (1) the separation of the catalyst from the suspension after the reaction could be difficult, (2) the suspended particles tend to aggregate, especially when they are present at high concentrations, (3) the particulate suspensions can block the openings of the reactor in continuous-flow systems. These problems can be solved by synthesizing the catalyst in the form of thin films either coated on the inner wall of the reactor

bed or supported on some substrate like Ni-foam through which the $NaBH_4$ solution can be poured. Catalysts in the form of thin films are also beneficial to the reactor because they can easily be recovered and reused, which means that they are suitable as an on/off switch for the generation of H_2.

Thin film catalyst also has extra degrees of freedom to change the surface morphology and structure to gain efficiency [108]. Ni-foam certainly offers a better option as catalyst support because of its high porosity and initial surface area. Thus catalyst supported on Ni-foam seems the better choice for fixed catalyst bed in continuous-flow system where $NaBH_4$ solution is allowed to pass through the large pores of the Ni foam by producing H_2 when coming in contact with catalyst surface.

5.1 Co-B-P film catalyst

In Chapter 3, we have analyzed Co-B, Co-P, and Co-P-B catalyst powders for hydrogen generation by catalytic hydrolysis of $NaBH_4$. We found that ternary alloy catalyst in the form of Co-P-B was able to produce hydrogen with much higher rate as compared to the binary alloy Co-P and Co-B. This enhancement was explained on the basis of synergic effects caused by P and B atoms in the Co-P-B catalyst where, as revealed by X-Photoelectron-Spectroscopy analysis, the role of P is to create high number of Co active sites on the surface while B provides the necessary electron density to Co thus enhancing its catalytic activity [78, 113]. However, in powder catalyst there is an intrinsic low active area due to atomic agglomeration. In addition, problems related to powder recovering, after or during the reaction, restrict such a kind of catalysts for the applications. To solve these problems it is necessary to synthesize the catalyst in the form of thin films deposited on support. Catalysts in form of thin film have a extra degrees of freedom to change the surface morphology and structure.

Co-P-B catalyst, in the form of thin films were synthesised both by Electroless Deposition (ED) and Pulsed Laser Deposition (PLD)[1] and compared their catalytic efficiency with Co-P-B powder catalysts. The catalytic activity of these three different forms of Co-P-B catalysts was compared by measuring the hydrogen generation yield as function of time by hydrolysis of alkaline $NaBH_4$ (0.025 M) solution at 298 K: results are reported in Fig. 5.1. The hydrogen production starts without any induction time and reaches 100% of the theoretical H_2 yield. The H_2 generation yield values reported in Fig. 5.1 were perfectly fitted by using a single exponential function[2].

[1] See Chapter 2 for more details on film prepration by ED and PLD

[2] See Appendix A

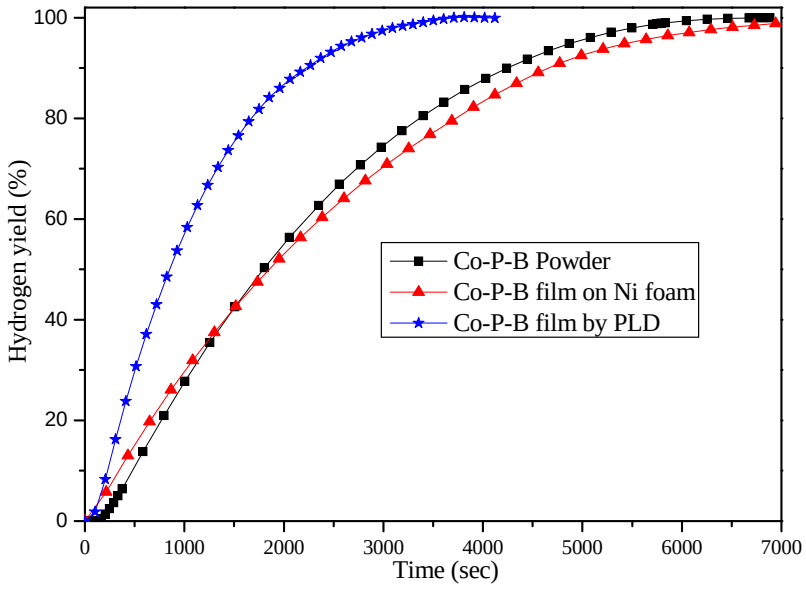

Figure 5.1 – Hydrogen generation yield as a function of reaction time obtained by hydrolysis of alkaline $NaBH_4$ (0.025 M) with Co-P-B powder and the corresponding films synthesized by ED and PLD.

The Co-P-B catalyst film deposited by PLD shows higher catalytic activity for hydrogen generation as compared to the same amount of Co-P-B catalyst powder and film deposited on Ni-foam by ED. Nearly similar value of maximum H_2 generation rate was obtained with chemically synthesized Co-P-B powder ($\sim 2010\, ml/min/g$ catalyst) and film on Ni-foam ($\sim 2090\, ml/min/g$ catalyst), while Co-P-B film synthesized by PLD ($\sim 4230\, ml/min/g$ catalyst) shows about 2 times higher R_{max}. Several films synthesized by using the same PLD parameters showed almost identical ($\pm 5\%$) H_2 generation rate: this proves the reproducibility of the PLD process. During the reaction process, the catalyst films maintain their stability both in connection to hydrogen production and bonding with substrate. In Fig. 5.2, we present SEM images of Co-P-B catalyst powder and films synthesized by both ED and PLD. The SEM images of catalyst powders show particle-like morphology with particles having spherical shape and average size of a few nanometers. During catalyst preparation, an efficient reducing agent in the form of $NaBH_4$ was used which is able to cause rapid reduction of Co ions that avoids particle growth above a few nanometers. However, due to the high surface energy related to these particles, they tend to agglomerate as observed in the SEM image (Fig. 5.2 a). Surface morphology of the Co-P-B film (Fig. 5.2 b) synthesized by ED on Ni-foam shows two-dimensional nano-flakes like structure with space separation of a few hundreds of nanometers. The surface of Ni-foam might act

as a nucleation site for the Co-P-B catalyst thus favouring the final observed peculiar structure. As seen in Fig. 5.2 c, Co-P-B catalyst films, prepared by PLD, exhibit a nanocluster assembled structure made of well dispersed spherical particles with size ranging between 50 and 200 nm. Such a cluster-assembled morphology can be explained on the basis of laser-induced phase explosion process. For a specific choice of the laser pulse parameters, especially the pulse energy density, in which the target material under the surface reaches temperature of $\sim 0.9T_c$ (thermodynamic critical temperature) causing a very high homogeneous nucleation of vapour bubble. In these conditions, the liquid makes a rapid transition from superheated liquid to a matrix of vapor and liquid droplets which leave the irradiated target surface and get deposited on the substrate [114, 115].

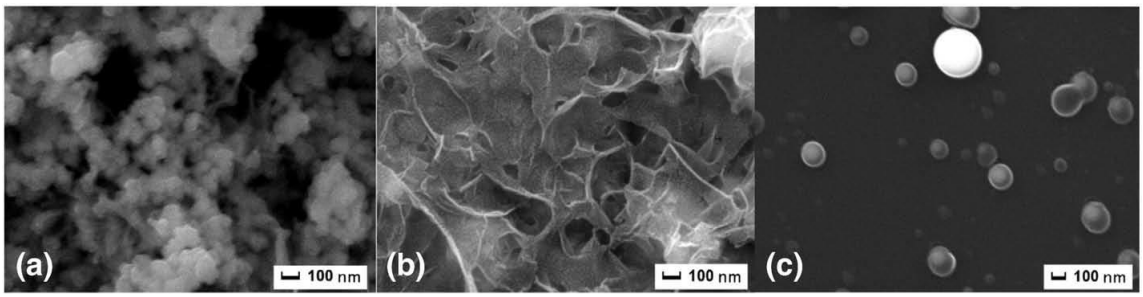

Figure 5.2 – SEM images of (a) Co-P-B powder and corresponding films synthesized by (b) ED and (c) PLD

The nanoparticles on film surface are thought to be highly active sites, for the hydrolysis reaction, which produce hydrogen immediately after coming in contact with the solution even at low concentration of $NaBH_4$ and room temperature. Despite the fact that the Co-P-B film synthesized by ED on Ni-foam exhibits activity for H_2 production similar to the powder, it however has the advantage of easy recovery during or after the reaction course. The easiness to prepare this kind of catalyst film makes it a potential candidate as a catalyst bed in continuous-flow type reactor. Co-P-B catalyst film synthesized by PLD on glass support shows much better activity for H_2 production and also with the advantage of catalyst recovery and reuse.

5.1.1 Co-B-P catalyst prepared on Ni-foam

The effect of Co-P-B loading on the catalytic activity was studied by synthesizing Ni-foam specimens covered with increasing number of Co-P-B catalyst layers using

ED. The hydrogen generation yield was measured as a function of time (Fig. 5.3) by hydrolysis of alkaline $NaBH_4$ (0.025 M) solution using Co-P-B catalyst films on Ni-foam with different number of layers. Inset of the (Fig. 5.3) shows the maximum H_2 generation rate (R_{max}) as a function of number of deposited layers on Ni-foam.

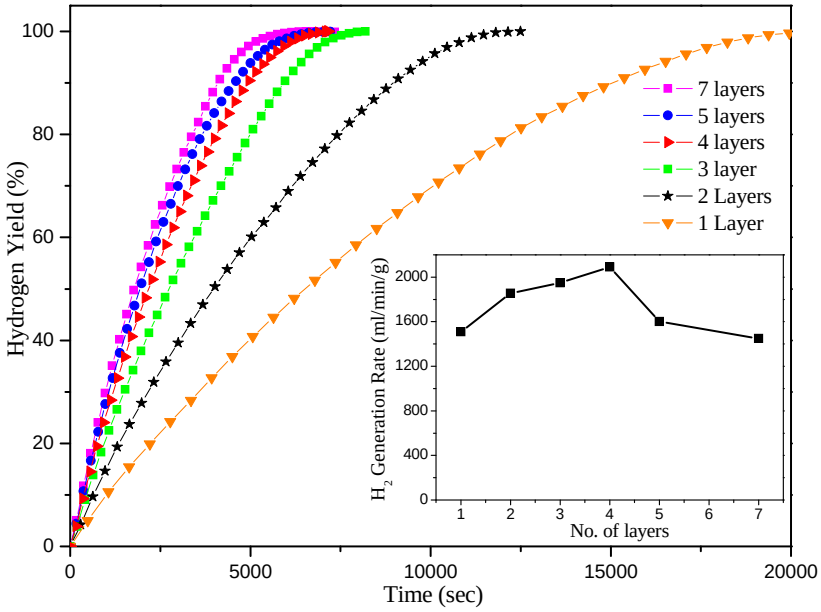

Figure 5.3 – Hydrogen generation yield as a function of reaction time obtained by hydrolysis of alkaline $NaBH_4$ (0.025 M) with different numbers of Co-P-B films synthesized by ED. Inset shows the maximum H_2 generation rate (R_{max}) obtained with Co-P-B catalyst films as a function of number of layers. Please note that 7-layers Co-P-B film takes less time to reach 100% H_2 yield but shows lower R_{max} value than 4 layers film as R_{max} is calculated per gram of catalyst.

The figure clearly shows that the H_2 generation rate increases with the number of layers and reaches the maximum value with 4 layers. With further increase of the layers number the R_{max} value decreases. In Fig. 5.4 we present SEM images of Ni-foam substrate, both uncoated (Fig. 5.4 a) and coated with single layer (Fig. 5.4 b), four layers (Fig. 5.4 c), and seven layers (Fig. 5.4 d). By looking at these images we may safely conclude that single layer is not sufficient to fully cover the surface of the Ni-foam while, on the other hand, 3 - 4 layers of Co-P-B film can completely cover the foam. However, by depositing more than 4 layers, only the weight of the catalyst film increases without much improvement of the catalytic efficiency. This implies that the R_{max} value decreases because H_2 generation rate is calculated per gram of catalyst. To gain further insight on the catalytic behaviour of the different number of Co-P-B layers deposited on Ni-foam, we have acquired SEM images (Fig. 5.5) at

higher magnification of one, four, and seven layers, respectively. Ni-foam coated with one (Fig. 5.5 a) and four layers (Fig. 5.5 b) show similar nano-flakes type morphology. However, with seven layers the morphology of the coated Ni-foam becomes like an agglomerated-particle structure which probably causes the decrease in the effective surface area of the Co-P-B catalyst. This is also the reason of the R_{max} decrease with layers number exceeding 4. The agglomeration phenomenon is most probably related to the minimization of the excess surface free energy which is growing with the number of the deposited layers.

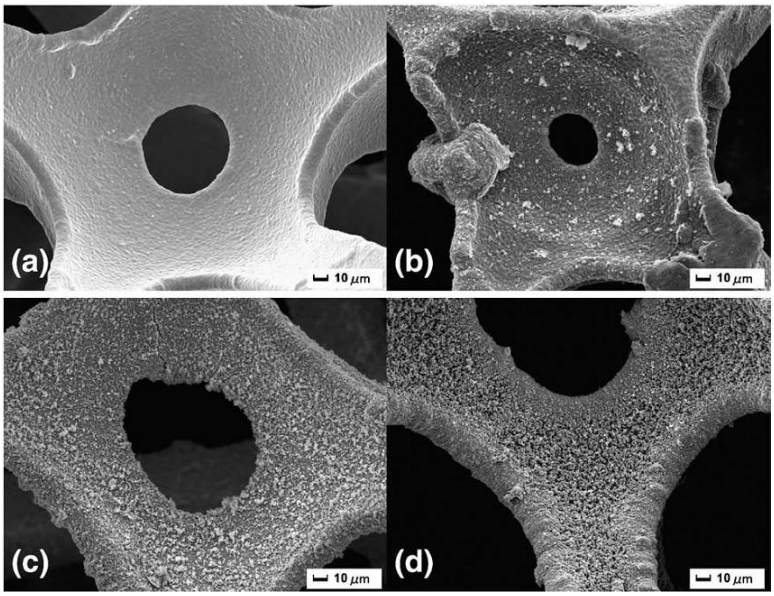

Figure 5.4 – Low magnification SEM images of Ni-foam: (a) uncovered, and covered by ED with Co-P-B film: (b) single layer, (c) four layers, and (d) seven layers.

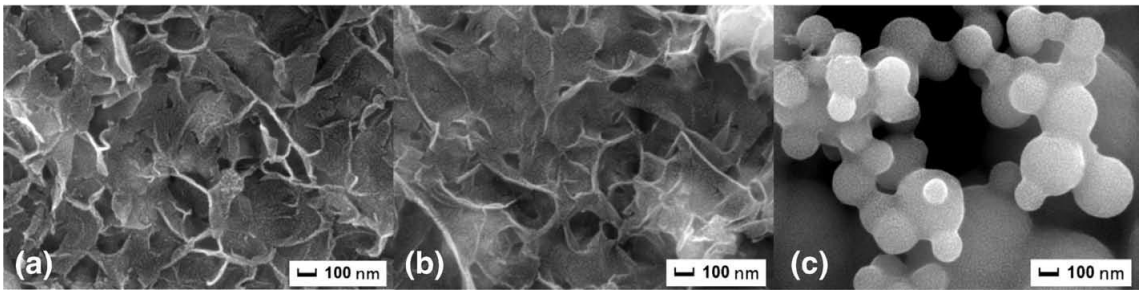

Figure 5.5 – High magnification SEM images of Co-P-B films deposited by ED on Ni-foam: (a) single layer, (b) four layers, and (c) seven layers.

5.1.2 Co-B-P film prepared by PLD

The role of nanoparticles in enhancing the catalytic activity is studied by synthesizing the Co-P-B films by using various laser energy densities ranging from 1 to 20 J/cm^2 during PLD. The hydrogen generation yields, as a function of time, produced by hydrolysis of alkaline $NaBH_4$ (0.025 M) solution using these Co-P-B films are reported in Fig. 5.6 and the corresponding R_{max} values are summarized in Table 5.1. The Co-P-B film deposited at the lowest laser energy density of 1 J/cm^2 shows negligible activity. The highest H_2 generation rate is observed with the film deposited at laser energy density of 3 J/cm^2, while the films deposited at higher laser energy densities (15 and 20 J/cm^2) showed lower H_2 generation rate. SEM images (secondary electrons) of the Co-P-B films deposited with laser energy densities of 1, 3, 9, and 15 J/cm^2 are reported in Fig. 5.7 (a), (c), (e), and (g) respectively. Spherical nanoparticles having similar average size are observed on the surface of all the Co-P-B films irrespective of the laser deposition energy densities.

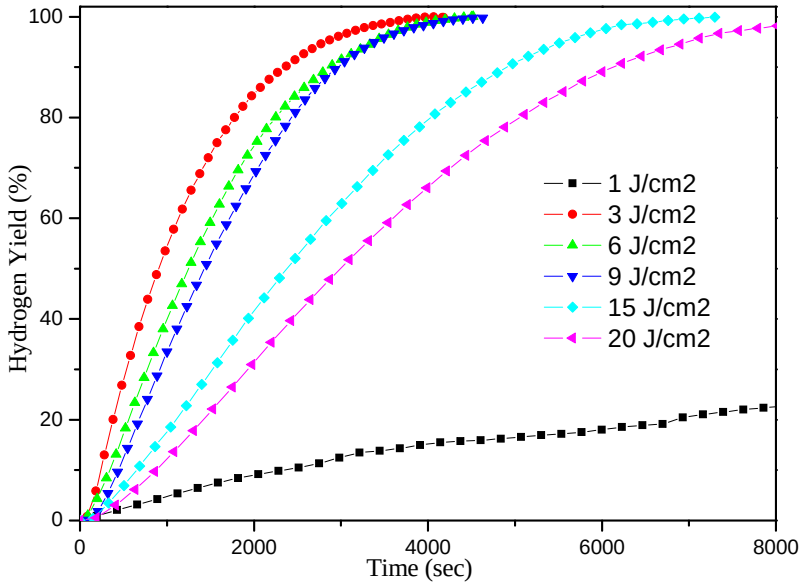

Figure 5.6 – Hydrogen generation yield as a function of reaction time obtained by hydrolysis of alkaline $NaBH_4$ (0.025 M) with Co-P-B films synthesized by PLD using different laser energy densities

For this reason we suppose that the different catalytic efficiencies of Co-P-B films deposited at different energies could be related to the different atomic composition of the ablated nanoparticles. To clarify this point, the compositional SEM images of all the Co-P-B films were acquired in back scattered electrons (BSE) mode

Fig. 5.7 (b), (d), (f), and (h). In BSE images, the materials of heavy and light elements can be readily distinguished through their brightness. By comparing secondary electrons (SE) image in Fig. 5.7 a and the corresponding BSE image (Fig. 5.7 b) of the Co-P-B film deposited at 1 J/cm^2, one can clearly conclude that the particles formed on the surface of the films are essentially P and B light elements having low brightness and hence difficult to be detected in BSE image. Only those particles containing cobalt are visible because of their brightness. Particles containing Co appear smaller in size in BSE image (Fig. 5.7 b) as compared to SE image (Fig. 5.7 a) because the Co particles are clearly encapsulated by P and B layers. We tentatively attribute this special feature of the PLD cluster assembled films to the preferential ablation of light atoms at low laser pulse energy. The low catalytic activity of the film deposited at 1 J/cm^2 is explained on the basis of the SEM detected composition where the P and B particles prevail over the Co particles which, in addition, are covered by the light elements. Additional information is provided from the elemental composition of all the films measured by EDS and summarized in Table 5.1. The atomic percentage ($at.\%$) of Co and P are only reported in the table because with EDS it is difficult to measure the right amount of B. The $at.\%$ of Co in the film deposited at 1 J/cm^2 is very low as compared to all the other films deposited at higher energy densities.

Laser energy density (J/cm^2)	Maximum H_2 generation rate (R_{max}) ($ml/min/g\,catalyst$)	Co and P atomic content of Co-P-B films ($at.\%$)	
		Co	P
1	∼250	∼45%	∼55%
3	∼4320	∼80%	∼20%
6	∼3210	∼82%	∼18%
9	∼2990	∼86%	∼14%
15	∼1640	∼90%	∼10%
20	∼1250	∼90%	∼10%

Table 5.1 – Co and P atomic content of Co-P-B films synthesized by PLD using different laser energy densities and their corresponding maximum hydrogen generation rates obtained from the hydrolysis of alkaline $NaBH_4$ (0.025 M).

The cluster-assembled film deposited at 3 J/cm^2 contains both Co as well as P and B particles as deduced by comparing the SE (Fig. 5.7 c) and BSE images (Fig. 5.7 d). Here, the EDS analysis shows around 80 $at.\%$ of Co and 20 $at.\%$ of P. Thus, the highest

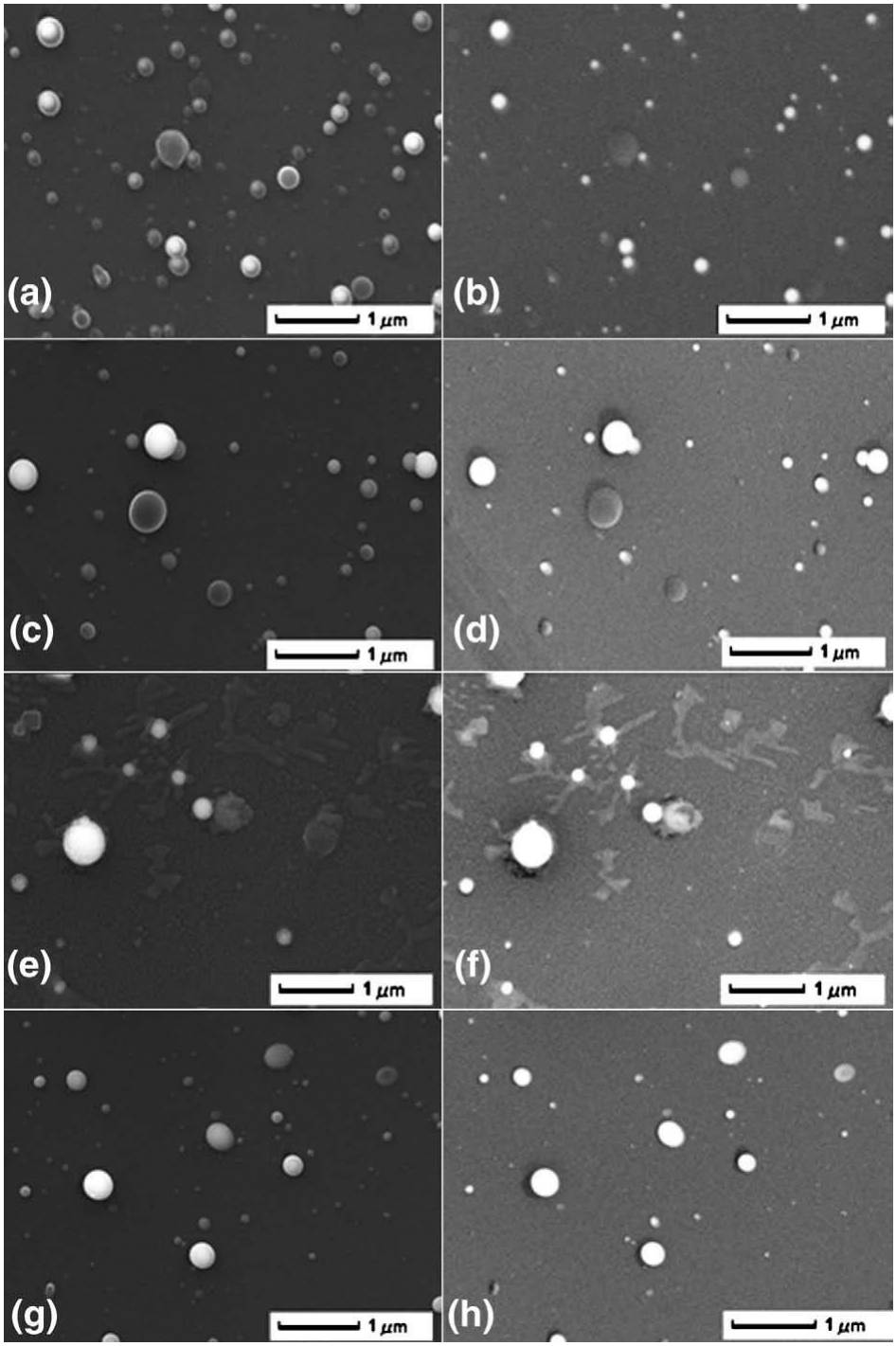

Figure 5.7 – Secondary electron image of the films deposited with laser energy densities of: (a) $1\,J/cm^2$, (c) $3\,J/cm^2$, (e) $9\,J/cm^2$, and (g) $15\,J/cm^2$ and their corresponding back scattering electron images (b), (d), (f), and (h) respectively.

H_2 generation rate obtained with this film is due to the presence of particles of the catalyst element in optimum concentration [78]. By preparing cluster-assembled films with higher laser energy density of 9 J/cm^2, a good catalytic activity still remains even if the efficiency values are decreasing from the maximum obtained with 3 J/cm^2. EDS analysis indicates that Co becomes prevailing in atomic composition but this is not the best situation for the Co-P-B catalyst because we have proved that B and P play a special role to enhance catalytic activity [78]. The same considerations apply to films prepared with 15 and 20 J/cm^2.

Considering the above reported results Ni-foam coated with Co-P-B film by ED can be used as catalyst fixed screen through which $NaBH_4$ solution continuously flows in the reactor to produce hydrogen. On contrary the inner wall of the reactor tube should be coated with efficient nanoparticle-assembled Co-P-B catalyst film synthesized by PLD to ensure a very efficient reaction rate. In conclusion, the proposed scheme to use ED- and PLD-catalysts would make sure that 100% $NaBH_4$ is converted into H_2 with high generation rate[3].

5.2 Co-B on carbon film

We have studied the catalytic behivour of Co-P-B nanoparticles-assembled thin film. In the past we have also seen that Co-B nanoparticles-assembled thin film, and Pd supported on rough carbon thin film were successfully developed by PLD and tested for catalytic hydrolysis of $NaBH_4$ solution to generate pure H_2 gas. Both these kinds of catalyst films showed excellent activity to produce expected amount of H_2 from hydrolysis of $NaBH_4$ with significantly higher rates than the same amount of the corresponding powders. For Co-B and Co-B-P film, the enhanced catalytic activity are mainly attributed to the Co-B and Co-B-P nanoparticles, produced during the ablation process on the film surface and well established spherical form [78, 97, 116]. These nanoparticles not only increase the surface area of the catalyst but also act as the active catalytic centres for the hydrolysis reaction of $NaBH_4$. The highly porous and irregular morphology of carbon support provides very high initial surface area and better dispersion of Pd particles on the surface [108, 117]. These results showed that the nanoparticles and appropriate carbon film morphology were the main reason behind the enhanced performance. Considering these results, in the present work we combine the two features (nanoparticles and rough support surface) to synthesize

[3] *more experiments are required for better understand of the mechanisms related to laser ablating*

Co-B nanoparticles on highly irregular and porous carbon film support to improve the initial surface area and obtain better dispersion of nanoparticles.

Co-B film supported on carbon was synthesized in two steps: 1) by depositing carbon film by PLD, on a glass substrate, using a laser fluence of 12 J/cm^2 and varying Ar pressure from 10 to 50 Pa to obtain different surface roughness; 2) by PLD of Co-B nanoparticles-assembled film over these carbon substrates in vacuum with same laser parameters as used to deposit unsupported Co-B film. Weight of the catalyst loading was evaluated by measuring the weight of the glass slide (76×46 mm) with carbon film, before and after deposition of Co-B film: it was kept approximately constant for all the produced samples (10 mg). Films were deposited on silicon substrates for the characterization and on glass substrates to test their catalytic activity

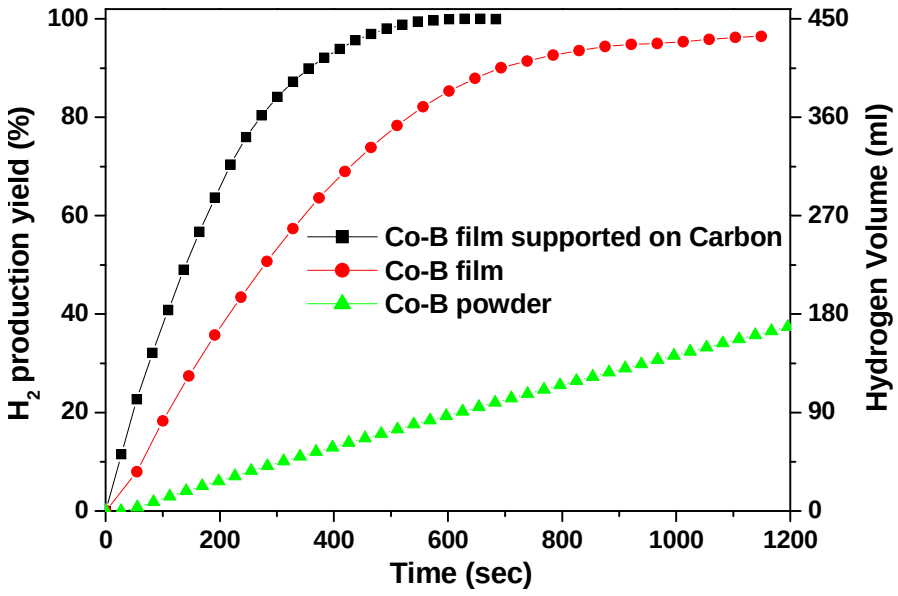

Figure 5.8 – Hydrogen generation yield as a function of reaction time obtained by hydrolysis of alkaline $NaBH_4$ solution (0.025 M) with Co-B catalyst powder and with unsupported and C-supported Co-B film deposited by PLD. Carbon film used for the measurement was deposited with Ar pressure of 40 Pa.

Hereafter Co-B film deposited on glass substrate and on carbon film will be designated as unsupported- and C-supported Co-B film, respectively. The catalytic activity of C-supported and unsupported Co-B film was compared by measuring the hydrogen generation yield as function of time by hydrolysis of alkaline $NaBH_4$ (0.025 M) solution at 298 K: results are reported in Fig. 5.8. The figure clearly shows that both

the Co-B catalysts films are really efficient and produce hydrogen instantaneously as soon as they come in contact with the $NaBH_4$ solution. However, the C-supported Co-B film exhibits higher catalytic activity as compared to the unsupported Co-B film and it was able to complete the reaction within 10 mins while the same amount of unsupported Co-B film catalyst ($10\,mg$) takes about 18 mins and the Co-B powder catalyst takes 85 mins. The expected total amount of H_2 was measured irrespective of the type of catalyst used. The H_2 generation yield values reported in Fig. 5.8 are perfectly fitted by using a single exponential function.

A numerical procedure, was used to obtain the maximum value of the hydrogen generation rate (R_{max}) for all the catalysts. By using same catalyst amount ($10\,mg$), the maximum H_2 generation rate obtained for C-supported Co-B films ($\sim 8100\,ml/min/g\,catalyst$) has been found significantly higher (almost 2 times) than that obtained using the unsupported Co-B film ($\sim 4330\,ml/min/g\,catalyst$). While the R_{max} value for C-supported Co-B films is about one order of magnitude higher than Co-B powder catalyst ($\sim 680\,ml/min/g\,catalyst$). Several films synthesized by using the same PLD parameters showed almost identical ($\pm 5\%$) H_2 generation rate, thus establishing the reproducibility of our produced PLD films. During the reaction, the catalyst films were quite stable both in terms of hydrogen-production and bonding with the substrate.

In Fig. 5.9 we present SEM images of Co-B catalyst powder and of both films (unsupported and C-supported) synthesized by PLD. The SEM images of catalyst powders show typical particle-like morphology with spherical shape and average size of a few nanometers. However, because of the high surface energy related to these particles, they tend to agglomerate as observed in the SEM image (Fig. 5.9 a). As seen in Fig. 5.9 b, the surface of unsupported Co-B catalyst films exhibit a nanoparticles-assembled structure made of well dispersed spherical particles with size ranging between 50 to $300\,nm$. In addition to this Co-B nanoparticles we also observed much smaller Co nanoparticles (NPs) embedded in boron matrix on the film surface by TEM. Fig. 5.10 a represents the bright-field TEM micrographs of Co-B film surface deposited by PLD using laser fluences of 3 J/cm^2. The Co-NPs, with well defined spherical shape and average size of 11 ± 4 nm, are observed to be well-dispersed in the matrix of light element (especially boron or boron-oxide) as confirmed by energy dispersive X-ray spectroscopy. The histograms of particle size distribution are illustrated in Fig 5.10 b, while the particle density (with size D $<$ 30 nm) calculated from this plot is about $320 \pm 30\,NP/\mu m^2$. Depending on the laser energy density and tar-

get material thermodynamic properties, the laser ablation process falls into two main categories: vaporization (also intense vaporization) and explosive boiling [114, 118].

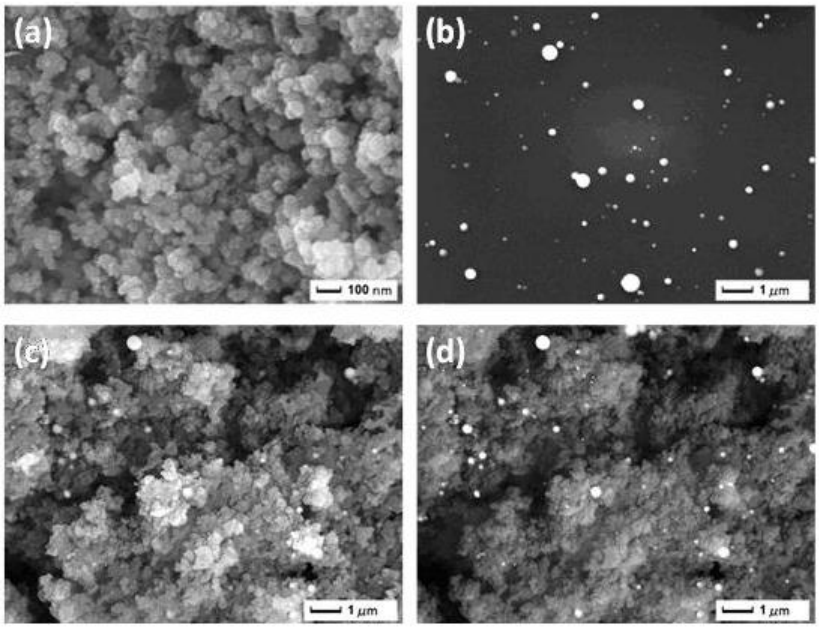

Figure 5.9 – SEM micrographs of Co-B catalyst: (a) powder, (b) unsupported film, and (c) C-supported film deposited by PLD. (d) Back scattering electron image of C-supported Co-B film. Carbon film used for the measurement was deposited with Ar pressure of 40 Pa.

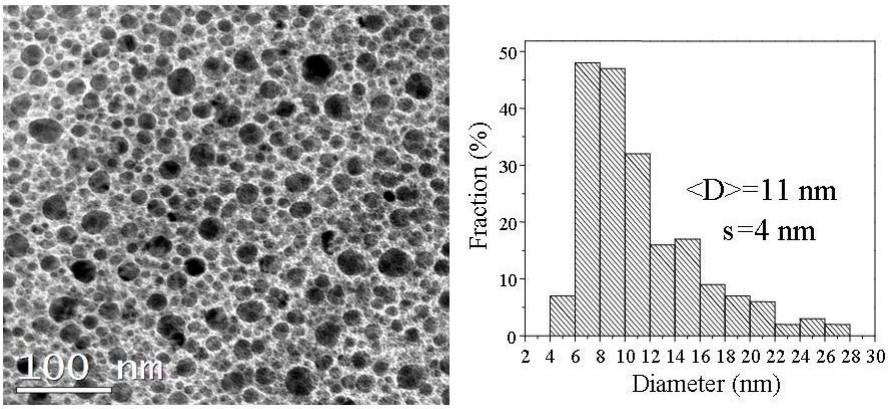

Figure 5.10 – (a) Bright field TEM images and (b) particle size histogram for unsupported Co-B catalyst film deposited by PLD using energy density of $3\,J/cm^2$

The mechanism of direct nanoparticle formation is here attributed to the phase explosion process that occurs under extreme conditions of high temperature and pressure produced by the laser pulses irradiating targets in vacuum [119]. As discussed earlier, high energy density laser beam irradiation causes a superheating of the region

below the target surface beyond the limit of thermodynamic stability of the material ($\sim 90\%$ of the thermodynamic critical temperature, T_c) inducing a homogeneous nucleation of vapor bubble. The target surface then makes a rapid transition from superheated liquid to a matrix of vapour and liquid nano-size droplets, which leave the irradiated target surface and get deposited on the substrate: this is the case for Co-B nanoparticles ($50 - 300\,nm$ range) formation on the surface. The phase explosion process occurs in a superheated liquid near T_c and we suppose that the emitted liquid would have a homogeneous Co-B composition. However, either during the flight from target to substrate, or just on the substrate, cooling processes will occur that could lead to phase separation and Co NP formation within the boron matrix occurs on the surface. However, the involved mechanisms are still to be well understood. SEM images of C-supported Co-B film (Fig. 5.9 c) show dendritic microstructure of carbon film with highly irregular and porous surface. To clearly identify Co-B particles in carbon film the compositional SEM image in backscattering electron mode (BSE) was acquired (Fig. 5.9 d). In BSE images materials of heavy and light elements can be readily distinguished through their brightness. Thus, from Fig. 5.9 d, it is clearly evident the presence of Co-B nanoparticles (bright particles) embedded in the porous carbon film with improved dispersion. The mechanism behind the formation of such rough carbon surface through PLD is discussed below. The above morphological results confirm the enhanced catalytic activity obtained with Co-B film, as compared to powder, is primarily attributed to the Co-B nanoparticles which act as active catalytic centres for the hydrolysis reaction. Depositing these active Co-B nanoparticles on carbon film gives rise to a further enhancement in catalytic activity which is mostly ascribed to highly rough and porous carbon surface which: 1) favours the better dispersion of the nanoparticles, 2) provides high initial surface area, and 3) stabilizes the nanoparticles against aggregation. To further confirm the role of carbon film we used different Ar pressure in PLD chamber, ranging from 10 to 50 Pa, to tailor roughness of deposited C-films. The SEM images of the carbon films deposited under Ar gas pressure of 20, 30, 40 and 50 Pa are illustrated in Fig 5.11(a), (c), (e), and (g), while Co-B film supported on these carbon films are reported in Fig. 5.11(b), (d), (f), and (h), respectively. Microstructures ranging from flat to highly irregular and to porous are clearly visible. The carbon film deposited at low Ar pressure (20 Pa) exhibits columnar structure (observed through cross-section SEM images of the film, figure not shown) with embedded spherical nodules on the surface. By increasing the pressure (to 30 and 40 Pa) dendritic, highly porous microstructure starts to appear with extremely irregular surface. The nodes in this case appear bigger, loosely packed, and

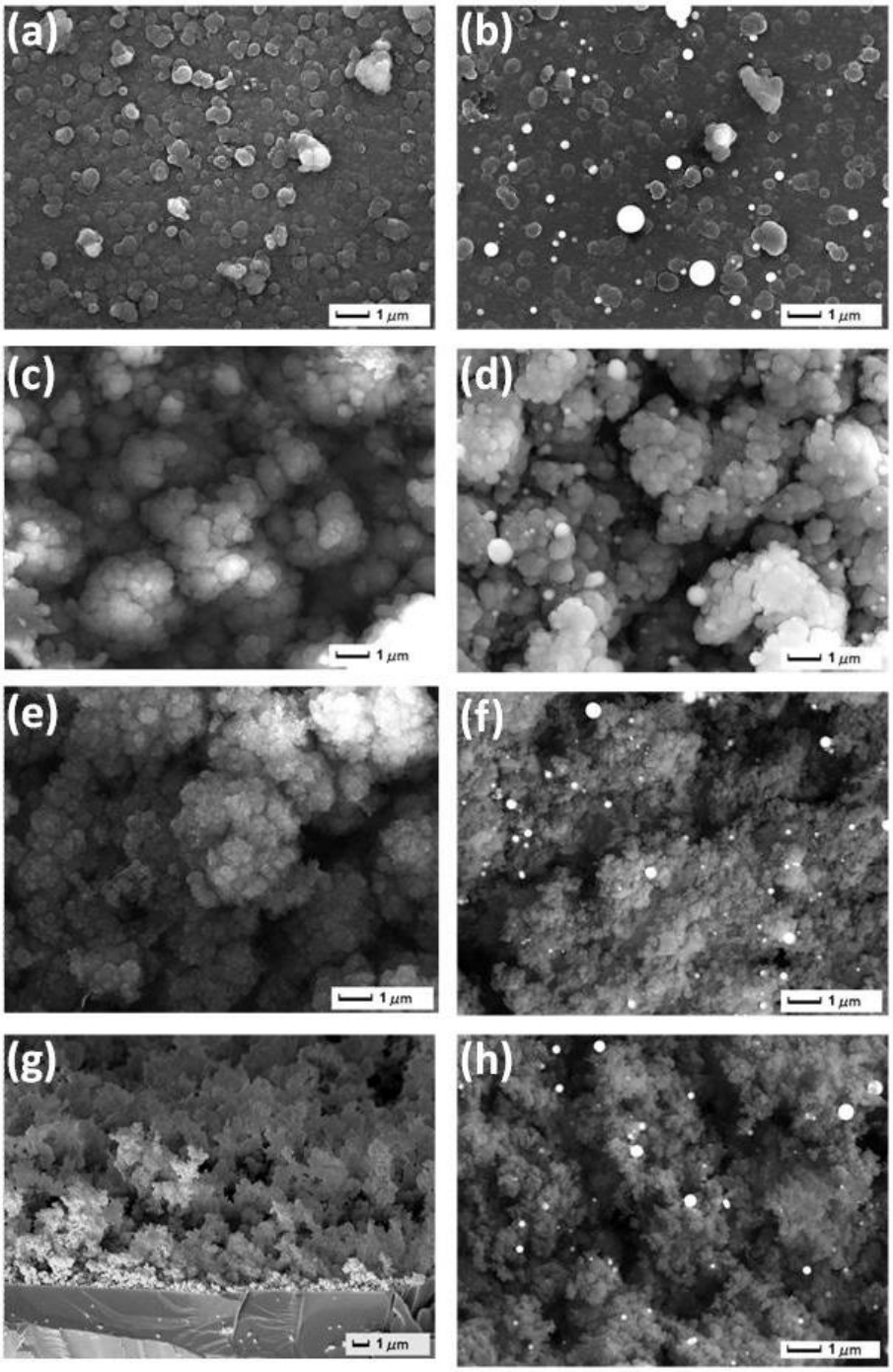

Figure 5.11 – SEM micrographs of the carbon films deposited under different Ar gas pressures (a) 20, (c) 30, (e) 40 and (g) 50 Pa, while (b), (d), (f) and (h) are the SEM images of Co-B film supported on these carbon films, respectively

non-spherical. Film-substrate adhesion is slightly poor than that reached at low Ar pressure. When using high pressure conditions (50 Pa), the film appears powder-like, with barely any adhesion to the substrate. The morphology of such a film is very similar to that of simulated films grown under ballistic deposition conditions. The collision effects imposed by inert gas (Ar) at high pressure in the deposition chamber cause a cooling down of plume along with charges recombination and condensation of carbon clusters in the plume which are deposited on the substrate. In particular, by increasing the gas pressure, cluster-cluster collision may also occur that contributes to formation of bigger clusters which when assembled form highly porous and irregular structure on the film surface.

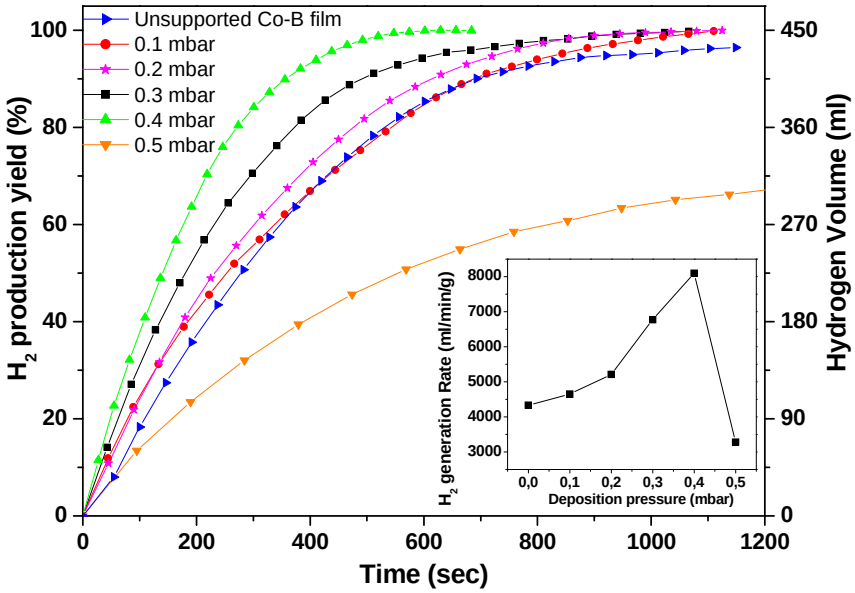

Figure 5.12 – Hydrogen generation yield as a function of reaction time obtained by hydrolysis of alkaline $NaBH_4$ solution (0.025 M) with Co-B film catalyst supported on carbon films deposited with various Ar pressures by PLD. Inset shows the R_{max} as a function of Ar gas pressure used to deposit the carbon films

Hydrogen generation yield was measured, as a function of time, during the hydrolysis of alkaline $NaBH_4$ solution (0.025 M) at 298 K in presence of Co-B film catalyst supported on different carbon films deposited with various Ar pressures ranging from 10 to 50 Pa (Fig. 5.12). The inset of Fig. 5.12 shows the R_{max} as a function of Ar gas pressure used to deposit the carbon films. Co-B catalysts supported on C-film deposited at low Ar pressures (10 and 20 Pa) show almost similar catalytic activity as un-supported Co-B film. We attribute this result to the non-porous structure of C-films. However, the catalytic activity increases for Co-B catalysts supported on

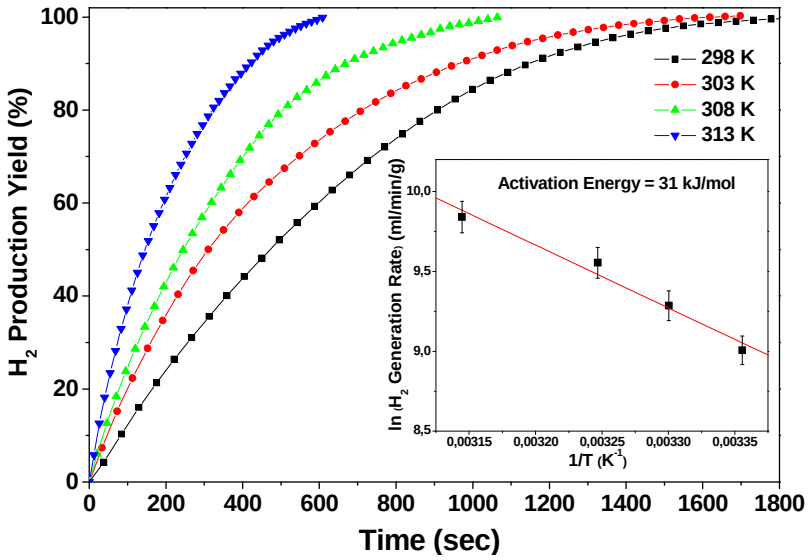

Figure 5.13 – Hydrogen generation yield as a function of reaction time obtained by hydrolysis of alkaline $NaBH_4$ solution (0.025 M) with C-supported (40 Pa) Co-B film catalyst measured at 4 different solution temperatures. Inset shows the Arrhenius plot of the H_2 generation rates.

C-films deposited at higher Ar pressures (30 and 40 Pa). R_{max} reached the maximum for C-film deposited at 40 Pa. As indicated by SEM images, the roughness and surface area of C-film increases with the deposition pressure. This trend is also followed by the H_2 generation rate for hydrolysis of $NaBH_4$ as demonstrated in the inset of Fig. 5.12. Thus, surface area and roughness of C-films play a vital role in the increment of catalytic activity for Co-B film catalyst by providing better dispersion and avoiding aggregation of Co-B nanoparticles. On the contrary, Co-B catalyst supported on C-film deposited at highest pressure of 50 Pa shows a drastic decrease in the H_2 generation rate and was not able to complete the hydrolysis reaction of $NaBH_4$. The C-film deposited at this pressure has a very week adhesion with the substrate and thus under vigorous stirring the film slowly detached from the substrate in the reactant solution during the $NaBH_4$ hydrolysis reaction.

In Fig. 5.13 the H_2 generation yields, obtained through hydrolysis of alkaline $NaBH_4$ (0.025 M) solution using C-supported Co-B film, is reported as a function of time at different reaction temperatures. The carbon film deposited with Ar pressure of 40 Pa was used for the measurement. The Arrhenius plot of the hydrogen production rates (inset of Fig. 5.13) gives an activation energy value of $31 \pm 2\, kJmol^{-1}$ for C-supported nanoparticles-Co-B film which is the same as that obtained with unsupported nanoparticles-Co-B film ($30 \pm 1\, kJmol^{-1}$) [97] but much lower than that of Co-B powder ($45 \pm 1\, kJmol^{-1}$) [98]. In general, the obtained

activation energies are lower than that obtained with Co-B supported on different materials such as carbon ($57.8\,kJmol^{-1}$) [120], and Ni foam ($33\,kJmol^{-1}$) [121]. The present value is also lower than that of Co-based catalyst for example *Raney Co* ($53.7\,kJmol^{-1}$) [53], Co-B nanoparticles ($42.7\,kJmol^{-1}$) [107], Co supported on activated carbon ($44\,kJmol^{-1}$) [122], structured Co_2B ($45\,kJmol^{-1}$) [55], Co-B thin film ($44.47\,kJmol^{-1}$) [50] and Co supported on $\gamma - Al_2O_3$ ($33\,kJmol^{-1}$) [101], The values are also lower than that found by Amendola ($47\,kJmol^{-1}$) [16] by using Ru catalyst. Kaufman and Sen [45], by using different bulk metal catalysts, obtained $75\,kJmol^{-1}$ for cobalt, $71\,kJmol^{-1}$ for nickel, and $63\,kJmol^{-1}$ for Raney nickel.. The activation energy values obtained in the present case are comparable to that obtained with Pd/C powder ($28\,kJmol^{-1}$)) [108], Ru nanoclusters ($29\,kJmol^{-1}$) [52], and Ru-C ($37\,kJmol^{-1}$) [109]. The favourable activation energy values obtained in the present work are attributed to active nature of Co-B nanoparticles which are well dispersed in porous carbon film that indeed provides the initial high surface area and avoids agglomeration thus enhancing the catalytic hydrolysis reaction.

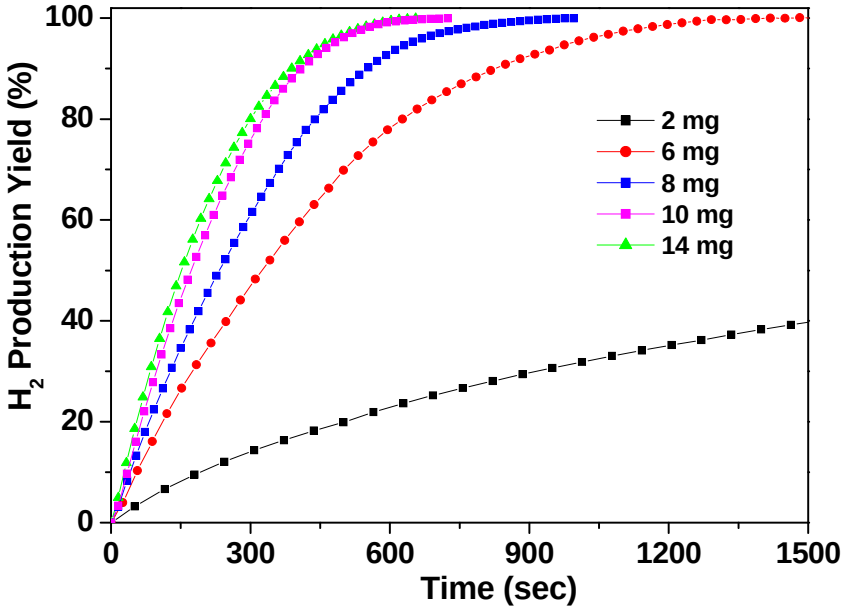

Figure 5.14 – Hydrogen generation yield as a function of reaction time obtained by hydrolysis of alkaline $NaBH_4$ solution (0.025 M) at 298 K in presence of Co-B catalyst with different loadings (2, 6, 8, 10, 14 mg) on carbon film support (40 Pa).

The effect of catalyst loading on catalytic activity of Co-B/C catalyst was studied by depositing different amount of Co-B catalyst on carbon film (deposited with 40 Pa Ar pressure). Fig. 5.14 presents the hydrogen generation yield, as a function of time, occurring from the hydrolysis of alkaline $NaBH_4$ solution (0.025 M) at 298 K

in presence of Co-B catalyst with different amount of loading (2, 6, 8, 10, 14 mg) on carbon film support. It is observed that H_2 generation rate (H_2 ml/min) increases with Co-B loading and takes less amount of time to produce the expected amount of H_2. However for higher Co-B loading, more than 10 mg, no further increment in H_2 generation rate is observed. This result shows that 10 mg is enough to cover the carbon film with better dispersion of NPs while high loading might decrease the level of dispersion.

5.3 Conclusion

Co-P-B catalyst thin films have been synthesized on Ni-foam and glass substrate by using ED and PLD respectively. The efficiency of these catalyst films was tested for hydrolysis of $NaBH_4$ for H_2 generation and comparison was made with Co-P-B powder catalyst. Co-P-B films deposited on Ni-foam, with 3-4 layers, show catalytic efficiency comparable to the powder. On contrary Co-P-B films prepared by PLD exhibit much superior H_2 generation rate as compared to Co-P-B powder. Specifically, R_{max} obtained with chemically synthesized Co-P-B powder is $\sim 2010\, ml/min/g\, catalyst$, with films on Ni-foam R_{max} is $\sim 2090\, ml/min/g\, catalyst$, while with Co-P-B films synthesized by PLD R_{max} is $\sim 4230\, ml/min/g\, catalyst$.

The increased efficiency of the PLD films is mainly attributed to the nanoparticles formed on the catalyst surface, due to deposition process, which increases active surface area and also favours electronic exchange mechanisms to promote efficient hydrolysis process for H_2 gas generation. Nanoparticles observed on PLD films are generated by phase explosion phenomena occurring in laser-irradiated material for appropriate parameters of the laser pulse. We have proved that nanoparticles must have a specific atomic composition to exhibit the best catalytic effect. The atomic composition of the synthesized nanoparticles depends on the laser pulse energy: specifically, we observed that by increasing the laser pulse energy, the atomic composition of the heavier element (Co) is prevailing over the light elements.

Co-B nanoparticles supported on carbon films were synthesized by using PLD and used as catalysts in the hydrolysis of $NaBH_4$ to produce H_2. Several Ar pressures, in the range from 10 to 50 Pa, were used during PLD of carbon films to tailor the roughness and porosity of carbon support prior to PLD of Co-B film. The hydrogen generation rate attained with carbon-supported Co-B catalyst film (Ar pressure of 40 Pa for C deposition) is significantly higher ($\sim 8100\, ml/min/g\, catalyst$) as compared to unsupported Co-B film ($\sim 4330\, ml/min/g\, catalyst$) and to conventional

Co-B powder ($\sim 680\, ml/min/g\, catalyst$). SEM analysis along with $NaBH_4$ hydrolysis tests show that the Co-B nanoparticles act as active catalytic centres for hydrolysis while the carbon support provides both better dispersion of the Co-B nanoparticles and atomic barriers that avoid nanoparticles segregation. The hydrogen generation rate obtained by the present carbon-supported Co-B catalyst was also investigated as a function of Co-B loading and solution temperature. The H_2 generation rate increases as function of loading but no further increment is observed for loading exceeding $10\, mg$ that is indeed enough to cover the carbon film with the best dispersion of Nanoparticles. Finally, the high performance of our carbon-supported Co-B film is well supported by the obtained very low activation energy ($\sim 31\, kJ\, (mol)^{-1}$) in the hydrolysis of $NaBH_4$.

Chapter 6

Catalysts for hydrolysis of Ammonia Borane

"Enjoy the little things, for one day you may look back
and realize they were the big things."
-Robert Brault

6.1 Metal doped Co-B powder catalyst

In the present work, we investigate the effect of the various dopant transition-metals (such as Cu, Cr, Mo, and W) in Co-B catalyst powder on hydrogen production by hydrolysis of Ammonia Borane. We will see that all these dopant metals significantly improve the catalytic performance of the Co-B catalyst. The role of each metal species in the alloy catalysts is revealed from the experiments carried out using various techniques used to characterize the catalysts. In Chapter 4, we have synthesized and systematically analyzed Co-B based ternary alloy catalysts for H_2 generation by hydrolysis of $NaBH_4$. Various transition metals, namely Ni, Fe, Cu, Cr, Mo, and W, were doped with Co-B catalyst in different concentration to establish the role of each dopant metal in the electron exchange mechanism involved in $NaBH_4$ hydrolysis. Cr, W, Mo, and Cu offered considerable promoting effects on the Co-B catalyst by increasing the H_2 generation rate by 3-4 times as compared to the undoped catalyst. On the contrary, Ni and Fe were only able to create a marginal increment in the catalytic performance of the Co-B catalyst. Considering these previous results, the aim of the present work is to test Cr, W, Mo, and Cu doped Co-B ternary alloy catalysts for the hydrolysis of AB.

We have also learnt (in Chapter 4) that, Co-Cu-B, Co-Cr-B, Co-Mo-B, and Co-W-B ternary alloy catalyst powders, with molar ratio of $\chi_{Cu} = 35\%$, $\chi_{Cr} = 4\%$,

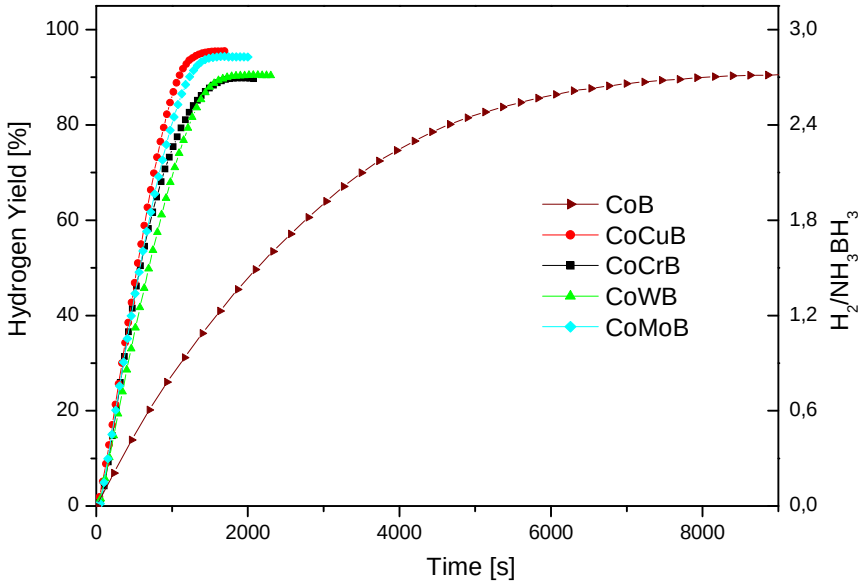

Figure 6.1 – Hydrogen generation yield as a function of reaction time obtained by hydrolysis of AB solution (0.025 M) with of Co-B, Co-Cu-B($\chi_{Cu} = 35\%$), Co-Cr-B($\chi_{Cr} = 4\%$), Co-Mo-B($\chi_{Mo} = 5\%$), and Co-W-B($\chi_W = 5\%$) powder catalysts at 298 K.

$\chi_{Mo} = 5\%$ and $\chi_W = 5\%$, showed maximum H_2 generation rate for the hydrolysis of $NaBH_4$ [123]. Therefore presently we consider just these particular molar ratio values for the catalytic hydrolysis of AB. Hydrogen generation yield was measured, as a function of time, during the hydrolysis of AB (0.025 M) solution in presence of Co-B, Co-Cu-B($\chi_{Cu} = 35\%$), Co-Cr-B($\chi_{Cr} = 4\%$), Co-Mo-B($\chi_{Mo} = 5\%$), and Co-W-B($\chi_W = 5\%$), powder catalysts at 298 K (Fig. 6.1).

The figure clearly shows that all the catalyst powders are highly active and produce hydrogen instantaneously as soon as they come in contact with the hydride solutions. It may be noted that, Cu, Cr, Mo, and W metal doped Co-B catalyst powders exhibit much higher catalytic activity as compared to the undoped-Co-B powder. Only 25-30 mins were required to complete the reaction by the ternary alloys, while the same amount of Co-B powder catalyst ($\sim 10mg$) took about 145 mins. The total amount of hydrogen generated by hydrolysis of AB using Co-Cu-B ($\frac{H_2}{NH_3BH_3} = 2.88$) and Co-Mo-B ($\frac{H_2}{NH_3BH_3} = 2.83$) powders is closer to the quantitative yield as expected from the reaction stoichiometry ($\frac{H_2}{NH_3BH_3} = 3.0$), than that generated by Co-Cr- B and Co-W-B ($\frac{H_2}{NH_3BH_3} = 2.7$). Nevertheless all the ternary alloy catalysts generate higher amount of H_2 gas than undoped-Co-B powder ($\frac{H_2}{NH_3BH_3} = 2.55$). In addition to the volumetric measurement of H_2 generation, the conversion of the AB was also monitored through ^{11}B NMR by comparing the intensity of the AB signal in the

NMR spectra during the course of the reaction. The peaks assigned to borate species are only visible after the completion of reaction.

The H_2 generation yield values for the undoped-Co-B powders reported in Fig. 6.1 were perfectly fitted by using a single exponential function (see eq. 4.1) indicating that hydrolysis reaction is first order reaction with respect to AB concentration. On the contrary, the H_2 generation data produced by the metal-doped Co-B ternary alloy catalyst powders was fitted with a linear function thus proving zero order reaction with respect to AB concentration. A numerical procedure[1], was used to obtain the maximum value of H_2 generation rate (R_{max}) for all the catalyst powders: these values are summarized in Table 6.1. The R_{max} values measured with the catalyst powders decrease in the following order: Co-Cu-B > Co-Mo-B > Co-Cr-B > Co-W-B > Co-B.

The measurements are repeated at least 3 times to verify the obtained results. The Co-Cu-B catalyst powder ($\sim 1250 ml/min/g$ catalyst) shows about 3.5 times higher H_2 generation rate as compared to that achieved with only Co-B catalyst powder ($\sim 360 ml/min/g$ catalyst). The above results demonstrate that doping Co-B powder with the transition metals: Cu, Cr, Mo, and W, enhances the catalytic efficiency of the catalyst. While most of the characterizations of ternary catalysts were accomplished in Chapter 4, here we present the most relevant results to understand the promoting effect of each dopant transition metal. All the catalyst powders show similar particle-like morphology with particles having spherical shape and size in a range of $30-50\,nm$ as ascertained by SEM (Fig. 4.8). However, at higher SEM magnification undoped-Co-B powder displays particles mostly in agglomerated state, while lower degree of agglomeration is observed with Co-Cu-B, Co-W-B, Co-Cr-B, and Co-Mo-B powders. Metal to cobalt ratio in all the alloy catalysts was confirmed by EDS. Structural characterization indicates the amorphous nature of all the catalyst powders with a broad peak at around $2\theta = 45^{o}$ assigned to the amorphous state of Co-B alloy (Fig. 4.9). Finally, the diffraction spectra indicate short-range order and long-range disorder and both the features are expected to enhance the catalytic activity. .

The measured BET surface area of all the catalyst powders is reported in Table 6.1. The specific surface area decreases in following order: Co-Cu-B > Co-W-B > Co-Mo-B > Co-Cr-B > Co-B. This shows that doping the Co-B catalyst with transition metals (Cu, Cr, Mo, and W), causes an increase in the specific surface area irrespective of the type of dopant. Histograms representing particle size distribution of all the catalyst powders are shown in Fig. 6.2. These plots show the frequency

[1]See Appendix A

Catalyst powder	Max H_2generation rate (R_{max}) $(ml/min/g\,catalyst)$	BET Surface area $(m^2 g^{-1})$	Activation energy $(kJ.mol^{-1})$	Average Particle size (nm)
Co-B	362	20	44	1940 nm
Co-Cu-B	1254	115	41	194 nm
Co-Cr-B	1058	40	44	410 nm
Co-Mo-B	1231	43	43	641 nm
Co-W-B	1000	54	38	247 & 763 nm

Table 6.1 – Maximum H_2 generation rate, Surface area, Activation energy, and Average particle size of the as-prepared alloy catalyst powders.

distribution or histogram (% channel) of particle sizes and their cumulative distribution (% passing). The evaluated mean particle diameter of the catalyst powders is summarized in Table 6.1. The average particle size of undoped-Co-B powder is around $\sim 2\,\mu m$ which decreases by the addition of different transition-metal dopants (Cu, Cr, Mo and W). The Co-B catalyst doped with Cu metal (Co-Cu-B) exhibits the lowest average particle size of about $\sim 200\,nm$: one order of magnitude lower than the undoped-Co-B catalyst. Two sets of particles with average size of ~ 250 and $\sim 750\,nm$ can be seen for Co-W-B catalyst.

As revealed by the particle size analysis, almost all the particulate present in undoped-Co-B powder have size greater than $1\,\mu m$ but, the SEM images (see Fig. 4.8) clearly indicate that the particles on the catalyst surface have size of $30 - 50\,nm$. This can be explained by the fact that the high surface energy of particles, during the exothermic reduction reaction, causes Co-B particles to agglomerate to form big clusters (size more than $1\,\mu m$) where the active surface area is reduced. When small amount of Cr, Mo or W ($\chi_{Cr,\,Mo,\,W} = 4 - 5\%$) is included as dopant in Co-B, the specific surface area of the catalyst increases by almost 2 to 2.5 times, which is due to the limited particle agglomeration as compared to pure Co-B (see Fig. 6.2). Surface characterization (Fig. 4.11) of these catalyst powders suggests that Cr, Mo, and W in form of oxides are located on the surface of the catalyst. These metal oxides act as a kind of atomic barrier between the several Co-B nanoparticles thus avoiding agglomeration caused by their high surface energy. As a result, the effective surface area increases significantly for Co-Cr-B, Co-Mo-B, and Co-W-B catalysts.

In the case of Co-W-B catalyst, tungsten is present in oxidized (67%) as well as in metallic (33%) form (as confirmed by XPS) and may be due to their dissimilar tendency to separate the Co-B particles, it leads to development of two sets of clusters (250 and $750\,nm$) for this catalyst. However, this point is not yet clear and requires more experimental evidence. A remarkable increment in the surface area (about 5.5 times), caused by the decrease in average particle size ($\sim 200nm$), is observed for Co-Cu-B catalyst as compared to the undoped Co-B. As revealed by XPS, the Cu on the catalyst surface is in completely metallic state which, like other metal oxides, acts as an atomic barrier to prevent the agglomeration of Co-B nanoparticles. The highest surface area of Co-Cu-B is mainly due to the high concentration of Cu ($\chi_{Cu} = 35\%$) as compared to Cr($\chi_{Cr} = 4\%$), Mo($\chi_{Mo} = 5\%$), and W($\chi_{W} = 5\%$) dopant in Co-B catalyst. In Chapter 4, we have seen that when transition metals are added at high concentration in Co-B catalyst, there is a very high increase in the surface area as compared to the undoped Co-B catalyst.

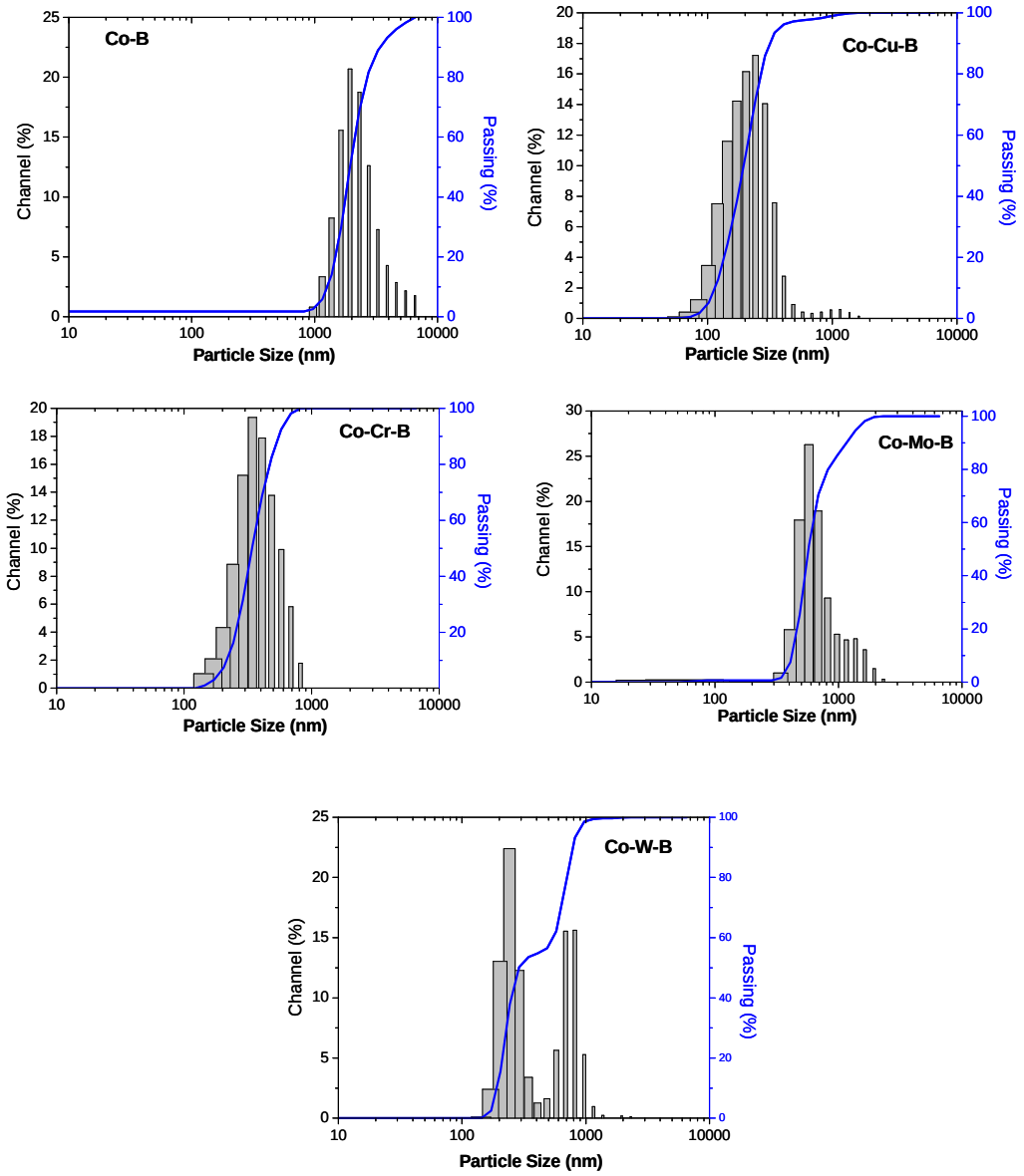

Figure 6.2 – Histograms representing particle size distribution for Co-B, Co-Cu-B ($\chi_{Cu} = 35\%$), Co-Cr-B ($\chi_{Cr} = 4\%$), Co-Mo-B ($\chi_{Mo} = 5\%$), and Co-W-B ($\chi_{W} = 5\%$) powder catalysts.

However, a deleterious effect in catalytic activity is detected with high concentration of the dopant metals (Cr, Mo, and W) due to the surface covering of the active Co metal by Cr, Mo, or W species. On the basis of the characterization results, the role of each dopant transition metal in the Co-B based ternary alloy powder catalyst is to act as atomic barrier to avoid Co-B particle agglomeration and thus favouring better particle dispersion. This leads to the significant increment in active surface area formed by smaller cluster as compared to the undoped-Co-B catalyst.

The H_2 production from the metal-catalyzed hydrolysis of NH_3BH_3 takes place, according to ref. [57], by the following kinetics steps: 1) metal-particle surface and NH_3BH_3 molecule form activated complex species where the interaction of the H_2O molecule leads to dissociation of the B–N bond; 2) BH_3^- ions chemisorbed on the metal (Co) atom transfer H^- to an unoccupied adjacent (Co) metal atom; 3) the hydrogen atom acquires an electron from the metal and leaves the site in hydridic form (H^-); 4) this H^- reacts with water molecule to produce H_2 and OH^-; 5) OH^- reacts with boron in BH_2^- to produce the $BH_2(OH)^-$ ion. Again, H^- is transferred from $BH_2(OH)^-$ ion to an unoccupied adjacent (Co) metal atom. The cycle of hydrogen absorption on metal sites continues till $BH_2(OH)^-$ forms $B(OH)_3^-$ and molecular hydrogen is released during each cycle. According to this hydrolysis reaction mechanism, the initial reaction occurs between NH_3BH_3reactant and metal sites which means that the reaction rate is proportional to the number of available metal sites for the absorption of BH_3^- ions in the solution. In this reaction scheme, the doped Co-B catalyst powder, having a surface area almost 3 to 5 times higher than that of Co-B, may provide an ideal condition for BH_3^- ion absorption for catalytic hydrolysis reaction: the main reason in enhancing the H_2 generation rate. However, during the last step, the reaction between $OH^-$and BH_2^- ions is not favoured by the catalyst which may lower the reaction rate. In the present Co-B based alloy catalyst, the Cr^{3+}, Mo^{4+}, and W^{4+} species act as Lewis acid sites for OH^- absorption due to the strong affinity of these sites towards oxygen of the OH^- group [78]. This bonding polarizes the hydroxyl group which becomes favourable to the reaction with boron species attached to the neighbouring Co active sites thus increasing the overall reaction rate.

6.1.1 Activation energy

The H_2 generation yield as a function of time was measured at different solution temperatures by hydrolysis of AB (0.025 M) solution using Co-B, Co-Cu-B(χ_{Cu} = 35%), Co-Cr-B(χ_{Cr} = 4%), Co-Mo-B(χ_{Mo} = 5%), and Co-W-B(χ_W = 5%), powder catalysts as reported in Figures 6.3 - 6.7 respectively. As expected, the H_2 generation rate increases with the temperature. The Arrhenius plot (inset of Figs. 6.4 - 6.7) of the hydrogen production rate permits the evaluation of the activation energies of the rate limiting steps: the values are summarized in Table 6.1. There is a slight decrease in the activation energy for the transition metal-doped Co-B catalyst powders as compared to the undoped Co-B catalyst powder ($44\,kJmol^{-1}$).

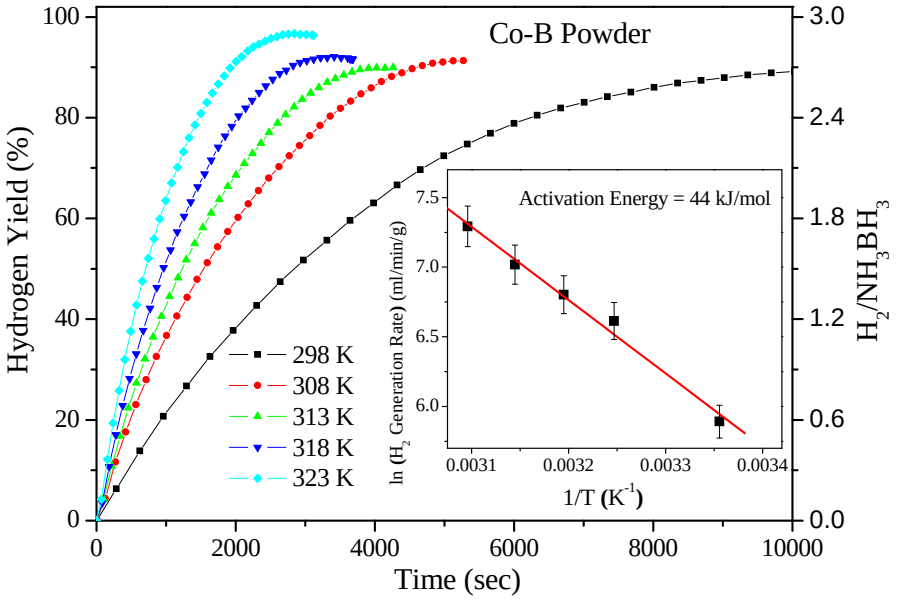

Figure 6.3 – Hydrogen generation yield as a function of reaction time by hydrolysis of NH_3BH_3 (0.025 M) solution with Co-B catalyst powder, measured at 5 different solution temperatures. Inset shows the Arrhenius plot of the H_2 generation rates

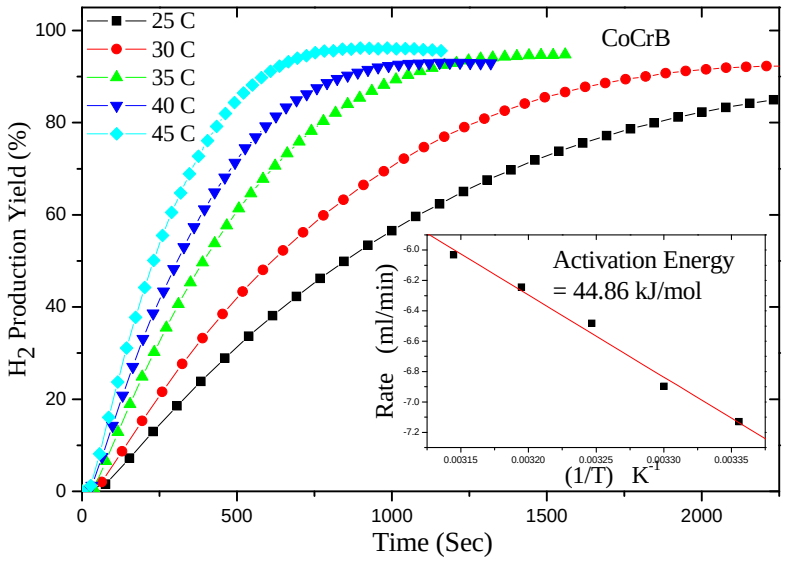

Figure 6.4 – Hydrogen generation yield as a function of reaction time by hydrolysis of AB (0.025 M) solution measured at different solution temperatures with Co-Cr-B ($\chi_{Cr} = 4\%$) powder catalysts. Inset shows the Arrhenius plot of the H_2 generation rates.

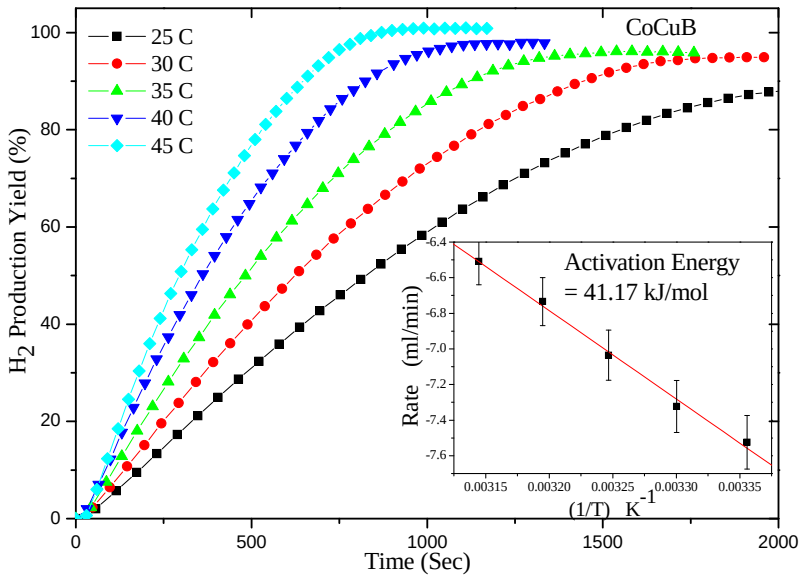

Figure 6.5 – Hydrogen generation yield as a function of reaction time by hydrolysis of AB (0.025 M) solution measured at different solution temperatures with Co-Cu-B (χ_{Cu} = 35%) powder catalysts. Inset shows the Arrhenius plot of the H_2 generation rates.

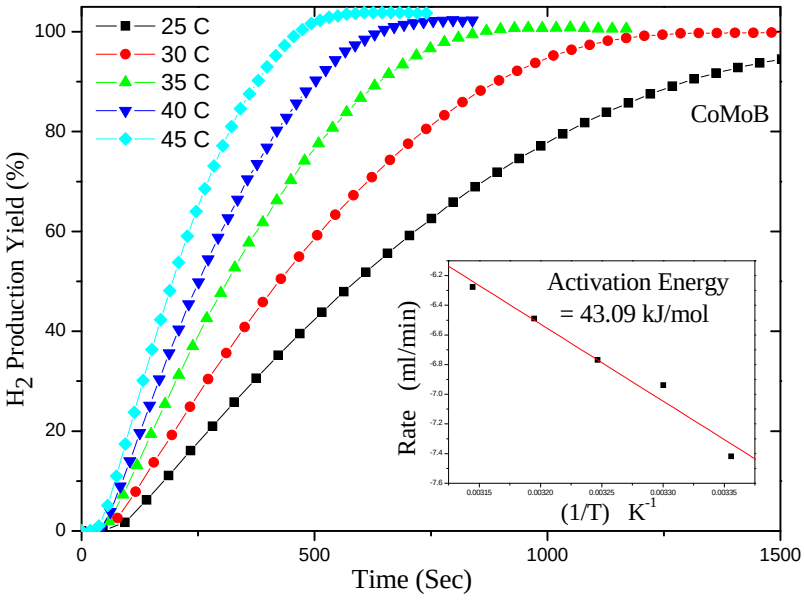

Figure 6.6 – Hydrogen generation yield as a function of reaction time by hydrolysis of AB (0.025 M) solution measured at different solution temperatures with Co-Mo-B (χ_{Mo} = 5%) powder catalysts. Inset shows the Arrhenius plot of the H_2 generation rates.

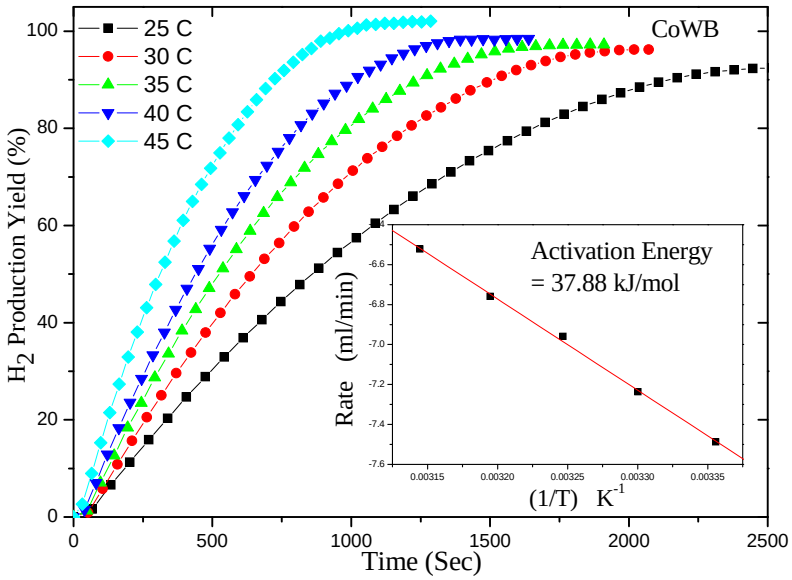

Figure 6.7 – Hydrogen generation yield as a function of reaction time by hydrolysis of AB (0.025 M) solution measured at different solution temperatures with Co-W-B ($\chi_W = 5\%$) powder catalysts. Inset shows the Arrhenius plot of the H_2 generation rates.

In general, the obtained activation energies are lower than that obtained with Rh ($67\,kJmol^{-1}$) nanoclusters [64], Ru/C ($76\,kJmol^{-1}$) [58], K_2PtCl_6 ($86\,kJmol^{-1}$) [61], NiAg ($51\,kJmol^{-1}$) [69], and Co/α-Al_2O_3 ($62\,kJmol^{-1}$) [65]. On the contrary, the obtained values are comparable to that reported for metal catalysts like Ru ($47\,kJmol^{-1}$) [63], Pd metal ($44\,kJmol^{-1}$) [62], Co-Mo-B/Ni foam ($44\,kJmol^{-1}$) [94], and Co (0) nanoclusters ($46\,kJmol^{-1}$) [66].

6.2 Film catalyst for Hydrolysis of Ammonia borane

6.2.1 Co-B film catalyst

The SEM surface morphologies of the Co-B powder and of PLD films are reported in Fig. 6.8 a and b, respectively. The SEM images of catalyst powder show particle-like morphology with particles having size of a few nanometers. During catalyst preparation, the use of $NaBH_4$ as a reducing agent causes a fast reduction of Co ions which inhibit particle growth above a few nanometers. However, these particles tend to agglomerate to minimize their high surface energy. The surface of the PLD Co-B film shows the presence of spherical particulates with a wide distribution of diameter values (average size of $270\,nm$). The observed particles are generated by laser induced phase explosion process.

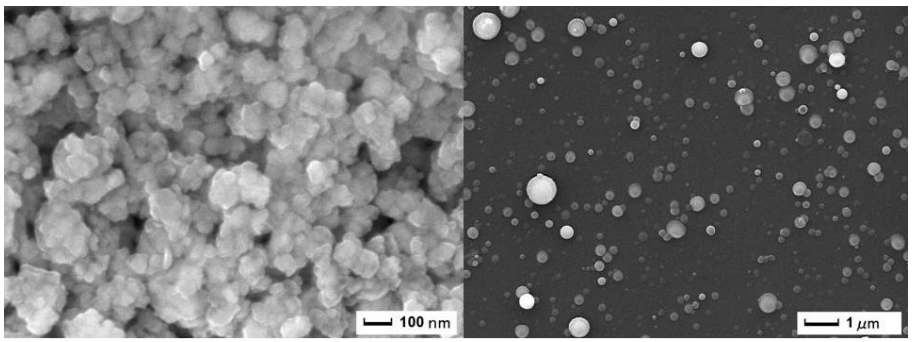

Figure 6.8 – SEM micrographs of Co-B catalyst: (a) powder, and (b) film deposited by PLD.

The 3D image (Fig. 6.9) obtained with AFM also confirms the rough morphology of the surface, with average RMS roughness of 264 nm that is consistent with the particulates formation. XRD patterns (Fig. 6.10) of Co-B powder show a broad peak at around $2\theta = 45^{\circ}$ which is attributed to the amorphous state of cobalt-metalloid alloy. The Co-B film does not exhibit any peak in the XRD spectra (see Fig. 6.10 in which only one peak related to the Si substrate is present) indicating an amorphous structure of the particles which contributes to enhance the catalytic activity. This special feature is well established in the literature and is attributed to the peculiarities of the short-range order but long-range disorder structure [92].

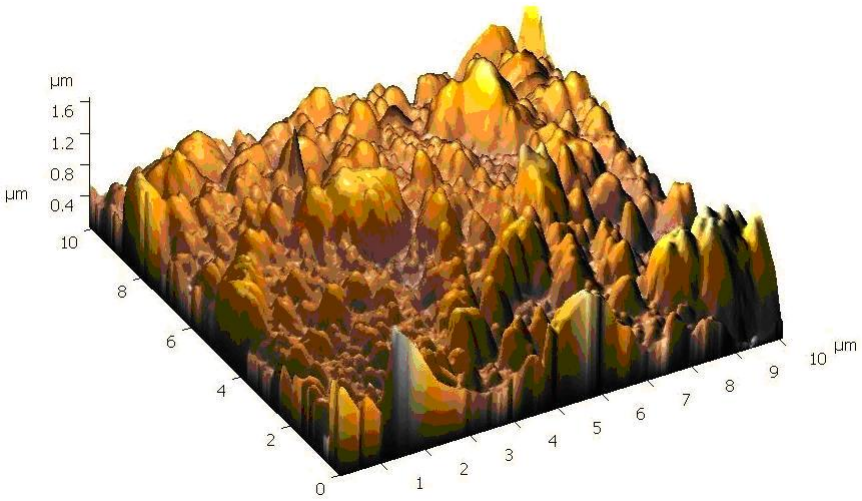

Figure 6.9 – 3D-AFM images of Co-B catalyst film deposited by PLD.

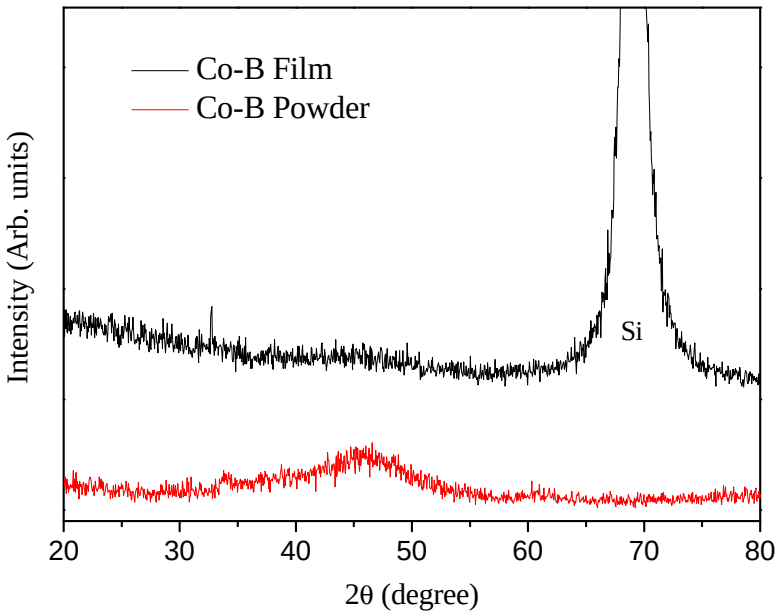

Figure 6.10 – XRD pattern of Co-B catalyst powder and film deposited by PLD.

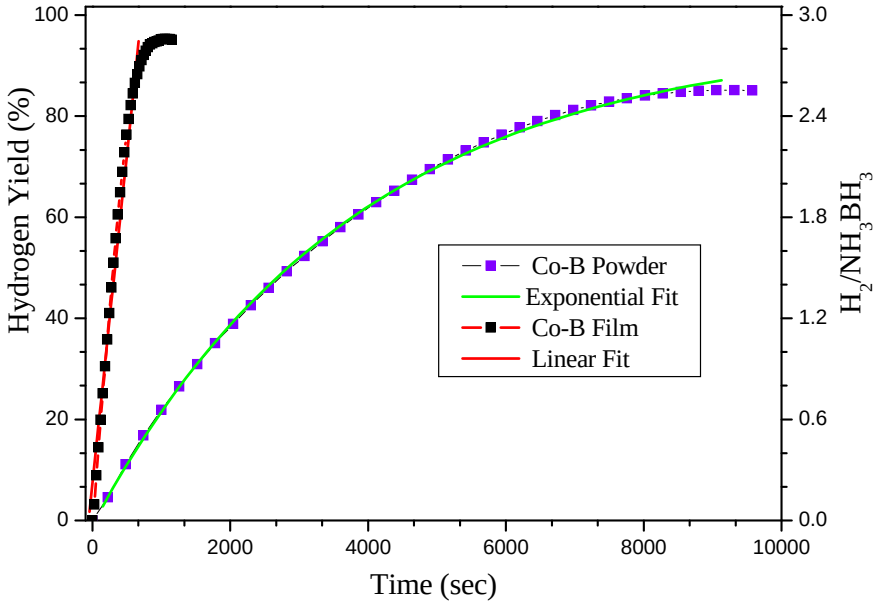

Figure 6.11 – Hydrogen generation yield as a function of reaction time obtained by hydrolysis of NH_3BH_3 (0.025 M) with Co-B catalyst powder and film deposited by PLD.

The catalytic behaviour of Co-B films, synthesized by PLD, was compared with that of the corresponding Co-B powder. Hydrogen generation yield was measured,

as a function of time, during the hydrolysis of AB solution (0.025 M) in presence of Co-B powder and of PLD film at 298 K (Fig. 6.11). The figure clearly shows that both the Co-B catalysts are active and produce hydrogen instantaneously as soon as they come in contact with the AB solution. However, the Co-B film exhibits much higher catalytic activity as compared to the Co-B powder and it was able to complete the reaction within 15 min while the same amount of Co-B powder catalyst (10 mg) took about 145 min. The total amount of hydrogen generated by hydrolysis of AB using Co-B film ($\frac{H_2}{NH_3BH_3} = 2.85$) is closer to the expected quantitative yield, from the reaction stoichiometry ($\frac{H_2}{NH_3BH_3} = 3.0$) than that generated by Co-B powder ($\frac{H_2}{NH_3BH_3} = 2.55$). In addition to the volumetric measurement of H_2 generation, the conversion of the AB was also monitored through ^{11}B NMR by comparing the intensity of the AB signal in the NMR spectra during the course of the reaction. The intensity of ^{11}B peak of AB at 23.9 ppm slowly decreases as the reaction proceeds due to hydrogen evolution. After completion of the reaction, the NMR peak due to AB entirely disappears whereas a broad peak at +11.6 ppm attributed to borate (BO_2) species is visible in the spectra (Fig. 6.12). Thus the above result indicates that the hydrolysis reaction of NH_3BH_3 over Co-B film catalyst proceeds by evolution of nearly 3 moles of H_2, leaving NH_4^+ and BO_2 as end products, in agreement with recent literature reports [71, 124].

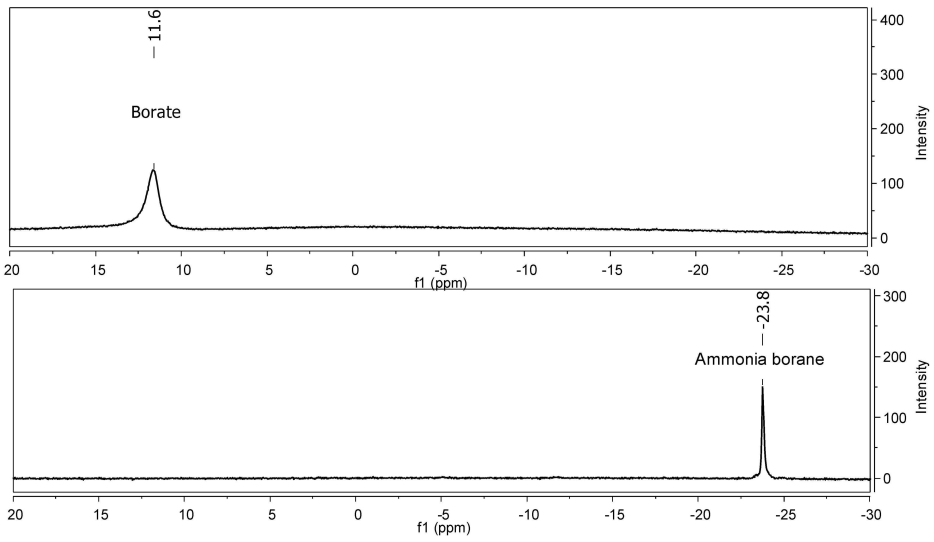

Figure 6.12 – ^{11}B-proton decoupled NMR spectra of: (a) freshly prepared aqueous NH_3BH_3 solution, and (b) reaction product after hydrolysis of NH_3BH_3.

Several films synthesized by using the same PLD parameters showed almost iden-

tical (5%) H_2 generation rate, thus establishing the reproducibility of our produced PLD films. During the reaction, the catalyst films were quite stable in terms of hydrogen production. The maximum H_2 generation rate obtained for the same amount of catalyst ($10\,mg$) by using the Co-B films ($2420\,ml/min/g\,catalyst$) has been found about 6 times higher than that obtained using the Co-B powder ($400\,ml/min/g\,catalyst$). This better catalytic performance is mainly attributed to surface morphology effects in nanoparticle-assembled films (Fig. 6.8). The nanoparticles, having average size of around $300\,nm$, are the highly active sites for the hydrolysis reaction even at low AB concentration and at room temperature. These active Co- B nanoparticles promote the hydrogen production immediately after coming in contact with the solution, as seen by the high initial H_2 generation rate (Fig. 6.11). The relative surface area calculated on the basis of the AFM image of the nanoparticle-assembled Co-B film shows $70-75\%$ increment, with respect to the flat surface

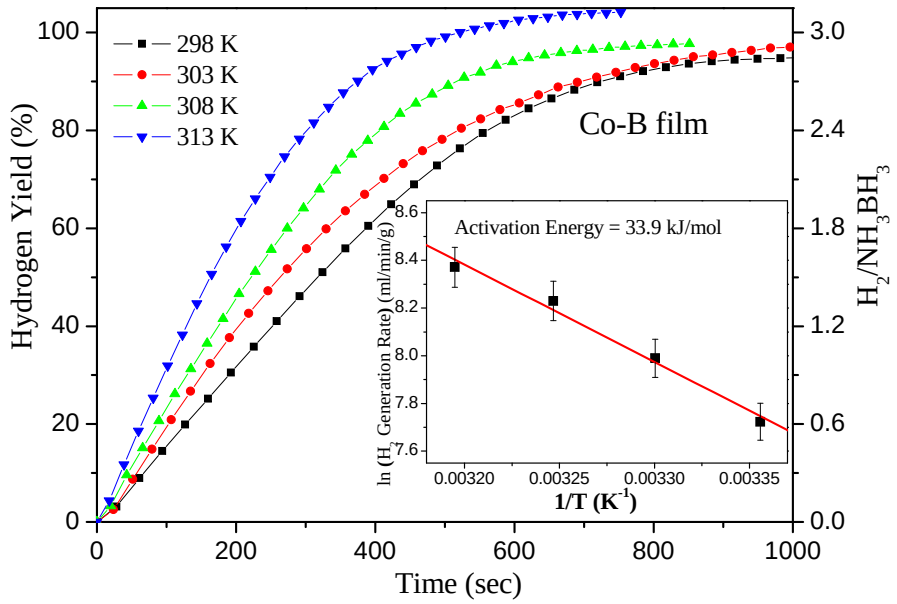

Figure 6.13 – Hydrogen generation yield as a function of reaction time by hydrolysis of NH_3BH_3 (0.025 M) solution with Co-B catalyst film deposited by PLD, measured at 4 different solution temperatures. Inset shows the Arrhenius plot of the H_2 generation rates.

The H_2 generation yield as a function of time was measured at different solution temperatures by hydrolysis of AB (0.025 M) solution using film catalysts as reported in Figs. 6.13. The Arrhenius plot of the hydrogen production rate (inset of Figs. 6.13) gives an activation energy value of $34\,kJmol^{-1}$ for Co-B film which is lower than that

obtained with Co-B powder ($44\,kJmol^{-1}$) (see fig. 6.3). This value is also much lower than that reported in the literature.

Recently, Umegaki et al. [73, 124] demonstrated that Ni is able to generate H_2 from the hydrolysis of $NaBH_4$ and AB mixture at higher rate than from solutions containing only the AB species. The authors proved that $NaBH_4$ is able to activate the catalyst surface thus enhancing the overall rate. In order to understand if such a behavior could also observed in our Co-B catalyst film, we measured the H_2 generation yield (Fig. 6.14), as a function of time, through hydrolysis of AB and $NaBH_4$ mixture with the molar ratio $[AB]/[NaBH_4] = 9$. The enhancing catalytic effect of the small amount of $NaBH_4$ present into AB solution was clearly visible since we observed an increment of about 60% in the R_{max} value as measured by hydrolysis of the hydride mixture ($\sim 3500\,ml/min/g\,catalyst$) as compared to that of pure AB solution ($\sim 2200\,ml/min/g\,catalyst$). As confirmed by XPS analysis, in present Co-B catalyst film there is a partial oxidation of Co on the surface. This oxide is in form of cobalt hydroxide ($Co(OH)_2$) which can be easily reduced by $NaBH_4$ in the course of the hydrolysis thus explaining the enhanced catalytic effect.

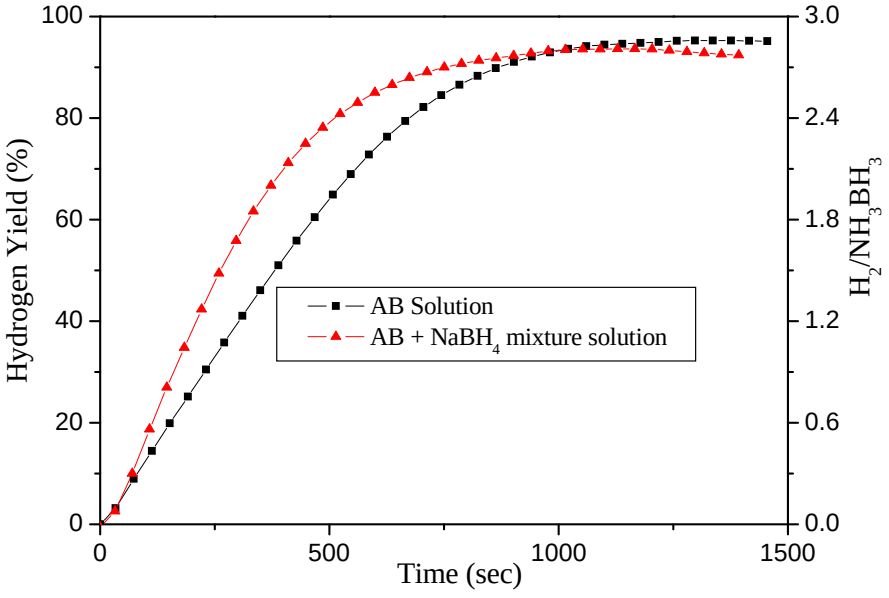

Figure 6.14 – Hydrogen generation yield as a function of reaction time by hydrolysis of NH_3BH_3 (0.025 M) solution and mixture of NH_3BH_3 + $NaBH_4$ solution (0.025 M) (molar ratio of $NH_3BH_3 : NaBH_4$ is kept at 9 : 1) with Co-B catalyst film deposited by PLD.

6.2.2 Co-B on carbon film catalyst

The Co-B film catalyst was able to produce almost expected amount of H_2 (95%) from AB hydrolysis with significantly higher rate (about 6 times) than the same amount of the corresponding Co-B powders (Fig. 6.15). The enhanced catalytic activity was mainly attributed to the Co-B nanoparticles, produced during the ablation process on the film surface, with average size of around $\sim 250\,nm$ and well established spherical form. These nanoparticles not only increase the surface area of the catalyst but also act as the active catalytic cents for the hydrolysis reaction of AB. However, this nanoparticles-assembled film was deposited on the plane glass substrate. Thus in the present work highly irregular and porous carbon film was adopted as a support for the Co-B nanoparticles to effectively improve the initial surface area and obtain better dispersion of nanoparticles. Carbon film was deposited on the glass substrate using Ar gas pressure (40 Pa) in the PLD chamber prior to the deposition of Co-B film. Hereafter Co-B film deposited on glass substrate and on carbon film will be designated as unsupported and C-supported Co-B film, respectively. The catalytic activity of C-supported and unsupported Co-B film was compared by measuring the hydrogen generation yield as function of time by hydrolysis of NH_3BH_3 (0.025 M) solution at 298 K: results are reported in (Fig. 6.15). The figure clearly shows that both the Co-B catalysts films are active and produce hydrogen instantaneously as soon as they come in contact with the AB solution. However, the C-supported Co-B film exhibits higher catalytic activity as compared to the unsupported Co-B film and it was able to complete the reaction within 10 mins while the same amount of unsupported Co-B film catalyst ($\sim 10\,mg$) took about 15 mins. Nevertheless both these Co-B films took significantly less time than Co-B powder catalyst (145 mins). The total amount of hydrogen generated by hydrolysis of AB using both the Co-B films ($\frac{H_2}{NH_3BH_3} = 2.85$) is closer to the quantitative yield expected from the reaction stoichiometry ($\frac{H_2}{NH_3BH_3} = 3.0$) than that generated by Co-B powder ($\frac{H_2}{NH_3BH_3} = 2.55$).

A numerical procedure, was utilized to obtain the maximum value of the hydrogen generation rate (R_{max}) for all the catalysts. By using same catalyst amount ($10\,mg$), the maximum H_2 generation rate obtained for C-supported Co-B films ($\sim 4060\,ml/min/g\,catalyst$) has been found significantly higher than that obtained using the unsupported Co-B film ($\sim 2420 ml/min/g$ catalyst). Several films synthesized by using the same PLD parameters showed almost identical ($\pm 5\%$) H_2 generation rate, thus establishing the reproducibility of our produced PLD films. During the reaction, the catalyst films were quite stable in terms of hydrogen-production and their bonding with the substrate.

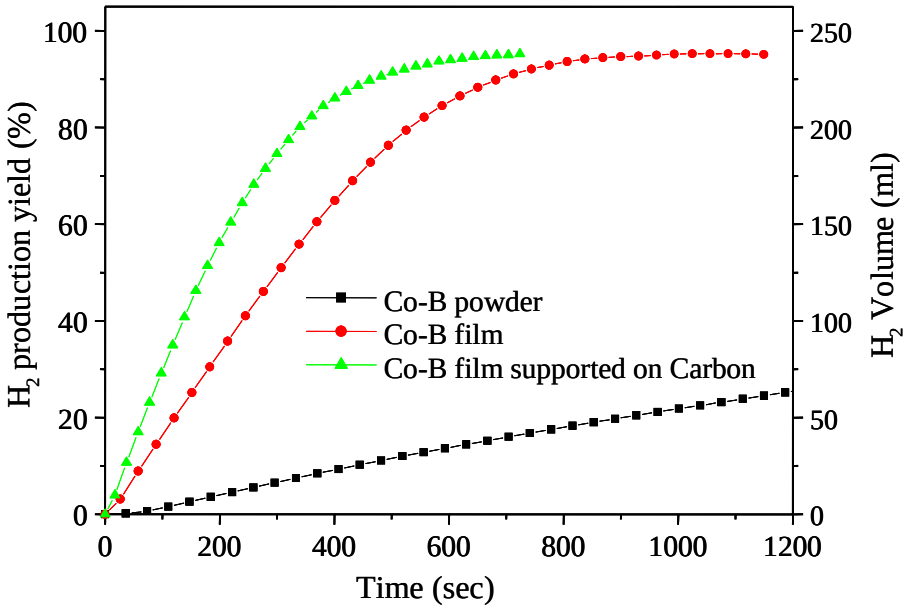

Figure 6.15 – Hydrogen generation yield as a function of reaction time obtained by hydrolysis of NH_3BH_3 (0.025 M) with Co-B catalyst powder and with unsupported and C-supported Co-B film deposited by PLD. Carbon film used for the measurement was deposited with Ar pressure of 40 Pa.

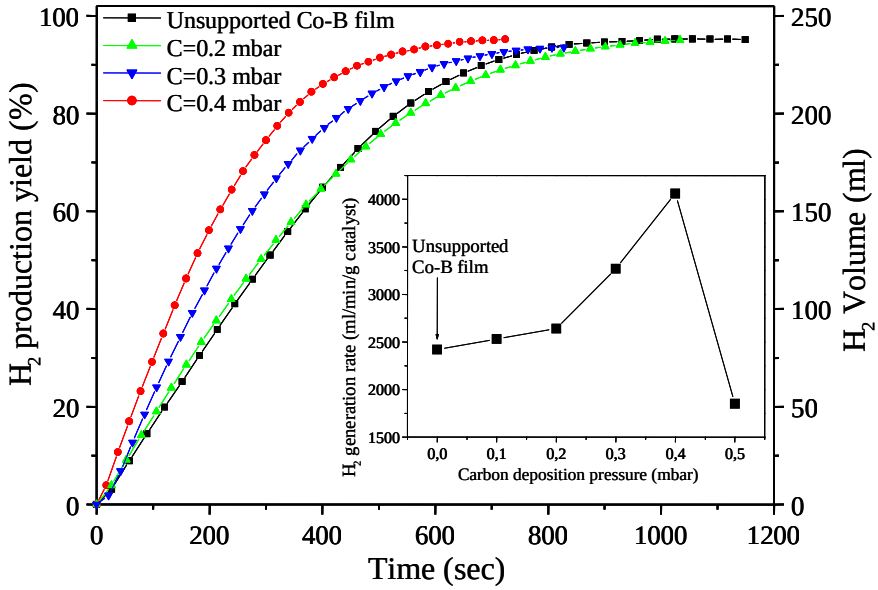

Figure 6.16 – Hydrogen generation yield as a function of reaction time obtained by hydrolysis of NH_3BH_3 (0.025 M) with Co-B film catalyst supported on carbon films deposited with various Ar pressures by PLD. Inset shows the R_{max} as a function of Ar gas pressure used to deposit the carbon films.

Hydrogen generation yield was measured, as a function of time, by the hydrolysis of AB solution (0.025 M) at 298 K in presence of Co-B film catalyst supported on different carbon films deposited with various Ar pressures ranging from 10 to 50 Pa (Fig. 6.16). The inset of figure 6.16 shows the R_{max} as a function of Ar gas pressure used to deposit the carbon films. Co-B catalysts supported on C-film deposited at low Ar pressures (10 and 20 Pa) show almost similar catalytic activity as un-supported Co-B film. We attribute this result to the non-porous structure of C-films. However, the catalytic activity increases for Co-B catalysts supported on C-films deposited at higher Ar pressures (30 and 40 Pa). R_{max} reached the maximum for C-film deposited at 40 Pa. As indicated by SEM images (Fig. 5.11), the roughness and surface area of C-film increases with the deposition pressure. This trend is also followed by the H_2 generation rate for hydrolysis of AB as demonstrated in the inset of Fig. 6.16. Thus, surface area and roughness of C-films play a vital role in the increment of catalytic activity for Co-B film catalyst by providing better dispersion and avoiding aggregation of Co-B nanoparticles. On the contrary, Co-B catalyst supported on C-film deposited at highest pressure of 50 Pa showed drastic decrease in the H_2 generation rate and was not able to complete the hydrolysis reaction of AB. The C-film deposited at this pressure had a very week adhesion with the substrate and thus under vigorous stirring the film slowly detached from the substrate in the reactant solution during the AB hydrolysis reaction.

In Figs. 6.17 the H_2 generation yields, obtained through hydrolysis of AB (0.025 M) solution using C-supported Co-B film, is reported as a function of time at different reaction temperatures. The carbon film deposited with Ar pressure of 40 Pa was used for the measurement. The Arrhenius plot of the hydrogen production rate (inset of Figs. 6.17) gives an activation energy value of $29 \pm 2\, kJmol^{-1}$ for C-supported Co-B film which is lower than that obtained with unsupported Co-B film ($34 \pm 1\, kJmol^{-1}$) and Co-B powder ($44 \pm 1\, kJmol^{-1}$). This value is also much lower than that reported in the literature when using various noble and non-noble metal catalysts.

Finally, we compare the H_2 generation rates obtained with the present C-supported Co-B nanoparticles catalyst with those reported in the literature for different solid catalysts. Generally most of these reports indicate the H_2 generation rate per gram of the active metal catalyst (i.e. $ml/min.g$ of metal catalyst). In our case, only Co is the active metal catalyst and, therefore, the H_2 generation rate, as calculated after linear fitting of our data, is $\sim 13500\, ml\, H_2 min^{-1}(g\, of\, Co)^{-1}$ by hydrolysis of AB. The H_2 generation rate value obtained in the present case is far better than those found for catalysts such as Co/C ($\sim 2000\, ml\, H_2 min^{-1}(g\, of\, Co)^{-1}$ [68], PVP

stabilized Co(0) nanoclusters ($\sim 1500\,ml\,H_2min^{-1}(g\,of\,Co)^{-1}$) [70], $Co-Al_2O_3$ ($\sim 630\,ml\,H_2min^{-1}(g\,of\,Co)^{-1}$ [62], PVP stabilized Ni ($\sim 1100\,ml\,H_2min^{-1}(g\,of\,Ni)^{-1}$ [124], Fe nanoparticles ($\sim 1000\,ml\,H_2min^{-1}(g\,of\,Fe)^{-1}$ [71] and Pt/Al_2O_3 ($\sim 8500\,ml\,H_2min^{-1}(g\,of\,Pt)^{-1}$ [60] catalyst.

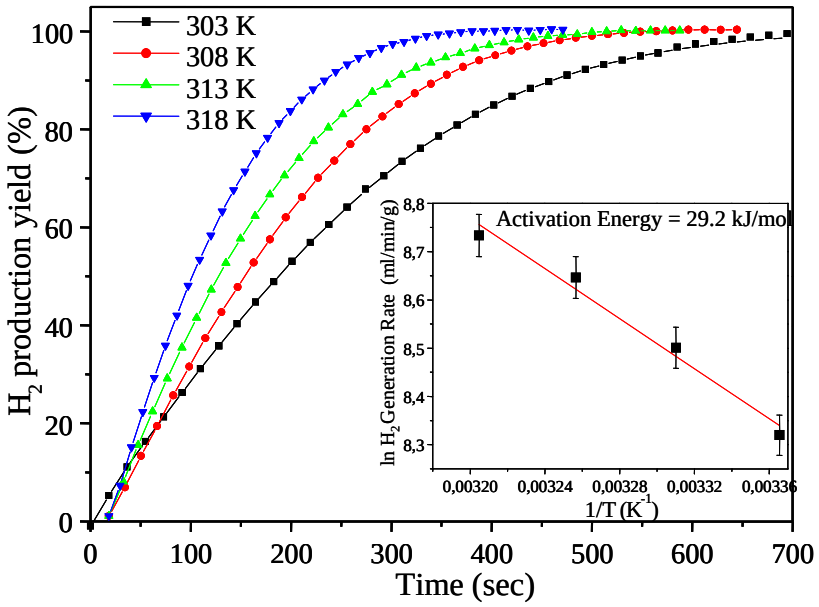

Figure 6.17 – Hydrogen generation yield as a function of reaction time obtained by hydrolysis of NH_3BH_3 (0.025 M) with C-supported (40 Pa) Co-B film catalyst measured at 4 different solution temperatures. Inset shows the Arrhenius plot of the H_2 generation rates.

6.3 Conclusion

The Co-B catalyst was doped, separately, with Cu, Cr, Mo, and W transition metals. The doped catalysts were characterized by XPS, XRD, SEM, BET surface area measurement, and particle size analysis and were tested on H_2 generation process through hydrolysis of Ammonia Borane. All the transition metals induce significant promoting effects on the Co-B catalyst by increasing the H_2 generation rate by about 3 times as compared to the undoped Co-B. It was established that dopant transition-metals, in either oxidized or/and metallic state, act as an atomic barrier that prevents Co-B particle agglomeration thus preserving considerable effective surface area. In addition, the oxidized species such as Cr^{3+}, Mo^{4+}, and W^{4+}, act as Lewis acid sites for better absorption of OH^- group to further assist the hydrolysis reaction over alloy catalysts. The promoting feature of the investigated transition metals on Co-B alloy

powders is also proved by the very low activation energy and high H_2 generation rate measured in hydrolysis of AB.

We have proved that nanoparticle-assembled Co-B thin films, synthesized by PLD, act as efficient catalysts for hydrolysis of AB to produce hydrogen. The comparison was made with same amount of Co-B powders which exhibit a lower rate (about 6 times) of H_2 generation. Almost complete conversion of AB was obtained, as confirmed by ^{11}B NMR, with Co-B films at room temperature: 2.85 moles of H_2 have been generated instead of the maximum expected, i.e. 3.0 equivalents. The activation energy of the rate limiting process involved in the final hydrogen production is as low as $34\,kJ\,mol^{-1}$ and the H_2 generation rate is similar to that reported in the literature for noble metal like Pt/Al_2O_3. The peculiarities of the Co-B nanoparticles, produced by PLD, are related to their well established spherical form and to their density distribution which is preserved against coalescence. In presence of the Co-B film catalyst, the order of the reaction with respect to the AB concentration is zero, a kinetics feature related to the morphological properties of the nanoparticles that are able to confine the hydrogen generation to a surface reaction. On the contrary, the first order kinetics, involving diffusion of BH_4 on the catalyst surface, is the rate limiting step in the case of Co-B powder. Finally we found that adding a small amount of $NaBH_4$ to the AB solution, the efficiency of the Co-B catalyst films increases thus generating H_2 with higher rate. The role of $NaBH_4$ is to activate the catalyst by reducing oxidized forms of Cobalt ($Co(OH)_2$) as observed by XPS and FT-IR analysis.

We synthesized thin films of C-supported Co-B nanoparticles by PLD to be used as catalysts in hydrolysis of AB to produce H_2. PLD deposition of C-film was performed at different Ar pressures (from 10 to 50 Pa) to tailor film roughness in order to investigate the role of porous and irregular C-surface on supporting Co-B nanoparticles acting as catalysts. The hydrogen generation rate attained with C-supported Co-B catalyst film is significantly higher than both unsupported-Co-B film and conventional Co-B powder. Comparative SEM analysis of the different C-films proves that C-support provides high initial surface area to accommodate Co-B nanoparticles thus favouring better dispersion and tolerance against their aggregation. The relevant performance of our C-supported Co-B film is manifested by the very high H_2 generation rate ($\sim 13500\,ml\,H_2\,min^{-1}\ (g\,of\,Co)^{-1}$) from the hydrolysis of AB that is governed by a very low activation energy ($\sim 29\,kJ(mol)^{-1}$) of the rate limiting process.

Chapter 7

Conclusions and future work

"Every new beginning comes from some other beginning's end."
-Lucius Seneca

7.1 Conclusions

With ever growing demand for an efficient and environmentally friendly energy source, hydrogen is forecasted to become a major energy carrier. Hydrogen powered PEM fuel cells are attractive power sources for providing clean energy for transportation and personal electronic applications especially where low system weight and portability are important. Currently, hydrogen is primarily used in the chemical industry, but in the near future it will become a significant fuel. There are many processes for hydrogen production and tremendous amount of research being pursued in the development of hydrogen generation and storage systems. Hydrolysis of chemical hydride (stable aqueous solutions of Sodium Borohydride $NaBH_4$ and Ammonia Borane, AB) in presence of suitable catalyst is a simple, convenient, and safe chemical process that generates high purity hydrogen gas on demand. The catalysts used in the process (like Pt and Pd), are quite expensive and cannot be considered for application purpose due to their high cost. This thesis was aimed at developing new kinds of catalyst that are economical, easy to synthesise and at the same time show high catalytic activity.

The present study reported 12 new types of Co-based catalysts that were synthesised and studied. Eight of them were in form of powder (Co-Ni-B, Co-Fe-B, Co-Cu-B, Co-Cr-B, Co-Mo-B, Co-W-B, Co-P-B, Co-Ni-B-P), while four were synthesised in form of films by using Electroless deposition (ED) technique (Co-P-B film) and by using Pulsed Laser Deposition (PLD) technique (Co-B film, Co-B on carbon, Co-P-B film)

For powder catalyst, the $\frac{Metal}{Co+Metal}$ molar ratio was varied in order to study the effect of each metal dopant concentration on the catalytic efficiency. The catalysts were characterized by XPS, XRD, SEM, BET surface area measurement, and particle size analysis and were then tested by catalytic hydrolysis of $NaBH_4$ and AB for H_2 generation. The present investigation has unveiled that the best promoting effects were obtained only with specific molar concentration of the transition metals. Co-Cr-B with $\chi_{Cr} = 4\%$ catalyst powder, showed the highest H_2 generation rate (R_{max}) of $3400\,ml/min/g$ for hydrolysis of alkaline $NaBH_4$ (0.025 M), While for hydrolysis of AB (0.025 M), Co-Cu-B with $\chi_{Cu} = 35\%$, was found to yield the highest R_{max} of $1254\,ml/min/g$. The results demonstrated that transition metals added to Co-B catalyst impose significant catalytic effects on the H_2 generation rate and increases up to 4 times, as compared to Co-B catalyst accompanied with lower activation energy. The promoting effects (depending on the dopand) were related to: (1) large active surface area of the catalysts (2) ability to act as Lewis acid sites for better absorption of OH groups in case of $NaBH_4$ (3) electronic interaction with Co active metal and (4) amorphous nature of the alloy catalyst.

Film catalysts of Co-B-P were produced by PLD on glass-substrate and by ED on Ni-substrate for the catalytic hydrolysis of $NaBH_4$. R_{max} obtained with electroless deposited films was found to be $\sim 2090\,ml/min/g\,catalyst$, while that synthesized by PLD was $\sim 4230\,ml/min/g\,catalyst$. Co-B thin films were also synthesised for catalytic hydrolysis of AB, The maximum H_2 generation rate obtained for the same amount of catalyst ($10\,mg$) by using the Co-B films ($2420\,ml/min/g\,catalyst$) has been found about 6 times higher than that obtained using the Co-B powder ($400\,ml/min/g\,catalyst$). The increased efficiency of the PLD films is mainly attributed to the nanoparticles formed on the catalyst surface, by phase explosion phenomena occurring in laser-irradiated material at an appropriate parameters of the laser pulse. These nanoparticles increase the active surface area and also favours electronic exchange mechanisms to promote efficient hydrolysis process for H_2 gas generation.

Thin films of Carbon (C) supported Co-B nanoparticle catalysts were also synthesized by PLD for the hydrolysis of $NaBH_4$ and AB to produce H_2. PLD deposition of C-film was performed at different Ar pressures (from 10 to 50 Pa) to tailor film roughness and to study the role of porous and irregular C-surface that supported Co-B nanoparticles. The hydrogen generation rate attained with C-supported Co-B catalyst film is significantly higher than both unsupported-Co-B film and conventional Co-B powder. Comparative SEM analysis of the different C-films proves that C-support

provides high initial surface area to accommodate Co-B nanoparticles thus favouring better dispersion and tolerance against their aggregation. The hydrogen generation rate attained with carbon-supported Co-B catalyst film (Ar pressure of 40 Pa for C deposition) was found to be $\sim 8100\, ml/min/g\, catalyst$ and $\sim 4060\, ml/min/g\, catalyst$ for catalytic hydrolysis of $NaBH_4$ and AB respectively. The highest hydrogen generation rate and the activation energies for all the catalysts are summerised in Table. 7.1

Catalyst powders	Max H_2 generation rate $(ml/min/g\, catalyst)$		Activation energy $(kJmol^{-1})$	
	$NaBH_4$	AB	$NaBH_4$	AB
Co-B	850	400	45	44
Co-Ni-B ($\chi_M = 15$)	1175	-	34	-
Co-Fe-B ($\chi_M = 35$)	1300	-	31	-
Co-Cu-B ($\chi_M = 35$)	2210	**1254**	30	41
Co-Cr-B ($\chi_M = 4$)	**3400**	1058	37	44
Co-Mo-B ($\chi_M = 5$)	2875	1231	39	43
Co-W-B ($\chi_M = 5$)	2570	1000	41	38
Co-B-P ($\frac{B}{P} = 2.5$)	2120	-	-	-
Co-Ni-B-P ($\chi_M = 15, \frac{B}{P} = 2.5$)	2400	-	29	-
Co-B film (PLD)	4330	2420	-	34
Co-B-P Film (PLD)	4320	-	-	-
Co-B-P Film (ED)	2090	-	-	-
Co-B on Carbon (PLD)	**8100**	**4060**	31	29

Table 7.1 – Maximum H_2 generation rate and activation energy of catalyst powders and films

7.2 Future Work

Most of the efforts in the future can be devoted to improvement and development of the catalyst for hydrogen production. Probing deeper, the results in this thesis provide several lines of research arising which should be pursued.

- We have observed that metal doped Co-B catalytic powders and Co-B film produced by PLD have higher efficiencies than Co-B powder catalyst. Combining

them both, metal doped Co-B films using PLD technique can be developed and studied for Hydrolysis of $NaBH_4$ and AB in the future.

- Co-B catalyst powder can be doped with more than one metal; the combined effect of the metals could result in even higher catalytic activity and can be studied.

- The atomic composition of the synthesized nanoparticles depends on the laser pulse energy: specifically, we have observed that by increasing the laser pulse energy, the atomic composition of the heavier element (Co) is prevailing over the light elements. A dedicated investigation is required for understanding the ablalation process for binary and ternary alloy powders.

- Until now the PLD film that were prepared, lacked very good adhesion with the glass substrate, and hence they tend to peal out when used for a very long time. An alternative substrate such as Ni-foam can be used to deposit these films using PLD for better adhesion.

- Fuel cells that are used for the portable device to generate power, can be tested by attaching it to the present H_2 generation reactor system. The H_2 produced by catalytic hydrolysis of $NaBH_4$ can be directly supplied as fuel to generate power.

- A compact hydrolysis reactor with controllable continuous flow system having a fixed catalyst bed can be developed that can be refuelled with fresh $NaBH_4$ or AB solution. Ni-foam coated with film by ED can be used as catalyst fixed screen through which the solution continuously flows in the reactor to produce hydrogen, while the inner wall of the reactor tube should be coated with efficient nanoparticle-assembled catalyst film synthesized by PLD to ensure a very efficient reaction.

List of Figures

List of Tables

References

[1] A. Midilli, M. Ay, I. Dincer, M. Rosen, *Renewable and Sustainable energy Reviews* **2005**, *9*, 255–271.

[2] *U.S. Energy Information Administration* **2010**.

[3] *Oil and Gas Journal*, *107*, 20–21.

[4] *BP Statistical Review of World Energy 2010*, www.bp.com.

[5] Wikipedia, *http://en.wikipedia.org/wiki/Natural-gas*.

[6] G. Nicoletti, *International Journal of Hydrogen energy* **1995**, *20*, 759–765.

[7] I. Dincer, *Energy Policy* **1999**, *27*, 845–854.

[8] Q. Xu, J. Chandra, *Catalysis Today* **2002**, *77*, 17–49.

[9] *International Energy Agency* **2010**.

[10] A. Dicks, *Journal of Power Sources* **1996**, *61*, 113–124.

[11] S. Satyapal, J. Petrovic, C. Read, G. Thomas, G. Ordaz, *Catalysis Today* **2007**, *120*, 246–256.

[12] A. Zuttel, *Naturwissenschaften* **2004**, 157–172.

[13] L. Schlapbach, A. Zuttel, *Nature* **2001**, *414*, 353–358.

[14] B. D. Solomon, A. Banerjee, *Energy Policy* **2006**, *34*, 781–792.

[15] Wikipedia, *http://en.wikipedia.org/wiki/Engine-efficiency*.

[16] S. C. Amendola, S. L. Sharp-goldman, M. S. Janjua, N. C. Spencer, M. T. Kelly, P. J. Petillo, M. Binder, *International Journal of Hydrogen Energy* **2000**, *25*, 969–975.

[17] K. S. Jeong, B. Oh, *Journal of Power Sources* **2002**, *105*, 58–65.

[18] C. J. Zhong, J. Luo, P. N. Njoki, D. Mott, B. Wanjala, R. Loukrakpam, S. Lim, *Energy and Environmental Science* **2008**, *1*, 454–466.

[19] A. Bauen, D. Hart, *Journal of Power Sources* **2000**, *86*, 482–494.

[20] G. Hoogers, *Fuel Cell Technology Handbook, CRC Press* **2003**.

[21] *U.S. Energy Department* **2003**, http://www.energy.gov/.

[22] *Ballard Power Systems* **2010**, http://www.ballard.com/.

[23] N. Sammes, *Fuel Cell Technology* **2006**.

[24] C. Zhong, J. Luo, B. Fang, B.Wanjali, P. Njoki, R. Loukarakpam, J. Yin, *Nanotechnology* **2010**, *21*, 1–20.

[25] B. Steele, A. Heinzel, *Nature* **2001**, *414*, 345–352.

[26] K. Praveen, Cheekatamarla, C. M. Finnerty, *Journal of Power Sources* **2006**, *160*, 490–499.

[27] M. Momirlan, T. N. Veziroglu, *Renewable and Sustainable Energy Reviews* **2002**, *6*, 141–179.

[28] A. Sarkar, R. Banerjee, *Interlational Journal of Hydrogen Energy* **2005**, *30*, 867–877.

[29] A. Zuttel, *Materials today* **2003**, *6*, 24–33.

[30] U. Eberle, M. Felderhoff, F. Schuth, *Angewandte Chemie international edition* **2009**, *48*, 6608–6630.

[31] X. L. Ding, X. Yuan, C. Jai, Z. F. Ma, *International Journal of Hydrogen energy* **2010**, *35*, 11077–11084.

[32] J. Liang, Y. Li, Y. Huang, J. Yang, H. Tang, Z. Wei, S. P. K, *Interlational Journal of Hydrogen Energy* **2008**, *33*, 4048–4054.

[33] Z. T. Xia, S. H. Chan, *Journal of Power Sources* **2005**, *152*, 46–49.

[34] U. B. Dermicri, P. Miele, *Physical Chemistry Chemical Physics* **2010**, *12*, 14651–14665.

[35] M. Diwan, H. T. Hwang, A. Al Kuhun, A. Varma, *AlChE Journal* **2011**, *57*, 259–264.

[36] S. B. Kalidindi, A. A. Vernekar, B. R. Jagirdar, *Physical Chemistry Chemical Physics* **2009**, *11*, 770–775.

[37] S. Orimoa, Y. Nakamoria, G. Kitaharaa, K. Miwab, N. Ohbab, S. Towatab, A. Zuttel, *Journal of Alloys and Compound* **2005**, *427*, 404–406.

[38] E. Fakioglu, Y. Yuruma, T. N. Veziroglu, *International Journal of Hydrogen* **2004**, *29*, 1371–1376.

[39] T. Umegaki, J. Yan, X. Zhang, H. Shioyama, N. Kuriyama, Q. Xu, *International Journal of Hydrogen energy* **2008**, *34*, 2303–2311.

[40] F. H. Stephens, V. Pons, R. Baker, *Dalton Transactions* **2007**, *25*, 2613–2626.

[41] Z. P. Lin, N. Morigazaki, B. H. Liu, S. Suda, *Journal of Alloys and Compounds* **2003**, *349*, 232–236.

[42] H. Schlesinger, H. Brown, A. Finholt, J. Gilbreath, H. Hockstra, E. Hyde, *Journal of the American Chemical Society* **1953**, *75*, 215–219.

[43] R. W. Kreevoy, M. M. Jacobson, *Ventron Alembic* **1979**, *15*, 2–3.

[44] J. C. Walter, A. Zurawaski, D. Montgomery, M. Thornburg, S. Revankar, *Journal of Power Sources* **2008**, *179*, 335–339.

[45] C. M. Kaufman, B. Sen, *Journal of Chemical Society Dalton Trans* **1985**, *2*, 307–313.

[46] S. Suda, Y. Sun, B. Liu, Y. Zhou, S. Morimitsu, K. Arai, N. Tsukamoto, M. Uchida, Y. Candra, Z. Li, *Applied Physics A* **2001**, *72*, 209–212.

[47] Y. Kojima, K. Suzuki, Y. Kawai, *Journal of Power Sources* **2006**, *155*, 325–328.

[48] Y. Bai, C. Wu, F. Wu, B. Yi, *Materials Letters* **2006**, *60*, 2236 – 2239.

[49] G. Guella, C. Zanchetta, B. Patton, a. Miotello, *The journal of physical chemistry. B* **2006**, *110*, 17024–17033.

[50] P. Krishnan, S. G. Advani, A. K. Prasad, *Applied Catalysis B* **2009**, *86*, 137–144.

[51] C. H. Hsueh, C. Y. Chen, J. R. Ku, S. F. Tsai, Y. Y. Hsu, F. Tsu, M. S. Jeng, *Journal of Power Sources* **2008**, *177*, 485–492.

[52] S. Ozkar, M. Zahmakiran, *Journal of Alloys and Compounds* **2005**, *404*, 728–731.

[53] H. B. Liu, P. Z. Li, S. Suda, *Journal of Alloys and Compounds* **2006**, *415*, 288–293.

[54] D. Hua, Y. Hanxi, A. Xinping, C. C, *Interlational Journal of Hydrogen Energy* **2003**, *28*, 1095–1100.

[55] J. Lee, K. Y. Kong, C. R. Jung, E. Cho, S. P. Yoon, J. Han, T. G. Lee, S. W. Nam, *Catalysis Today* **2007**, *120*, 305–310.

[56] H. Ma, W. Ji, J. Zhao, J. Liang, J. Chen, *Journal of Alloys and Compounds* **2009**, *474*, 584–589.

[57] M. Diwan, *International Journal of Hydrogen Energy* **2008**, *33*, 1135–1141.

[58] S. Hausdorf, F. Baitalow, G. Wolf, F. Mertens, *International Journal of Hydrogen Energy* **2008**, *33*, 608– 614.

[59] B. Peng, J. Chen, *Energy and Environmental Science* **2008**, *1*, 479–483.

[60] Q. Xu, M. Chandra, *Journal of Alloys and Compounds* **2007**, *446*, 729–732.

[61] M. Chandra, Q. Xu, *Journal of Power Sources* **2006**, *156*, 190–194.

[62] S. Basu, A. Brockman, P. Gagare, Y. Zheng, P. Ramachandran, W. Delgass, J. Gore, *Journal of Power Sources* **2009**, *188*, 238–243.

[63] V. Simagina, P. Storozhenko, O. Netskina, O. Komova, G. Odegova, Y. Larichev, A. Ishchenko, A. Ozerova, *Catalysis Today* **2008**, *138*, 253–259.

[64] N. Mohajeri, a. Traissi, O. Adebiyi, *Journal of Power Sources* **2007**, *167*, 482–485.

[65] O. Metin, S. Sahin, S. Ozkar, *International Journal of Hydrogen Energy* **2009**, *34*, 6304–6313.

[66] F. Durap, M. Zahmakiran, S. Ozkar, *International Journal of Hydrogen Energy* **2009**, *34*, 7223–7230.

[67] M. Zahmakiran, S. Ozkar, *Applied Catalysis B* **2009**, *89*, 104–110.

[68] Q. Xu, J. Chandra, *Journal of Power Sources* **2006**, *163*, 364–370.

[69] T. J. Clark, G. R. Whittell, I. Manners, *Inorganic chemistry* **2007**, *46*, 7522–7527.

[70] O. Metin, S. Ozkar, *Energy and Fuel* **2009**, *23*, 3517–3526.

[71] J. M. Yan, X. B. Zhang, S. Han, H. Shioyama, Q. Xu, *Chem. Int. Ed.* **2008**, *47*, 2287–2289.

[72] C. F. Yao, L. Zhuang, Y. L. Cao, X. P. Ai, H. X. Yang, *Interlational Journal of Hydrogen Energy* **2008**, *33*, 2462–2467.

[73] T. Umegaki, J. Yan, X. Zhang, H. Shioyama, N. Kuriyama, Q. Xu, *Journal of Power Sources* **2009**, *191*, 209–216.

[74] U. B. Demirci, P. Miele, *Energy Environment Science* **2009**, *2*, 627–637.

[75] M. Bonelli, C. Cestari, A. Miotello, *Mesurement Science and Technology* **1999**, *10*, N27–N30.

[76] C. Zanchetta, B. Paton, G. Guella, A. Miotello, *Mesurement Science and Technology* **2007**, *18*, N21–N26.

[77] S. U. Jeong, E. A. Cho, S. W. Nam, I. H. Oh, U. H. Jung, S. H. Kim, *International Journal of Hydrogen Energy* **2007**, *32*, 1749 – 1754.

[78] N. Patel, G. Guella, a. Kale, a. Miotello, B. Patton, C. Zanchetta, L. Mirenghi, P. Rotolo, *Applied Catalysis A: General* **2007**, *323*, 18–24.

[79] H. Li, Y. Wu, Y. Wan, J. Zhang, W. Dai, M. Qiao **2004**, *95*, 493–503.

[80] K. Eom, K. Cho, H. Kwon, *Journal of Power Sources* **2008**, *180*, 484–490.

[81] X. Yu, H. Li, J. F. Deng, *Applied Catalysis A: General* **2000**, *199*, 191–198.

[82] H. Li, P. Yang, D. Chu, H. Li, *Applied Catalysis A: General* **2007**, *325*, 34–40.

[83] S. P. Lee, Y. W. Chen, *Journal of Molecular Catalysis* **2000**, 213–223.

[84] W. L. Dai, M. H. Qiao, J. F. Deng, *Applied Surface Science* **1997**, *120*, 119–124.

[85] A. Lebugle, U. Axelsson, R. Nyholm, N. Martensson, *Physica Scripta* **1981**, *23*, 825–827.

[86] H. Li, P. Palanca, V. Sanz, L. Lahoz, *Inorganica Chimica Acta* **1999**, *285*, 25–30.

[87] H. Li, Y. Wu, H. Luo, M. Wang, Y. Xu, *Journal of Catalysis* **2003**, *214*, 15–25.

[88] S. Yoshida, H. Yamashita, T. Funabiki, T. Yonezawa, *Journal of the Chemical Society, Faraday Transactions 1* **1984**, *80*, 1435–1446.

[89] H. Li, Y. Wu, J. Zhang, W. Dai, M. Qiao, *Applied catalysis A :Gen.* **2004**, *275*, 199–206.

[90] C. Wu, F. Wu, Y. Bai, B. Yi, H. , *Materials Letters* **2005**, *59*, 1748–1751.

[91] G. W. Pei, W. L. Zhong, S. B. Yue, *X-ray Diffraction of Single, Crystalline and Amorphous Materials, Shandong Univ. Press, Jinan* **1989**, *18*, 453.

[92] A. Baiker, *Faraday Discussions of the Chemical Society* **1989**, *87*, 239–251.

[93] H. Li, Q. Zhao, H. Li, *Journal of Molecular Catalysis A: Chemical* **2008**, *285*, 29–35.

[94] H. Li, W. Wang, H. Li, J. F. Deng, *Journal of Catalysis* **2000**, *194*, 211–214.

[95] W. S. Xia, Y. Fan, Y. S. Jiang, Y. Chen, *Applied Surface Science* **1996**, *103*, 1–9.

[96] Q. Zhang, G. M. Smith, Y. Wu, *International Journal of Hydrogen Energy* **2007**, *32*, 4731–4735.

[97] N. Patel, R. Fernandes, G. Guella, A. Kale, A. Miotello, B. Patton, C. Zanchetta, *Journal of Physical Chemistry* **2008**, *112*, 6968–6976.

[98] R. Fernandes, N. Patel, A. Miotello, M. Filippi, *Journal of Molecular Catalysis A* **2009**, *298*, 1–6.

[99] N. Patel, R. Fernandes, A. Miotello, *Journal of Power sources* **2009**, *188*, 411–420.

[100] Y. Pei, P. Guo, M. Qiao, H. Li, S. Wei, H. He, *Journal of Catalysis* **2007**, *248*, 303–310.

[101] W. Ye, H. Zhang, D. Xu, L. Ma, B. Yi, *Journal of Power Sources* **2007**, *164*, 544–548.

[102] T. Dong Ge, C. Wei, L. Yong Yue, C. Hongc, J. Xiao Yangc, *Journal of Molecular Catalysis A : Chemical* **2007**, *269*, 149–157.

[103] H. Li, J. F. Deng, *Journal of Chemical Technology and Biotechnology* **2001**, *76*, 985–990.

[104] R. Fernandes, N. Patel, A. Miotello, *Applied Catalysis B : Environmental* **2009**, *92*, 68–74.

[105] J. Fang, X. Chen, B. Liu, S. Yan, M. Qiao, H. Li, H. He, *Journal of Catalysis* **2005**, *229*, 97–104.

[106] B. H. Liu, Q. Li, *International Journal of Hydrogen Energy* **2008**, *33*, 7385–7391.

[107] A. Garron, D. Swierczynski, S. Bennici, A. Auroux, *International journal of hydrogen energy* **2009**, *34*, 1185–1199.

[108] N. Patel, B. Patton, C. Zanchetta, R. Fernandes, G. Guella, A. Kale, A. Miotello, *International Journal of Hydrogen Energy* **2008**, *33*, 287–292.

[109] Y. Shang, R. Chen, *Energy & Fuel* **2006**, *20*, 2149–2154.

[110] S. C. Amendola, S. Sharp-Goldman, M. S. Janjua, M. T. Kelly, P. J. Petillo, M. Binder, *Journal of Power Sources* **2000**, *85*, 186.

[111] J. H. Wee, *Journal of Power Sources* **2006**, *155*, 329–339.

[112] B. Richardson, J. F. Birdwell, F. G. Pin, J. F. Jansen, R. F. Lind, *Journal of Power Sources* **2005**, *145*, 21–29.

[113] R. Fernandes, N. Patel, A. Miotello, *International Journal of Hydrogen Energy* **2009**, *34*, 2893–2900.

[114] A. Miotello, R. Kelly, *Applied Physics Letters* **1995**, *67*, 3535.

[115] A. Miotello, R. Kelly, *Applied Physics A: Materials Science & Processing* **1999**, *69*, S67–S73.

[116] N. Patel, R. Fernandes, N. Bazzanella, A. Miotello, *Thin Solid Films* **2010**, *518*, 4779–4785.

[117] N. Patel, R. Fernandes, G. Guella, a. Kale, a. Miotello, B. Patton, C. Zanchetta, P. Ossi, V. Russo, *Applied Surface Science* **2007**, *254*, 1307–1311.

[118] L. V. Zhigilei, Z. Lin, D. S. Ivanov, *The Journal of Physical Chemistry C* **2009**, *113*, 11892–11906.

[119] R. Kelly, A. Miotello, *Applied Surface Science* **1996**, *96-98*, 205–215.

[120] J. Zhao, H. Ma, J. Chen, *International Journal of Hydrogen Energy* **2007**, *32*, 4711–4716.

[121] H. B. Dai, J. Liang, P. Wang, H. M. Cheng, *Journal of Power Sources* **2008**, *177*, 17–23.

[122] D. Xu, D. Dai, X. Liu, C. Cao, Q. Guo, *Journal of Power Sources* **2008**, *182*, 616–620.

[123] N. Patel, R. Fernandes, A. Miotello, *Journal of Catalysis* **2010**, *271*, 315–324.

[124] T. Umegaki, J. Yan, X. Zhang, H. Shioyama, N. Kuriyama, Q. Xu, *International Journal of Hydrogen Energy* **2009**, *34*, 3816–3822.

List of Publications

1. N. Patel, **R. Fernandes**, G. Guella, A. Miotello. "Promoting effect of transition metal-doped Co-B alloy catalysts for hydrogen production by hydrolysis of alkaline $NaBH_4$ solution". *Journal of Catalysis.* 271 (**2010**) 315 - 324.

2. N. Patel, **R Fernandes**, N. Bazzanella and A. Miotello. "Co-P-B catalyst thin films prepared by electroless and pulsed laser deposition for hydrogen generation by hydrolysis of alkaline sodium borohydride: a comparison". *Thin Solid Films*, 518 (**2010**) 4779 - 4785.

3. N. Patel, **R. Fernandes**, G. Guella, A. Miotello. "Nanoparticle-assembled Co-B thin film for the hydrolysis of ammonia borane: A highly active catalyst for hydrogen production". *Applied Catalysis B: Environmental*, 95 (**2010**) 137 - 143.

4. N. Patel, **R Fernandes**, N. Bazzanella and A. Miotello. "Enhanced hydrogen production by hydrolysis of $NaBH_4$ using "Co-B nanoparticles supported on Carbon film" catalyst synthesized by pulsed laser deposition". *Catalysis Today,* doi:10.1016/j.cattod.2010.11.077 (in press)

5. **R. Fernandes**, N. Patel, A. Miotello, M. Filippi. "Studies on catalytic behavior of Co-Ni-B in hydrogen production by hydrolysis of $NaBH_4$". *Journal of Molecular Catalysis A: Chemical*, 298 (**2009**) 1 - 6.

6. **R. Fernandes**, N. Patel, and A. Miotello. "Efficient catalytic properties of Co-Ni-P-B catalyst powders for hydrogen generation by hydrolysis of alkaline solution of $NaBH_4$". *International Journal of Hydrogen Energy*, 34 (**2009**) 2893 - 2900.

7. **R. Fernandes**, N. Patel, and A. Miotello. "Hydrogen generation by hydrolysis of alkaline $NaBH_4$ solution with Cr-promoted Co-B amorphous catalyst". *Applied Catalysis B: Environmental*, 92 (**2009**) 68 - 74.

8. **R. Fernandes**, N. Patel, R. Dholam, M. Adami, A. Miotello. "Low energy ion-beam modification of TiO_2 photocatalyst thin film for visible light absorption". *Surface & Coatings Technology*, 203 (**2009**) 2579 - 2583.

9. N. Patel, **R. Fernandes**, and A. Miotello. "Hydrogen Generation by hydrolysis of $NaBH_4$ with efficient Co-P-B catalyst: A kinetic study". *Journal of Power Sources*, 188 (**2009**) 411 - 420.

10. N. Patel, **R. Fernandes**, G. Guella, A. Kale, A. Miotello, B. Patton, C. Zanchetta. "Structured and nanoparticle assembled Co-B thin films prepared by Pulsed Laser Deposition: a very efficient catalyst for hydrogen production". *Journal of Physical Chemistry* C, 112 (**2008**) 6968 - 6976.

11. N. Patel, B. Patton, C. Zanchetta, **R Fernandes**, G. Guella, A. Kale, A. Miotello. "Pd-C Powder and thin film catalyst for hydrogen production by hyrdolysis of sodium borohydride". *International Journal of Hydrogen Energy* 33 (**2008**) 287 - 292.

12. N. Patel, **R. Fernandes**, G. Guella, A. Kale, A. Miotello, B. Patton, C. Zanchetta, P. M. Ossi, V. Russo. "Pulsed-laser deposition of nanostructured Pd/C thin films. A new entry into metal-supported catalysts for hydrogen producing reactions". *Applied Surface Science*, 254 (**2007**) 1307 - 1311.

Appendix A

Fitting for H_2 generation rate.

In the zero-order reaction, plotting H_2 production yield as a function of time results in a linear dependence, and the rate of reagent $[BH_4^-]$ consumption is given by

$$-\frac{[BH_4^-]}{dt} = k_0[BH_4^-]^0 = k_0 \tag{A.1}$$

Since every mole of BH_4 produces 4 mol of H_2, the rate of hydrogen production is thus given by

$$\frac{d[H_2]}{dt} = 4k_0 \tag{A.2}$$

In the first-order reaction, plotting H_2 production yield as a function of time results in an exponential dependence as described by

$$[H_2](t) = [H_2]_{max}(1 - e^{-k_1 t}) = 4[[BH_4^-]_0(1 - e^{-k_1 t})] \tag{A.3}$$

where $[BH_4^-]_0$ is the initial molar concentration of sodium borohydride in the solution and k_1 is the overall rate constant of the reaction given by

$$\frac{-d[BH_4^-]}{dt} = k_1[BH_4^-] = k_{hyd}[H_2O][catalyst][BH_4^-] \tag{A.4}$$

or in terms of hydrogen concentration

$$\frac{d[H_2]}{dt} = 4k_1[BH_4^-] = k_{hyd}[H_2O][catalyst][BH_4^-] \tag{A.5}$$

By fitting the curve of H_2 production yield as a function of time by using eq. A.2 or eq. A.5, both reaction order and rate constant k_1 can be evaluated. The last quantity may be used to calculate the H_2 generation rate in terms of $mL/(min\,g\,of\,catalyst)$ by taking into account the concentration of the $NaBH_4$ (molarity of the solution, M) and of catalyst. In fact, the initial molar concentration of sodium borohydride

in the solution is known, and when the reaction is exhausted (100% conversion), it is simple to calculate the total volume of produced H_2 (V_{H_2}). By considering a first-order hydrolysis reaction and rewriting eq. A.3 in terms of produced volume of H_2 gas, instead of molar concentration, we have

$$V(t) = V_{H_2}(1 - e^{-k_1 t}) \tag{A.6}$$

with production rate given by

$$\frac{dV}{dt} = V_{H2} k1 e^{-k_1 t} \tag{A.7}$$

The maximum H_2 generation rate ($mL/(min\, g\, of\, catalyst)$) was estimated, when $[BH_4^-]$ is maximum (first-order reaction), i.e., for $t = 0$, as follows:

$$maximim\, rate = \frac{dV}{dt} = \frac{V_{H_2} k_1}{g_{catalyst}} \tag{A.8}$$

Appendix B

Proposed mechanism for the $NaBH_4$ hydrolysis reaction on Co-B catalyst.